ROBAT

EXPERIMENTAL INVESTIGATION OF A BAT INSPIRED ROBOTIC WING

GIDE KOEKKOEK
ST.NR 1215876
May 2012

aerodynamics
Faculty of Aerospace Engineering
TUDelft
Delft University of Technology
LUND UNIVERSITY

RoBat

Experimental investigation of a bat inspired robotic wing

Master of Science Thesis

For obtaining the degree of Master of Science in Aerospace
Engineering at Delft University of Technology

Gide Koekkoek

May 2012

Faculty of Aerospace Engineering: Delft University of Technology
Faculty of Theoretical Ecology: Lund University

DELFT UNIVERSITY OF TECHNOLOGY
AEROSPACE ENGINEERING DEPARTMENT OF AERODYNAMICS

THE UNDERSIGNED HEREBY CERTIFY THAT THEY HAVE READ AND RECOMMEND TO THE FACULTY OF AEROSPACE ENGINEERING FOR ACCEPTANCE THE THESIS ENTITLED **"ROBAT"** BY **GIDE KOEKKOEK** IN FULFILLMENT OF THE REQUIREMENTS FOR THE DEGREE OF **MASTER OF SCIENCE**.

DATED: MAY 22, 2012

SUPERVISORS:

PROF. DR. IR. H. BIJL

DR. IR. B. W. VAN OUDHEUSDEN

DR. IR. F. T. MUIJRES

DR. IR. J. F. L. GOOSEN

Preface

For the final stage of the study Aerospace Engineering, I've performed the research described in this Master Thesis. The time spend on this thesis can best be described as a journey, both figurative and literally. Figurative stands for the different phases that were sometimes challenging but always inspiring. Literally refers to the fact that most of the work for this thesis is performed at the University of Lund in Sweden. Here I've found the great combination of aerodynamics and biology in the research of bat flight. The combination of theoretical knowledge, practical robotics and experimental aerodynamics gave me the motivation to perform this study.

Not only the objective of this thesis gave me the motivation, but also to great extent the support of all my friends, family and colleagues. They made it possible to write this thesis. In particular my mentor Florian Muijres was always there for me when I needed help and he guided me in the right direction. Next to that Melanie Stuiver gave me a kick-start with the work she had performed for her master thesis and despite his busy schedule Anders Hedenström always made time for me. I would also like to thank all the new friends who made me feel at home in Sweden. During my stay in Sweden, my supervisor Bas van Oudheusden gave me the needed help for the most difficult issues using e-mail conversations. Back in the Netherlands gave me the support and feedback to write and finalize this thesis. I would like to express special gratitude for both. Last but certainly not least I would like to thank my girlfriend for the support and the effort she put into our relationship during my stay in Sweden.

Summary

The research done on bat flight has increased the knowledge about bat flight and the corresponding aerodynamic phenomena in great extent. In the mid seventies and eighties, the first kinematic studies by Norberg (1976a,b) and Aldridge (1986, 1987) were performed with the use of high speed cameras and made it possible to analyze the kinematics of bat flight in great detail. These studies were first performed in flight corridors, later followed by measurements in windtunnels (Busse von, 2011). This made it possible to measure over a range of flight speeds, which shows a gradual change in kinematics when flight speed is increased. Aerodynamic measurements were the next step in bat flight research and gave a better insight in the vortex structure of bat flight both onwing (Muijres et al., 2008) and in the wake (Hedenstrom et al., 2007, 2009; Johansson et al., 2008).

All these measurements are performed with living animals. These animals are hard to train, making the measurements and preparation time consuming. Another disadvantage of living animals is that it is hard to control them with respect to position, acceleration and other flight parameters. This makes it difficult to perform repeatable measurements and find the influence of single parameters such as flapping angle or Reynolds number. A robotic flapping wing inspired on bat flight will not have these problems and is thereby a valuable addition in the bat flight research. In other fields such as bird and insect flight research, these robotic flappers have already proven to be of great potential (Dickinson et al., 1999; Hubel and Tropea, 2008) however in bat flight only preliminary results are made (such as the BATMAV (Bunget, 2010)) with robotic wings. The bat inspired model for gliding flight described by Stuiver (2011) is used as starting point for this project.

The RoBat used in this project is designed, produced and tested in a windtunnel . The RoBat is inspired by bat flight and is capable of performing a flapping, pitching and leading edge flap (LEF) rotation. This is a simplification with respect to the real bat motions because the yawing, contracting and active deformations are neglected. The RoBat consists of three servo motors, one for each motion, and is constructed from carbon fiber reinforced rods and natural rubber skin to resemble the mechanical properties of a real bat wing.

In a windtunnel the kinematics are recorded using two high speed cameras and aerodynamic measurements are performed using 2D PIV. The measured kinematics of the RoBat are compared with kinematics from real bats and show a good resemblance in flapping, pitching and LEF rotation. The absence of the other motions and deformations is clearly visible in the kinematic measurements but due to an optimization of the angle of attack, inflow angle and inflow velocity, these values are comparable with bat flight. However the angle of attack at the start of the downstroke and during the upstroke is lower than found in bat flight. This is most likely caused by deformations of the wing which are not incorporated in the optimization of the motions.

When using the wake measurements it is shown that the circulation coefficients of the vortices are in the same order of magnitude. However the circulation coefficient of the tip vortex was too low during the first half of the downstroke and the upstroke. This combined with the too high circulation of the reversed vortex during the upstroke, made the lift production lower than found in real bat flight. The wake measurements are also used to find the influence of the LEF rotation on lift production, but no evidence could be found for a positive effect of the LEF rotation on the lift production. It could still be that bats use the LEF rotation to increase flight performance because the model might not be able to capture the complexity needed for this effect.

The onwing measurements are used to show the resemblance with real bat flight and give information on the effect of angle of attack, Reynolds number, Strouhal number and Rossby number on the leading edge vortex (LEV). Similar to bat flight, the model shows no LEV at high speeds and low angles of attack. For lower velocities and their corresponding higher angles of attack a LEV starts to occur and grow. With the RoBat measurements were also performed outside the steady flight envelope of bats. They show that the LEV can also be used to increase lift production at high speeds by increasing the angle of attack. Bats will not use this in steady flight because of the increased drag but might use it in maneuvers that require a high lift force, such as sharp turns.

Using the onwing measurements, the relation between angle of attack and circulation coefficient is clearly visible because the circulation coefficient increases almost linear with the angle of attack and remains more or less constant for a constant angle of attack. No clear relation between Reynolds number and circulation coefficient is found because the circulation coefficient increases at an almost constant Reynolds number and remains constant for a changing Reynolds number. The same is valid for Strouhal and Rossby number. The vortex area seems to be Strouhal dependent because this area is increasing almost linear for a decreasing Strouhal number.

Contents

1 Introduction 27

1.1 The objective of this thesis . . . 27

1.2 Used definitions for bat wings and bat flight . . . 28

1.2.1 Anatomy of the bat wing . . . 28

1.2.2 Motions of the bat wing . . . 29

1.2.3 Angles of bat flight . . . 29

1.3 Existing biomimetic mechanical flappers for research purpose . . . 30

1.4 Thesis structure . . . 31

2 Overview of the research literature on bat flight 33

2.1 Kinematic observations using flight corridors. . . . 33

2.2 Kinematic observations using wind tunnel tests. . . . 34

2.3 Aerodynamic observations . . . 35

2.4 Linking kinematic to aerodynamic observations . . . 39

2.5 Mechanical aspects of bat wings . . . 41

2.5.1 Wing membrane properties . . . 41

2.5.2 Bone properties . . . 42

3 Modeling of bat flight 43

3.1 The seven separate motions of bat flight . . . 43

3.2 Aerodynamic requirements and their relation with the motions . . . 44

3.3 Mechanical requirements . . . 46

3.4 Mathematical model of bat flight . . . 47

4 Conceptional design of the RoBat 51
4.1 Selection of degrees of freedom 51
4.2 Concept generation 55
4.3 Concept selection 57
4.4 Scaling of the mechanical model 58
Scale selection 61

5 Detailed design of the RoBat 63
5.1 Wing design 63
5.2 Optimization of the kinematics 66
5.3 Drive design 67
5.4 Electronic design 69
5.5 Software design 69

6 Test set-up 71
6.1 Windtunnel 71
6.2 PIV system 72
6.3 Kinematics cameras 72
6.4 Test set-up 73
6.5 The measurement sequences 73
Wake measurements 73
Onwing measurements 74

7 Data analysis 75
7.1 Wake kinematic data 75
7.2 Wake PIV data 78
7.3 Onwing kinematic data 81
7.4 Onwing PIV data 81

8 Results 83
8.1 Evaluation of the RoBat wing kinematics 83
8.1.1 The influence of aerodynamic and inertia forces 87
8.2 Aerodynamic analysis of the RoBat wing flow field. 89
8.2.1 Comparison of the RoBat wing flow field with respect to real bats. 89
Comparison of the 3D representation of the vorticity iso-surfaces 89
Comparison of the circulation coefficients 92
8.2.2 The influence of the leading edge flap on the aerodynamic performance 93
8.3 Onwing measurements results 95
8.3.1 Description of the flow field 95
8.3.2 Vortex dynamics 97

9 Conclusions and recommendations 99

9.1 Wake measurements . . . 100

9.2 Onwing measurements . . . 100

Bibliography 103

A Design option tree 107

B Design options part A: flapping motion 109

C Design options part B: pitching and LEF rotation 111

D LEF and no LEF motion compared using the force production 113

E Raw Data Examples 115

F Stroke plane angle controls leading edge vortex in a bat-inspired flapper 119

List of Figures

1.1 Anatomy and reference system definition 28

1.2 Angle definitions for bat flight 29

1.3 a) Robofly layout (Dickinson et al., 1999),b) goose inspired model (Hubel and Tropea, 2010) 30

1.4 The BATMAV with detailed views of the two joints (a) and the test set-up (b).(Bunget, 2012) 31

1.5 3D rendering of the gliding bat model designed by Stuiver (a) and a detailed view of the adjustable leading edge flap system (b). (Stuiver, 2011) 31

2.1 Typical wing tip paths of a bat seen from the side (left) and the top (right), (Hedenstrom et al., 2009) 34

2.2 Used markers (a-n) on the lower side of a bat flying at 3.2 m/s obtained from high-speed recordings. (Riskin et al., 2008) 35

2.3 36

2.4 Illustration of the clap (A,B and C) and fling (D, E, F). Black lines show flow lines, dark blue arrows show induced velocity and light blue arrows show net forces acting on the airfoil.(Sane, 2003) 37

2.5 Iso-surfaces of normalized constant streamwise vorticity of (a) *Glossophaga soricina* and (b) *Leptonycteris curasoae*. The x-axis represents the time domain with five stroke phases: bd (beginning downstroke), md (mid downstroke), ed (end of downstroke), mu (mid upstroke), eu (end of upstroke). (Hedenstrom et al., 2009) 38

2.6 Velocity and vorticity fields around a bat wing in forward speed (1 m/s). The vorticity is scaled according to the color bar with a range from -1750 to +1750 s^{-1}. The local wing profile and its relative motion is shown with a red curve and arrows. (Muijres et al., 2008) . 38

2.7 Correlation between normalized circulation and angle of attack (a) and camber (b). (Wolf et al., 2009) 40

2.8 Stress-strain curve of a representative piece of bat wing skin. (Swartz et al., 1996) 41

2.9 Anatomy of a bat's wing 42

3.1 Definitions of the 7 used motions in (a) the cross section of the wing, (b) the side-view and (c) the top view. I: LEF rotation, II: active camber, III: flapping, IV: pitching motion, V: rear leg motion, VI: yawing, VII: contraction. 44

3.2 Definition of aerodynamic forces . . . 45

3.3 Measured (thin line) and modeled (thick line) kinematics for the wingtip (blue), wrist (red), tip fifth digit (green) and body (black). Dotted lines are the upstroke and solid lines the downstroke. . . . 48

3.4 Comparison between bats and the model for the angle of attack (a) and effective velocity (b) at the midpoint of triangle "wingtip-wrist-fifth digit tip". The model consist of four different motions: flapping, pitching, yawing and contraction . . . 49

3.5 Comparison between the bats and the model for the angle (a) and magnitude (b) of the effective velocity at the wrist. The model consist of four different motions: flapping, pitching, yawing and contraction . . . 49

4.1 Deflection angles of the leading edge flap (a) and camber variation (b) during one period . . . 52

4.2 Angle of attack (a) and effective velocity (b) at the midpoint of the triangle, spanned by the wrist, wing tip and tip of the fifth digit, for four different combinations of flapping (A), pitching (B), yawing (C) and contraction (D) . . . 53

4.3 Angle (a) and magnitude (b) of effective velocity at the wrist for four different combinations of flapping (A), pitching (B), yawing (C) and contraction (D) . . . 54

4.4 Position sketch of the RoBat on a sidewall of the test section of the windtunnel. . . . 55

4.5 . . . 59

4.6 Effect of scaling on the required angular velocity (a) and flapping moment (b), with the boundaries derived from the servo characteristics and a safety factor equal to 1.5. . . . 61

5.1 Wing geometry of the RoBat (solid line) compared to the mean downstroke geometry of a bat wing (red dashed lines connecting the shoulder, wrist, end of fifth digit and wing tip) . . . 64

5.2 Young's modulus of natural latex sheet, for different strains. . . . 65

5.3 Optimized flapping and pitching motions together with their original sine shaped motion. . . . 66

5.4 Results of the optimized motions and the sine fit compared with the real measurements. . . . 67

5.5 Computer drawing of the drive system, with annotations of the servos and rotational axis. Red: gear, Blue: servo, Yellow: structure, Purple: bearing, Gray: axis. . . . 68

5.6 Computer drawings of the total system. Red: gear, Blue: servo, Yellow: structure, Purple: bearing, Gray: axis. . . . 68

5.7 Electrical scheme of the RoBat with the three servo motors (M1-M3) and power source (DC 7.4V) connected by the ground wire (black), the positive power wire (red) and the signal wire (yellow). . . . 69

5.8 Software design . . . 69

6.1 Layout of the Lund University wind tunnel. The direction of air movement is shown by the arrows.(Pennycuick et al., 1997) . . . 72

6.2 Test section of the windtunnel seen from above with the test set-up for the wake measurements (a) and the onwing measurements (b) with the corresponding windtunnel fixed reference system. . . . 73

7.1 Top view of the numbered markers on the RoBat wing 75

7.2 Illustration of the parallax effect. The dots represent particles in the flow, where the grey dots are particles illuminated a small time step after the black particles. From the PIV image in the middle a velocity vector field is calculated according to the image on the righthand side. 78

7.3 Stitched velocity field with blue arrows indicating the velocity of the upper domain, the red arrows of the lower domain and the black arrows the result of the stitching process in the overlap of the upper and lower domain. In sub-figure 7.3a the total field is represented and in sub-figure 7.3c and 7.3d a detailed view (as defined in sub-figure 7.3b) of the upper and lower boundaries of the overlap are shown. 79

7.4 Data acquisition of five measurements from one measurement set resulting in a mean value and its standard deviation 81

7.5 Vorticity field ($\alpha_{eff} = 48^{\circ}$ and $U_{eq} = 5.2$ m/s) with swirl strength contours (solid line) and semi circle domain (dashed line) 82

8.1 Three dimensional coordinates from the RoBat wing (dashed line), the simulation (solid line) and a bat wing (asterisks). The points showed are; the shoulder (black), the wrist (red), the wing tip (blue) and the trailing edge of the fifth digit (green). 84

8.2 Comparison between RoBat measurements, simulated values and bat measurements, showing the flap (a) and pitch (b) angle for one period. 85

8.3 Comparison between RoBat measurements, simulated values and bat measurements, using the LEF angle (a) and camber (b) for one period. 86

8.4 Comparison between RoBat measurements, simulated values and bat measurements, using the angle of attack (a), inflow velocity (b) and inflow angle (c) for one period. 86

8.5 Comparison between 0.5 Hz and 2.5 Hz flapping motion using the flap (a) and pitch (b) angle for one period. 87

8.6 Comparison between 0.5 Hz and 2.5 Hz flapping motion using the LEF angle (a) and camber (b) for one period. 88

8.7 Four views of the iso-surfaces (cut-off value = $60s^{-1}$) of the streamwise component of vorticity in the wake of a *Leptonycteris yerbabuenae* for one wingbeat at a flight speed of 6.3 m/s. Positive vorticity is colored red and negative blue.(Muijres et al., 2011) 90

8.8 Four views of the iso-surfaces (cut-off value = $30s^{-1}$) of the streamwise component of vorticity in the wake of the RoBat for one wingbeat at an equivalent flight speed of 5.1 m/s. Positive vorticity is colored red and negative blue. In the gray area no data is available. . . 90

8.9 Four views of the iso-surfaces (cut-off value = 5% of the overall maximum) of the swirl in the wake of the RoBat for one wingbeat at an equivalent flight speed of 5.1 m/s. Positive vorticity is colored red and negative blue. In the gray area no data is available. 91

8.10 92

8.11 LEF angle over one flapping period. Measurements of the RoBat with LEF motion (solid line) and without LEF motion (dashed lines) both with standard deviation boundaries compared with the LEF angle measured at a bat wing. 93

8.12 Maximum vorticity (a) and total circulation (b) for; the tip vortex (blue), inward vortex of the dipole (red) and outward vortex of the dipole (green). Solid lines are with a LEF motion, dashed lines without. Both are with $U_{\infty} = 2.6$m/s and $\beta = 73$. All are represented with standard deviation boundaries. 94

8.13 Maximum angle of attack versus equivalent free stream velocity U_{eq} (with standard deviation error bars). Both the variable α_{eff} (lower decreasing line) and constant α_{eff} (upper horizontal line) cases are shown. The labels A-F are given for comparison with other figures. 95

8.14 Instantaneous streamlines and vorticity in the wing fixed reference system at location 1 for A: $\alpha_{eff} = 8°$, $U_{eq} = 5.0$ m/s, B: $\alpha_{eff} = 41°$, $U_{eq} = 2.0$ m/s ,C: $\alpha_{eff} = 53°$, $U_{eq} = 1.0$ m/s, D: $\alpha_{eff} = 51°$, $U_{eq} = 2.0$ m/s, E: $\alpha_{eff} = 48°$, $U_{eq} = 3.1$ m/s, F: $\alpha_{eff} = 48°$, $U_{eq} = 7.4$ m/s. 96

8.15 Negative circulation coefficient in the semicircle above the wing with respect to Re_{loc} (a), $\alpha_{eff,loc}$ (b), St_{loc} (c) and Ro_{loc} (d) with labels A-F referring to figure 8.14. The error bars represent the standard deviation. 97

8.16 Cumulative area of the vortices in the semicircle above the wing with respect to Re_{loc} (a), $\alpha_{eff,loc}$ (b), St_{loc} (c) and Ro_{loc} (d) , with labels A-F referring to figure 8.14. The error bars represent the standard deviation. 98

A.1 Design option tree for the flapping motion. ^{1}Not possible, ^{2}Better option when the rotational axis is located on the wind tunnel boundary. 108

A.2 Design option tree for the pitching and LEF rotation motions 108

B.1 Sketches of the three possible concepts for the flapping motion 110

C.1 Sketches of the six possible concepts for the pitching and LEF rotation 112

E.1 Four frames of one kinematic camera at frame number 0, 17, 33, 50 from total range of 0 to 100 starting at the upper most point at frame 0 ($U_\infty = 2.5$m/s, $\beta = 83°$). 116

E.2 Four frames of the lower PIV camera at frame number 10, 20, 30 and 40 from total range of 0 to 80 starting at the upper most point at frame 0 ($U_\infty = 2.5$m/s, $\beta = 83°$). 117

E.3 Four frames of one PIV camera at frame number 24 to 27 from total range of 0 to 80 starting at the upper most point at frame 0 ($U_\infty = 2.5$m/s, $\beta = 83°$). Used frame for onwing postprocessing is frame 26. 118

List of Tables

2.1 Mechanical properties of the wing membrane in the direction of most fibers (0 degree) and perpendicular to that (90 degrees).(Swartz et al., 1996) 41

2.2 Diameter of most important bones of a bat of 22 grams. DV = dorsventral and ML = mediolateral. (Swartz and Middleton, 2008) 42

3.1 Connection between kinematic motions and aerodynamic parameters (X: minor influence, XX: major influence) 46

3.3 Sinusoidal fit of the four modeled motions 48

4.1 Selection of the first motion, flapping. Sketches of these three concepts can be found in figure B.1. Grading from very bad (–) to very good (++). 57

4.2 Selection of the second and third motions, pitching and LEF rotation. Sketches of these six concepts can be found in figure C.1. Grading from very bad (–) to very good (++). 57

5.1 Comparison between bat bones, RoBat bones and desired RoBat bones.(*(Mat, 2012),**(dpp pultrusion, 2011)) 64

6.1 Overview of the ten measurement configurations used for the wake measurements. 74

6.2 Overview of the ten measurement configurations used for the onwing measurements. 74

D.1 Force production [mN] for all three vortices together 114

D.2 Force production [mN] for the tip vortex 114

D.3 Force production [mN] for the inward vortex of the dipole vortex structure 114

D.4 Force production [mN] for the outward vortex of the dipole vortex structure 114

Nomenclature

Abbreviations

AoA	Angle of Attack
AR	Aspect Ratio
$BATMAV$	Bat inspired Micro Air Vehicle
DV	Dorsventral
LEF	Leading Edge Flap
LEV	Leading Edge Vortex
MAV	Micro Air Vehicle
ML	Mediolateral
PCI	Peripheral Component Interconnect
PhD	Doctor of Philosophy
PIV	Particle Image Velocimetry
POD	Proper Orthogonal Decomposition
RC	Radio Control
$RoBat$	Robotic Batwing
TS	Tensile Strength
USB	Universal Serial Bus
$Yield$	Mass per square meter

Greek Symbols

$\alpha_{eff,max}$	Maximum angle of attack
α_{eff}	Effective angle of attack
α_{flap}	Inflow angle
α_{LEF}	LEF angle

β	Stroke plane angle
$\ddot{\theta}$	Angular acceleration
$\ddot{\theta}_{max}$	Maximum angular acceleration
$\dot{\theta}$	Rotational flapping velocity
$\dot{\theta}_{loc}$	Local angular verlocity
$\dot{\theta}_{max}$	Maximum angular flapping velocity
γ	Body angle
Γ_{vort}	Circulation of a vortex
$\Gamma_{vort}^{'}$	Underestimated circulation of a vortex
λ_{ci}	Swirling strength
ν	Kinematic viscosity
ω	Vorticity
ω_{max}	Maximum vorticity
ω_{min}	Minimum vorticity
ρ	Density
σ	Stress
θ	Flapping angle
θ_{el}	Elastic deformation angle
θ_{flap}	Flapping angle
θ_{max}	Maximum flapping angle
θ_{pitch}	Pitching angle
ε	Strain

Latin Symbols

Δy	Offset from the mass center of the servo to the rotation axis
$\mathbf{C}$	Centroid vector
$\mathbf{n_{1-3}}$	Surface normals
$\mathbf{p_{1-8}}$	Vectors representing the markers 1 to 8
$\mathbf{V_c}$	Centroid velocity
$\triangle h$	Distance between the wing cross section and the chord line, normal to the chord line
$\triangle t$	Time increment
$\triangle x$	Spatial increment

$\triangle y$	Offset in y direction
A	Amplitude
a	Acceleration
A_0	Original amplitude
b	Semispan
b_{loc}	Local semi-span
b_{vort}	Semi-span of the vortices
c_Γ	Circulation coefficient
c_D	Drag coefficient
$c_{L\alpha}$	Slope of the c_L - α curve
$c_{l_{max}}$	Maximum c_l
c_{loc}	Local chord
C_l	Lift coefficient (2D)
c_L	Lift coefficient (3D)
D	Drag force
D	Gradient tensor
d	Diameter
E	Young's modulus
F	Force
f	Frequency
F_{aero}	Aerodynamic force
$F_{elastic}$	Elastic forces
F_{hor}	Horizontal component of total aerodynamic force
$F_{inertia}$	Inertia forces
F_{ver}	Vertical component of the total aerodynamic force
F_{vort}	Force corresponding with a vortex
g	Gravitational acceleration
h	Camber
h_{max}	Maximum camber
h_{mean}	Mean camber

$I-V$	Numbering fingers I for thumb, V for pink
$I-VII$	Numbering of motions
I_2	Area moment of inertia
I_{bones}	Mass moment of inertia of the bones
$I_{membrane}$	Mass moment of inertia of the membrane
I_{servo}	Mass moment of inertia of the servo's
I_{tot}	Total mass moment of inertia
k_{flap}	Model constant for flap angle
k_{pitch}	Model constant for pitch angle
L	Lift force
l	Length
M	Moment
m	Mass
M_{aero}	Aerodynamic moment
m_{bat}	Mass bat
m_{servo}	Mass of the servo's
p	Period
p_0	Original period
R	Rotational matrix
r^2	Coefficient of determination
Re	Reynolds number
Re_{loc}	Local Reynolds number
Re_{tip}	Reynolds number of the tip of the wing
Ro_{loc}	Local Rossby number
S	Surface
s	Second
S_{vort}	Vortex area
St	Strouhal number
St_{loc}	Local Strouhal number
St_{tip}	Strouhal number of the tip of the wing
t	Thickness

t	Time
t_{bat}	Thickness of the membrane of the bat
t_{model}	Thickness of the membrane of the model
u_x	X-component of the velocity
U_{∞,eff_x}	X- component of the effective freestream velocity
U_{∞,eff_z}	Z- component of the effective freestream velocity
$U_{\infty,eff}$	Effective freestream velocity
U_∞	Free stream velocity
U_{bat}	Young's modulus of the bat
U_{eq}	Equivalent freestream velocity
$U_{flap,x}$	X-component of the flap induced velocity
$U_{flap,y}$	Y-component of the flap induced velocity
$U_{flap,z}$	Z-component of the flap induced velocity
U_{flap}	Flap induced velocity
U_{model}	Young's modulus of the model
U_{wing}	Wing velocity
$U_{x,wing}$	Local x-component of the wing velocity
$U_{z,wing}$	Local z-component of the wing velocity
W_{bat}	Weigth bat

CHAPTER 1

Introduction

Bats have inspired people for a long time. For example the first uncontrolled heavier-than-air flyer, designed in 1890 by Clément Ader, was inspired by bats (Anderson, 2001). Clément used the geometry and bone structure of bats for a fixed wing configuration. Later, under influence of the Wright brothers, the shape of airplane wings became more rectangular with a different structure and the interest in bat flight decreased. However with the advent of high speed cameras the interest in bat flight returned in the seventies and eighties (Norberg, 1976a,b; Aldridge, 1986, 1987). It was now possible to record the motion of a bat while flying and analyze the kinematics afterwards. At first these measurements were done in flight corridors followed by windtunnel tests. Aerodynamic measurements were the next step in bat flight research in flight corridors as well as windtunnels, mostly using particle image velocimitry (PIV) (Hedenstrom et al., 2007; Johansson et al., 2008; Muijres et al., 2008; Hedenstrom et al., 2009; Muijres et al., 2011). Now it is possible to measure both kinematics and aerodynamics at the same time, making it possible to find relations between them and thereby getting a better understanding of bat flight (Tian et al., 2006; Hubel et al., 2009).

1.1 The objective of this thesis

The difficulty with these kind of measurements are that they are done with unpredictable living animals. This means training is necessary and even then it is time consuming to obtain accurate measurements because location, velocity and accelerations are hard to control. Another problem with living animals arises when the influence of a single flight parameters (flight speed, flapping frequency, flapping amplitude or stroke plane angle) or a single dimensionless number (Reynolds, Rossby or Strouhal number) has to be investigated. Changing one of those parameters in a systematic way is almost impossible with living bats. A mechanical flapper that mimics the motion of a bat's wing will make it possible to change the flight parameters and dimensionless numbers in a much larger range to explore bat flight. This is even possible outside the actual flight envelope. A mechanical flapper also makes it possible to accurately control the location of the wing in a wind tunnel and keep the accelerations of the body equal to zero resulting in a steady state flight. As a consequence, this reduces measurement time and increases repeatability.

With these advantages, the objective of this project is to design and produce a mechanical flapper (the RoBat) that will be able to mimic the motion and aerodynamics of a real bat wing. This RoBat will be used to obtain more insight in the aerodynamics of bat flight and bat inspired flight. In this study the influence of the leading edge flap on the circulation in the wake will be discussed, followed by a study about the influence of Reynolds, Rossby and Strouhal number on the leading edge vortex (LEV).

1.2 Used definitions for bat wings and bat flight

To increase clarity, definitions will be given of the most important bat wing anatomy, motions of a bat wing and used angles of bat flight.

1.2.1 Anatomy of the bat wing

In figure 1.1a the bone structure of a bat wing is shown. In the upper left corner, the shoulder is shown with a connection to the Humerus. This bone is connected to the Radius through the elbow of the bat. All the fingers of the wing are connected to the Carpals, or the wrist. The fingers, with the exception of the first digit, consist of four bones starting from the tip with the Distal, Middle and Proximal phalanx finished by the Metacarpels that is connected to the Carpals (figure 1.1a).

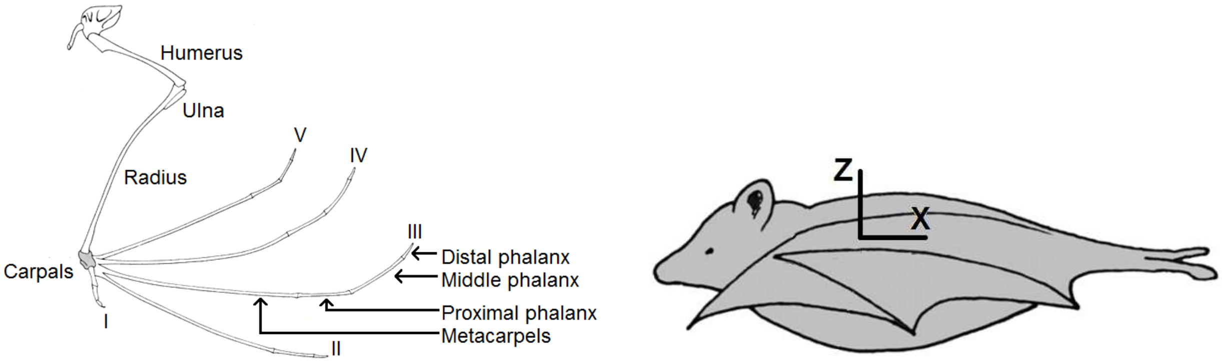

(a) Anatomy of a bat wing

(b) Bat with body fixed reference system, positioned at the shoulder.

Figure 1.1 – Anatomy and reference system definition

1.2.2 Motions of the bat wing

To define the motions of a bat wing, a body fixed reference system is defined at the shoulder of the bat. This reference system can be seen in figure 1.1b, where the bat is flying to the left, with the x-axis pointing to the rear, the z-axis up and the y-axis out of plane in this picture or to the left seen from the bats point of view. The shoulder of a bat moves with respect to the rest of the body because of body muscles (Riskin et al., 2008), but for simplicity this movement is neglected resulting in a body fixed reference system located at the shoulder. With this body fixed reference system two motions of the wing can be defined. The flapping motion which is a rotation around the x-axis and the yaw motion which is a rotation around the z-axis. For the definition of the pitching motion a second reference system is necessary, one that is wing fixed instead of body fixed. This reference frame is also positioned at the shoulder, but in this case rotates around it's origin following the wing for the yawing and flapping motions. The wing and body fixed reference systems are identical when the wing is at it's mean position. The pitching motion is defined as the rotation around the y-axis of this wing fixed reference system. Finally, the contracting motion is a change in the length of the line between the wrist and the shoulder of the bat wing.

1.2.3 Angles of bat flight

To be able to define the orientation of the bat and the RoBat flapper, three angles are stated in figure 1.2. Firstly the body angle (γ) which is the angle between the horizontal and the line through the shoulder and hip of the bat. Secondly the stroke plane angle (β), which is the angle between the horizontal and the line between the most upper and lower position of the wingtip, seen from the side. The last angle defined in this section is the effective angle of attack (α_{eff}), which is the angle between the chordline and the effective freestream velocity ($U_{\infty,eff}$). Where $U_{\infty,eff}$ is the resultant of the free stream velocity and flapping velocity of the wing.

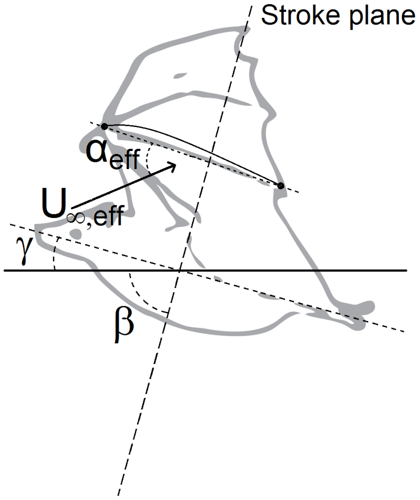

Figure 1.2 – Angle definitions for bat flight

1.3 Existing biomimetic mechanical flappers for research purpose

Because only a few mechanical flappers are described in the literature, insect and bird inspired flappers are also discussed and used as inspiration for the RoBat. The best documented insect model is the Robofly from Dickinson et al. (1999). This model is inspired by a fruit fly and is scaled to make production and measurements easier. The model consist of two stiff Plexiglas wings and each wing is capable of rotational motion about three axes. This model is powered by stepper motors and the motion is transmitted with coaxial drive shafts and a gearbox (figure 1.3a). The used flapping frequency is equal to 145 mHz.

Hubel and Tropea (2010) give a description of a goose inspired model (figure 1.3b). This model can perform a flapping motion and the pitch angle is manually adjustable. The span of this model is equal to 1130mm and the wings are made from glasfiber epoxy and assumed to be rigid. The pitching motion is powered by a direct current motor. The maximum frequency of this model is equal to 2.2 Hz.

Less research is done using bat inspired models but the BATMAV is one very promising model (Bunget, 2010)(figure 1.4). The BATMAV is powered by electrically stimulated shape memory alloy wires acting as the muscles of two joints (the shoulder and elbow joint) allowing a combined flapping, pitching, yawing and contraction motion. The desired frequency is between 8 and 11 Hz but this is not yet reached with the current model. The kinematics of this model are optimized using kinematic measurements of real bats.

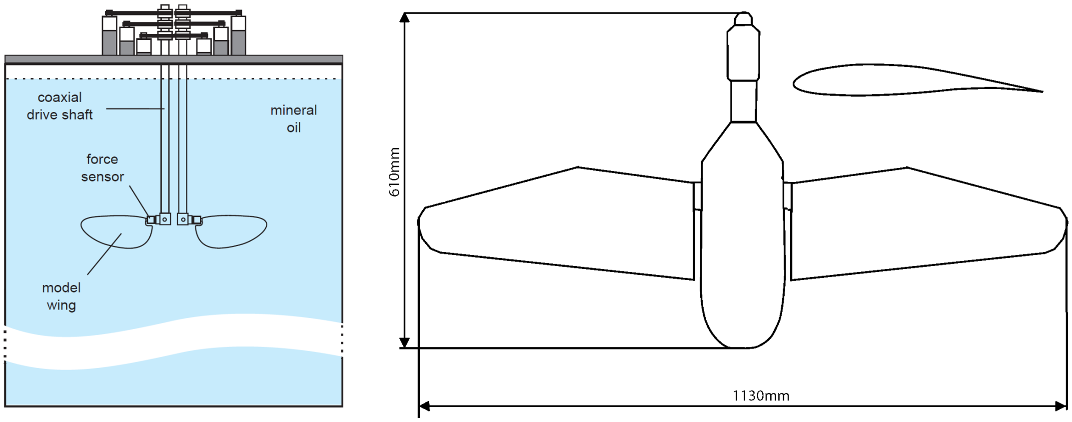

(a) (b)

Figure 1.3 – a) Robofly layout (Dickinson et al., 1999),b) goose inspired model (Hubel and Tropea, 2010)

The model inspired by bats, designed and tested by Stuiver (2011), is used as starting point for this project. This model is optimized for gliding flight but also had the objective of being expanded to a flapping model. The model uses a flexible carbon structure and plastic wing membrane which are designed to be comparable to wing bones and membrane (figure 1.5a). With this model it is possible to change the leading edge flap (LEF) angle manually (figure 1.5b), making it possible to find the influence of this LEF while gliding. The model shows comparable but lower lift coefficients compared to real gliding bats. Also the lift over drag ratio, equal to 6.5, is lower than the 7.5 found with real gliding bats. It is however in the same order of magnitude. It was found that the LEF deflection increased both the lift coefficient and the stall angle.

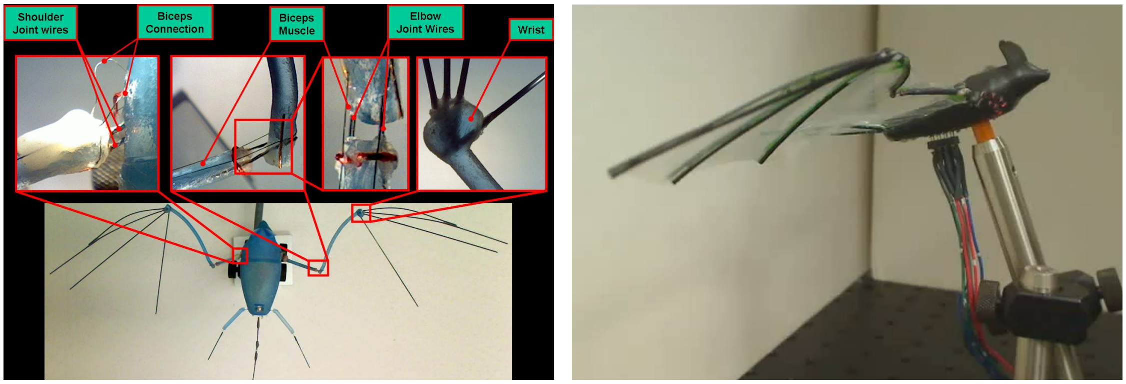

(a) (b)

Figure 1.4 – The BATMAV with detailed views of the two joints (a) and the test set-up (b).(Bunget, 2012)

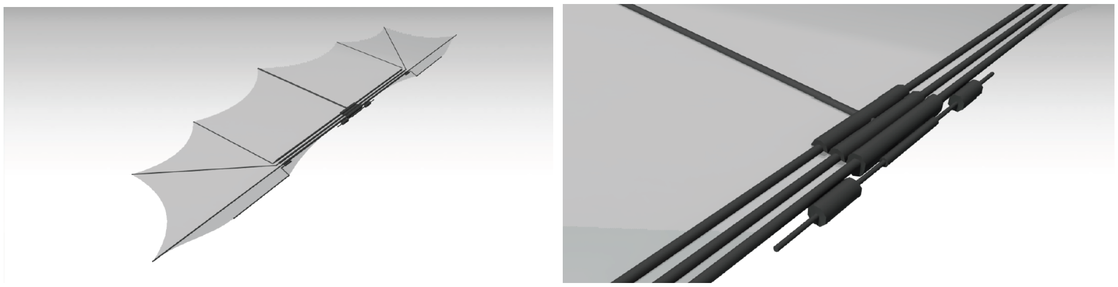

(a) (b)

Figure 1.5 – 3D rendering of the gliding bat model designed by Stuiver (a) and a detailed view of the adjustable leading edge flap system (b). (Stuiver, 2011)

1.4 Thesis structure

This report continues with the research literature on bat flight which is discussed in chapter 2. This is done for the kinematics, followed by the aerodynamics and the mechanical properties of bat wings. In chapter 3 this literature study is used to define the requirements for the RoBat and a description of the mathematical model is given that is used for prediction and optimization of the kinematics. The next chapter (chapter 4) describes the conceptual design decisions followed by the detailed design in chapter 5. This RoBat design is constructed and tested in a windtunnel, which is described in chapter 6. In chapter 7 the analysis of the data obtained from these tests is described followed by the results in chapter 8. These results are divided into the evaluation of the RoBat model, the results of measurements in the wake and the results of the onwing measurements. This report will finalized by the conclusions and recommendations in chapter 9. Part of the research performed for this study is also published in the the special edition 'Biomimetic flow control' of the journal 'Comptes Rendus Mecanique' (Koekkoek et al., 2012). This publication can be found as attachment F.

CHAPTER 2

Overview of the research literature on bat flight

2.1 Kinematic observations using flight corridors.

With the use of stroboscopic photogrammetry and later high speed cameras it is possible to track the motion of a bat and analyze the results. Aldridge (1986) used one bat (*Rhinolophus ferrumequinum*) with a span of 36 cm and a mass equal to 22 grams, flying in a flight corridor to study the kinematics using stroboscopic photogrammetry with a frequency of 100Hz. From this stroboscopic pictures the three dimensional coordinates were calculate for 6 tracking points. Aldridge found a gradual change in kinematics with increasing speed, the wingbeat frequency decreases and stroke plane angle increases. Later Aldridge found that three different patterns could be distinguished. At low speeds a tip-reversal during the upstroke is used for extra lift generation, at medium speeds lift is still generated but without the tip-reversal and at high speeds negative thrust, or drag is generated during the upstroke (Aldridge, 1987). A comparable test set-up was used by Norberg (Norberg, 1976a,b) to find the lift coefficients of forward flight and hover for the species *Plecotus Auritus* which has a span of 27 cm and a mass of 9 grams. These were calculated using quasi steady state aerodynamics, assuming steady horizontal flight. The lift coefficients are calculated using the fact that the sum of the vertical components of the lift and drag force must be equal to the weight of the bat. The directions of the lift and drag forces are respectively perpendicular and parallel to the effective velocity. This effective velocity is the sum of the flapping velocity, induced velocity and the flight speed. Where only the velocity components normal to the line from the shoulder to the wing tip are used. Norberg determined the flapping velocity from the film data, where the downstroke and $^2/_3$ of the upstroke is assumed to be a sin shaped motion. The induced velocity is calculated using the actuator disc momentum theory, assuming a constant induced velocity over the total wingbeat. Both velocities are determined for the midpoints of three different sections on the wing. The lift coefficients found were 1.4 - 1.6 for slow flight (Norberg, 1976a) and 3.1 - 6.4 for hover (Norberg, 1976b). The lift coefficients found for hover cannot be reached by steady state aerodynamics, which proves bats have to use unsteady aerodynamic phenomena during hover and slow flight.

2.2 Kinematic observations using wind tunnel tests.

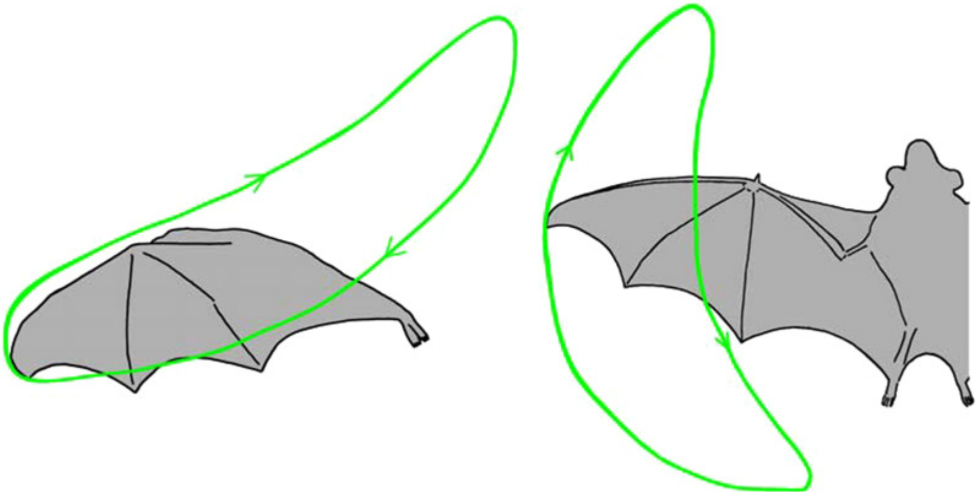

Figure 2.1 – Typical wing tip paths of a bat seen from the side (left) and the top (right), (Hedenstrom et al., 2009)

The use of a wind tunnel for kinematic observations resulted in measurements over a wide range of speeds and a better understanding of the different phases of bat flight. At low speeds, the kinematics of the wing tip shows a rotating motion with a large yawing and contracting part (see figure 2.1) and high angles of attack (positive during downstroke and negative during upstroke). Also the camber and leading edge flap angle show large variations. With increasing speed the contraction and yawing motions become less present resulting in a more straight flapping motion. The maximum angle of attack, variation in camber and frequency decreases with increasing flight speed (Busse von, 2011).

The number of markers used to track kinematics are different for the studies described in this chapter and it can be expected that with more markers, a larger part of the motion is captured. Furthermore the location of the markers is of great importance. To be able to select the best set of markers Riskin et al. (2008) tracked the kinematics of 7 female bats (*Cynopterus brachyotis*) at 9 different speeds using 17 markers and used proper orthogonal decomposition (POD) to quantify the amount of motion captured for each marker. The used markers are shown on one bat as example in figure 2.2. Combining the data of the 9 different speeds, they found the following order of markers (from most important to least important):

- Wrist (e)
- Wing tip (h)
- Elbow (d)
- Rear leg (p)
- Three more points on the 3th and 4th finger (k,f,j)
- Point half way the 5th finger (l)
- Two more points on the 3th and 4th finger (i,g)
- Two more points on the 5th finger (n,m)

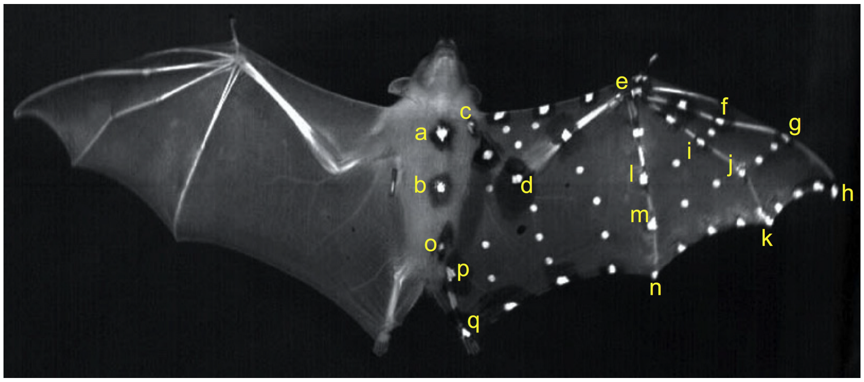

Figure 2.2 – Used markers (a-n) on the lower side of a bat flying at 3.2 m/s obtained from high-speed recordings. (Riskin et al., 2008)

It is important to note that this order is purely based on kinematics, which could mean that the importance of small motions with great influence on the aerodynamics, such as change in camber and pitching angle, might be underestimated.

2.3 Aerodynamic observations

To be able to understand the aerodynamics of bat flight four main unsteady aerodynamic effects present in low Reynolds number ($Re = 10^2 - 10^5$) flapping flight will be discussed, followed by a description of the recent literature on aerodynamics of bat flight.

Leading edge vortex In the Reynolds range for insects ($Re = 10^2 - 10^4$ (Lentink and Dickinson, 2009)) and small birds and bats ($Re = 10^3 - 10^5$ (Hedenstrom et al., 2007)), laminar separation is a common phenomena. For a two dimensional stationary wing, laminar separation leads to leading edge stall at high angles of attack during which laminar separation bubble may occur (a stable LEV) at medium angles of attack when the flow reattaches (as can be seen in figure 2.3b). For a three dimensional wing, the stable LEV can also occur at extreme high angles of attack due to sweep or a flapping motion. For swept wings, separation occurs at angles of attack as high as 35 degrees, compared to 10 degrees for non-swept wings. For swept wings, this also results in less abrupt stall characteristics (Berg van den and Ellington, 1997). The spanwise component of the free stream velocity results in a axial flow in the LEV which has a stabilizing effect for swept wings. It has been suggested that this axial flow might also be important for stabilizing the LEV on insect and bat wings (Ellington et al., 1996; Berg van den and Ellington, 1997) although the origin of the axial flow is different for flapping flight. Here, the axial flow can be generated by centrifugal forces or a spanwise pressure distribution caused by variation in vortex size or circulation (Maxworthy, 2007). On the other hand Birch and Dickinson find only an axial flow of 1% to 4% of the tip velocity and no influence on the vortex size if this axial flow is blocked by tear shaped fences on the upper side of the wing. They propose that the downwash is reducing the effective angle of attack and thereby reducing the size of the LEV (Birch and Dickinson, 2001). Lentink and Dickinson (2009) derive that the LEV dynamics on flapping wings are influenced by three accelerations: angular, centripetal and Coriolis. These accelerations are found by transforming the Navier-Stokes equations to a rotating reference frame on the wing. Flow visualizations and force measurements on a robotic scaled wing show that the centripetal and Coriolis accelerations have a stabilizing effect in the LEF, both present at low Rossby numbers. In this paper the Rossby number is defined as the wing tip radius divide by the mean chord, which is equal to the single wing aspect ratio.

Wake capture Flapping wings can interact with the wake vortices of the previous motion. Both increased velocity due to induced velocity in the wake and vortex interaction can result in a lower or higher lift production, depending on the phase shift between the flapping and pitching motion. Dickinson et al. (1999) tested a mechanical scaled model based on a fruit fly ($Re \approx 140$). They measured the lift produced by a flapping wing and compared this to the theoretical quasi steady state aerodynamic lift derived from the prescribed kinematics. The difference between those lift forces is the unsteady part of the lift force which they call rotational lift. The value of this rotational lift during one period is showed in figure 2.3a for three different phase shifts (advanced, symmetrical or delayed pitching motion with respect to the flapping motion). Positive lift is produced for the advanced case, no extra lift is produced for the symmetrical case and negative lift is produced for the delayed case. In other words the pitch angle needs to be negative at the beginning of the downstroke for optimal lift production

Rotational circulation The Magnus effect is a well known effect in physics, describing the lift generation due to the rotation of an object while moving through a fluid. The rotation of the object will introduce circulation in the surrounding fluid and thereby generate a lift force. For a flat wing, this effect is influenced by the instantaneous angle of attack and the axis of rotation. The angle of attack when exceeding 90 degrees will result in a negative lift and the axis of rotation will influence the amount of rotation, maximum when located at the leading edge and even negative when exceeding the $3/4$ chord point (Dickinson et al., 1999). In figure 2.3a the effect of rotational circulation can be seen for different phase shifts. In contrast to wake capture, not only the sign changes when the phase shift changes but also the timing. The advanced case again has the most favorable lift production.

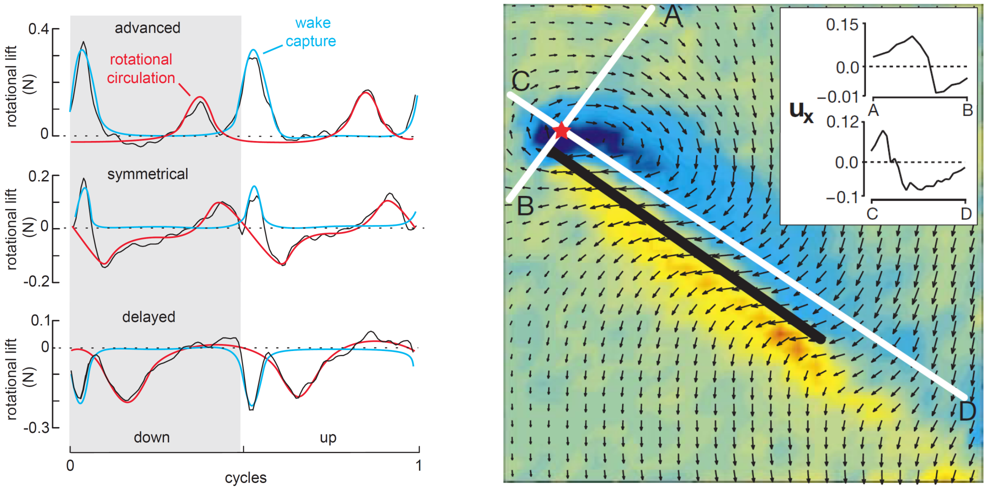

(a) Rotational lift production by an oscillating wing (black line) and proposed decomposition between rotational circulation part (red line) and wake capture part (blue line).(Dickinson et al., 1999)

(b) Leading edge vortex on a fruit fly inspired oscillating wing. Chord-wise cross-section halfway the wing at mid-stroke. The arrows represent the flow pattern and the colors the vorticity.(Birch and Dickinson, 2001)

Figure 2.3

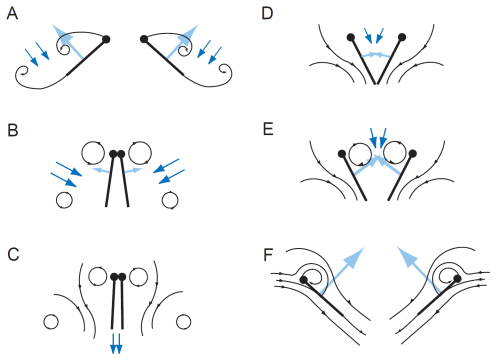

Figure 2.4 – Illustration of the clap (A,B and C) and fling (D, E, F). Black lines show flow lines, dark blue arrows show induced velocity and light blue arrows show net forces acting on the airfoil.(Sane, 2003)

Weis-Fogh's clap and fling The wings of some insects are brought together at the end of the upstroke where after they are pealed from each other at the start of the downstroke, creating a low pressure on the upper side of the wings (Weis-Fogh, 1973). A nicely illustrated description of the clap and fling is given by Sane (2003) and is shown in figure 2.4. The wings with a LEV first touch each other at the leading edge followed by a rotation around this leading edge that completes the clap. Stopping vortices are shed from the trailing edge as can be seen in figure 2.4B. The clap produces the first additional force production by the jet at the trailing edge. The fling starts with a rotation around the trailing edge (figure 2.4D) that results in a low pressure region between the wings. This low pressure causes a suction force and is an initial boost for the leading edge vortex formed as can be seen in figure 2.4F. The overall effect is an extra lift production during the transition between up- and downstroke and thus decreasing the delay in force production during start-up.

Aerodynamics in bat flight The use of PIV has given the possibility to measure complete flow fields and thereby give a good insight in the aerodynamic characteristics of bat flight. Initially, the repetition rate (10 Hz) of the measurements was too low to get a suitable time resolution for the flapping motion (∼10 Hz). The solution for this problem was to combine measurements from multiple wingbeats and thereby reach a better time-resolution.

Hedenstrom et al. (2007) used PIV to study the aerodynamics of two adult bats (*Glossophaga soricina*, 24 cm span) in a windtunnel at speeds ranging from 1.5 to 7 m/s. They measured the velocity in a plane behind the bat orthogonal to the free stream velocity, also called far wake measurements. Using these far wake measurements they described three different bat flight modes. Note that the transitions between these modes is gradual, unlike gaits found in terrestrial locomotion:

- Slow flight (1.5 m/s): During the first part of the downstroke a strong start vortex was shedded due to the acceleration of the wing. Later at the transition between down- and upstroke a combined start and stop vortex was shed. During the upstroke, the wing is moving backwards faster than the forward velocity of the body resulting in a reversed flow. Combined with the fact that the wing hand is upside down due to a large pitch-up motion at the start of the upstroke (backwards flick), this results in an active upstroke producing lift and thrust.
- Medium flight (4 m/s): Comparable with slow speeds, there is also a strong start vortex present during the first part of the downstroke. But during the transition between down- and upstroke, the stopping vortex is much more diffuse. Also the upstroke starts comparable with the slow speed case, but without the backwards flick and at the end of the upstroke, the outer part of the wing starts to produce negative lift, resulting in a vortex dipole structure with an upwash.
- Fast flight (6.5 m/s): The high speed case is comparable with the medium speed case, with the only differences that the magnitude of the vortices is smaller and the wavelength is larger.

At all cases both wings produce a separate vortex loop consisting of the start and stop vortices connected by the tip and root vortices. This is an indication that the body generates relatively little lift.

An important remark is made by Johansson et al. (2008), to be careful with the results from far wake measurements as performed by Hedenstrom et al. (2007). Johansson and colleagues compared near (1.1 chord lengths behind the wing) and far (1.6 chord lengths behind the wing) wake measurements of two small bats (*Glossophaga soricina*) and found that the total amount of circulation is the same for both measurements, so far wake measurements are valid for calculating lift forces, but the wake structure is different. Details can be missed using far wake measurements because diffuse vortices can roll-up in one more concentrated vortex.

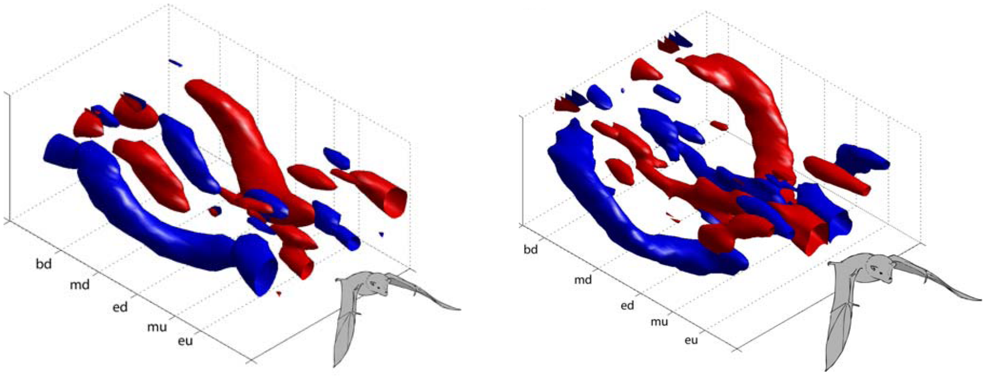

(a) (b)

Figure 2.5 – Iso-surfaces of normalized constant streamwise vorticity of (a) *Glossophaga soricina* and (b) *Leptonycteris curasoae*. The x-axis represents the time domain with five stroke phases: bd (beginning downstroke), md (mid downstroke), ed (end of downstroke), mu (mid upstroke), eu (end of upstroke). (Hedenstrom et al., 2009)

The near wake measurements from Hedenstrom et al. (2009) show more detail because, with the use of high speed stereo PIV, they could get time-resolved measurements (figure 2.5). During the first half of the downstroke, tip and root vortices are increasing in strength. During the second half of the downstroke, the strength of these vortices is constant with a clear downwash in between. This downwash together with the tip vortex is still present until mid-upstroke. In the last part of the upstroke, the tip vortex is replaced by a dipole introducing upwash and thus negative lift.

A new insight in the aerodynamics of bats was given by the onwing measurements described by Muijres et al. (2008). They reveal that the LEVs produce 40% of the lift during slow flight (1 m/s). The LEV is present during the downstroke over the complete wing span, with the highest strength near the wingtip. The LEV is stable during the downstroke, although at steady conditions the high angle of attack would cause full separation. Also evidence is found for rotational circulation, another unsteady aerodynamic effect.

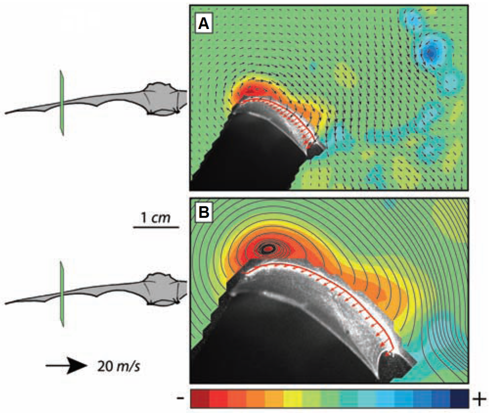

Figure 2.6 – Velocity and vorticity fields around a bat wing in forward speed (1 m/s). The vorticity is scaled according to the color bar with a range from -1750 to +1750 s^{-1}. The local wing profile and its relative motion is shown with a red curve and arrows. (Muijres et al., 2008)

2.4 Linking kinematic to aerodynamic observations

The first study where aerodynamic measurements were linked to wing kinematics and shape was carried out by Tian et al. (2006), who investigated bats flying at speeds between 2 and 3 m/s in a flight corridor. For these measurements female *Cynopterus brachyotis* bats (30 to 40cm wing span) where used. They found the same kinematics as shown in the pure kinematic studies previously mentioned and give a description of the tip or main vortex structure. This vortex follows the tip nicely during the downstroke, but is located more outward during the upstroke while the tip of the wing moves inward. They suggest that the vortex is shed from another location on the wing during the upstroke that is more outward than the wing tip, for example the fifth digit. This is in contrast with the findings of the studies described next, where a different vortex structure is found during the upstroke located around the wing tip or even more inward.

The wind tunnel study performed by Hubel et al. (2009) give more details on the vortex structure at speeds ranging from 3.5 to 5.5 m/s. They used three *Cynopterus brachyotis* bats with a wing span of 37 to 40 cm and describe a weak starting vortex at the beginning of the downstroke, followed by a more or less constant tip vortex and a weak root vortex during the rest of the downstroke and the first part of the upstroke. This root vortex is much weaker than found by Hedenstrom et al. (2007), respectively 8% compared to 50% of the strength of the tip vortex. A relative abrupt disappearance of the tip vortex at the end of the upstroke indicates a strong stopping vortex followed by some weaker vortices of different sign until the new wingbeat starts.

Another wind tunnel test performed by Hubel et al. (2010) with four *Cynopterus brachyotis* bats (wing span between 34 and 36 cm) at 5 and 6.7 m/s confirms the vortex structure found by Hedenstrom et al. (2007), but shows a less persistent root vortex. While Hedenström and colleagues find a root vortex in the complete downstroke and part of the upstroke, Hubel and colleagues only show a root vortex at the first part of the downstroke. This absence of the root vortices at the rest of the wingbeat suggests a combined system of the two wings (in contrast to the separated vortex loops found by Hedenstrom et al. (2007)). They also show little horizontal displacement of the root vortex suggesting it's related to the root of the wing. Comparable with Tian et al. (2006) a strong correlation is found between the main vortex location and the wing tip during the downstroke, but during the upstroke a different structure is found. The main vortex is more inward than the wing tip because the outer part of the wing produces a new vortex structure, a vortex dipole, producing negative lift. This discrepancy could be because of different definitions of the vortices made by Tian and Hubel.

Another study that finds correlations between kinematic and aerodynamic parameters is performed by Wolf et al. (2009). They used a male and female *Glossophaga soricina* bat to perform windtunnel tests at flight speeds of 1 to 7 m/s. At low speeds they found the use of a backwards flick, comparable to the one found by Hedenstrom et al. (2007), with thrust and some weight support as result. At higher speeds this backwards flick is not anymore used and the upstroke only produces weight support. This study also shows the variation of parameters like angle of attack, span ratio, camber and downstroke ratio with increasing flight speed which gives a strong indication for active adaption of those parameters. With increasing flight speed, both the mean and the maximum angle of attack decreases, camber decreases and both the span ratio and downstroke ratio increased from 1 to 3.5/4.5 m/s and stays constant or decreases when flight speed is further increased.

The comparison between the wake width and the wingspan shows that both increase during the first half of the downstroke followed by a decrease during the second half of the downstroke. This decrease continues during the first phase of the upstroke, but the wake shows a stronger decrease than the wingspan. The last part of the upstroke shows an increasing wake width and wingspan. Wolf and colleagues also calculated the circulation from the starting vortices and the total circulation, both showing a correlation with the angle of attack and camber as can be seen in figure 2.7.

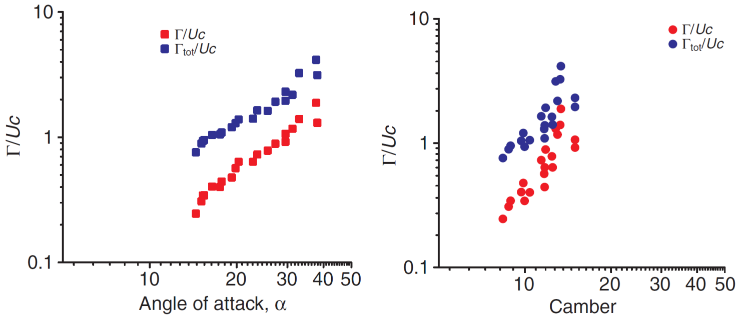

(a) **(b)**

Figure 2.7 – Correlation between normalized circulation and angle of attack (a) and camber (b). (Wolf et al., 2009)

A study focused on the interaction between kinematics and aerodynamics done by Busse von (2011) for a measurement range of 2 to 7 m/s shows a correlation between the tip vortex location and the wing tip for the down- and partly upstroke followed by a decreasing wake span and increasing wing span around mid-upstroke. Wake interaction could explain this phenomena. The root vortex is likely to be shed from the fifth finger at low speeds (2 to 3 m/s) and from the inner wing at intermediate speeds (4 to 6 m/s). Further the influence of camber, angle of attack and leading edge flap (LEF) angle on the resultant force coefficient will be described. The camber seems to show the weakest correlation with respect to the resultant force coefficient. The highest of this weak correlation seems to be at the range of 3 to 5 m/s. A stronger correlation is possibly found for the angle of attack over the total speed range, but with a time lag. This time lag suggest unsteady effects such as delayed stall. Also a correlation for the LEF angle with respect to the resultant force coefficient might be present at all speeds.

2.5 Mechanical aspects of bat wings

There are still many aspects unknown and not documented about the mechanical properties of bat wings. These properties vary between different bats and also for one individual bat where the variation is large for different locations in the wing. In this section the known properties of the membrane and bones will be described.

2.5.1 Wing membrane properties

The wing membrane of a bat consists of two layers of skin, with fibers and muscles in between. The structure of the fibers and muscles results in a largely anisotropic and adjustable mechanical behavior of the wing membrane. The stiffest direction of the wing membrane is in the same direction as the bones, resulting in a very flexible membrane perpendicular to that. Another property that makes bat wing skin a very special material is the fact that it is flexible for low strain but becomes much stiffer for higher strains (as can be seen in figure 2.8). The measurements done by Swartz et al. (1996) give an average value of the Young's modulus, failure strain and strength of the wing membrane gathered from different size bats. These values are given in table 2.1 in the direction of most fibers (0 degree) and perpendicular to that (90 degree) together with the r^2 values of the corresponding fit, which give information about the variability withing the measurements. From these values the anisotropic behavior is clearly visible, but also the uncertainty of these values is large (low r^2 values). The thickness of the measured membranes ranged from 0.078mm to 0.53mm with an average of 0.22mm for small bats (less than 10g) and 0.28mm for larger bats (50g) which is 4 to 10 times thinner compared to other mammals.

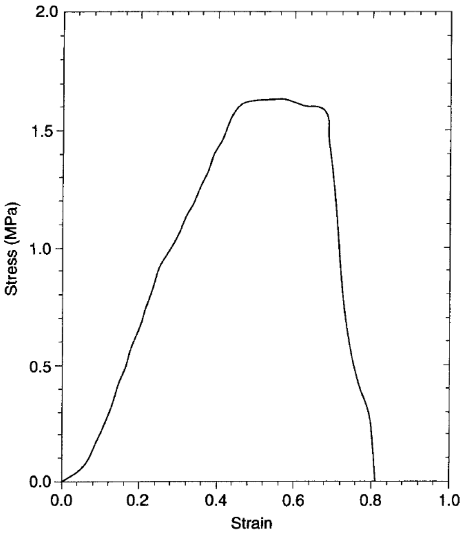

Figure 2.8 – Stress-strain curve of a representative piece of bat wing skin. (Swartz et al., 1996)

		0 degree	90 degrees	r^2
Youngs modulus	[MPa]	37	3.1	0.51
Failure strain	[-]	0.32	1.7	0.54
Strength	[MPa]	9.1	3.2	0.31

Table 2.1 – Mechanical properties of the wing membrane in the direction of most fibers (0 degree) and perpendicular to that (90 degrees).(Swartz et al., 1996)

2.5.2 Bone properties

Bat wings consists out of the same types of bones as a human arm, although the dimensions and mechanical properties are different. The fingers are much longer and Ulna and the first finger is much smaller. The names of all the bones can be found in figure 2.9, where you can see the arm (Humerus and Radius) and the fingers (I t/m V) that consist of the metacarpels and three phalanges. The leading edge of the wing is formed by the second and third finger, where the fifth finger is normally the most aft part of the wing.

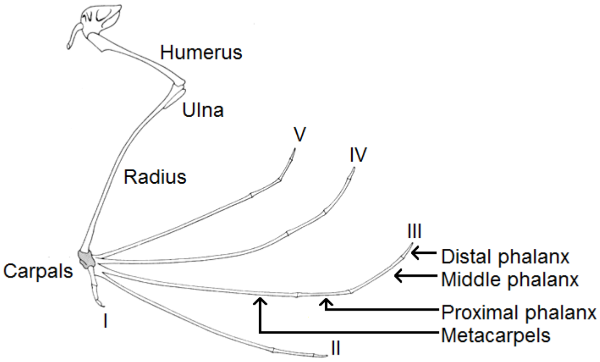

Figure 2.9 – Anatomy of a bat's wing

In general bats have thin, long flexible bones with a high density. The mechanical characteristics of the bones can be expressed in Young's modulus (E), tensile strength (TS), density (ρ) and area moment of inertia (I_2) which for a circular cross section is equal to:

$$I_2 = \frac{\pi}{64} d^4 \tag{2.1}$$

The Youngs modulus has been calculated from bending experiments with bones from a *Glossophaga soricina* bat and range between 20 GPa and 23 GPa (Swartz and Middleton, 2008). No reliable values for tensile strength are found. The density of bones from bats is found to be around 2000 $^{kg}/_{m^3}$ (Dumont, 2010) and the mid-bone diameters of the most important bones can be found in table 2.2.

	Diameter [mm]		Diameter [mm]
Humerus DV	1.5	Metacarpels V DV	0.81
Humerus ML	1.6	Metacarpels V ML	0.59
Radius DV	1.3	Proximal phalanx III ML	0.48
Radius ML	1.4	Proximal phalanx V ML	0.43
Metacarpels III DV	0.54	Distal phalanx III ML	0.28
Metacarpels III ML	0.43	Distal phalanx V ML	0.27

Table 2.2 – Diameter of most important bones of a bat of 22 grams. DV = dorsventral and ML = mediolateral. (Swartz and Middleton, 2008)

CHAPTER 3

Modeling of bat flight

With the use of the literature described in section 2 a mechanical model is designed for a bat inspired robotic wing. In this chapter the total kinematics will be divided into 7 sub-motions to enable mechanical modeling of the kinematics, next the aerodynamic requirements will be selected followed by the mechanical requirements. The last section will describe the mathematical model of four motions written in Matlab (7.11.0.584, R2010b). This model and the requirements are the starting point for the concept design in section 4.

3.1 The seven separate motions of bat flight

For the RoBat wing the kinematics of bats are divided into motions with one single rotational (for rotary actuators), translational (for linear actuators) axis or curvature change (for piezo-electric actuators). From the literature and the kinematic data used in the PhD thesis (Busse von, 2011) seven motions (figure 3.1) can be selected to form the total kinematics. The body and wing fixed reference systems as described in the introduction are used to define these seven motions:

1. Leading edge flap (LEF) rotation: rotation of the first and second digit around the y-axis of the wing-fixed reference system .
2. Active camber: change in camber.
3. Flapping motion: rotation around the x -axis of the body fixed reference systems.
4. Pitching motion: rotation of the wing around the y-axis of the wing fixed reference system.
5. Rear leg motion: rotation in the direction of the y-axis of the body fixed reference system, but around the ankle of the bat.
6. Yawing motion: rotation around the z-axis of the body fixed reference systems.
7. Wing contraction motion: translation in the direction of the y-axis of the wing fixed reference system.

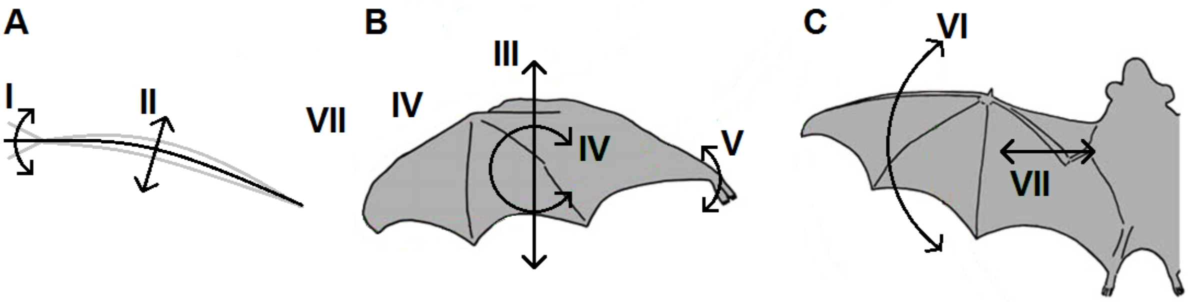

Figure 3.1 – Definitions of the 7 used motions in (a) the cross section of the wing, (b) the side-view and (c) the top view. I: LEF rotation, II: active camber, III: flapping, IV: pitching motion, V: rear leg motion, VI: yawing, VII: contraction.

3.2 Aerodynamic requirements and their relation with the motions

The aerodynamic requirements are derived from steady aerodynamic theory, using the definitions according to figure 3.2. Firstly the total aerodynamic force (F) are decomposed into a horizontal (equation 3.1) and vertical (equation 3.2) component, which are important forces concerning the performance. The vertical component will have to counteract the weight of the bat and the horizontal component will be used to overcome the body drag. Secondly the total aerodynamic force is also divided into a lift and drag force, relatively perpendicular and parallel to the effective inflow velocity (observed from a wing fixed reference system). These lift and drag forces can be constructed according to equation 3.3 and 3.4.

$$F_{hor} = F \cdot sin\left(\alpha_{flap}\right) \tag{3.1}$$

$$F_{ver} = F \cdot cos\left(\alpha_{flap}\right) \tag{3.2}$$

$$L = \frac{1}{2} c_{L\alpha} \alpha_{eff} \rho S U_{\infty,eff}^{2} \tag{3.3}$$

$$D = \frac{1}{2} c_{D} \rho S U_{\infty,eff}^{2} \tag{3.4}$$

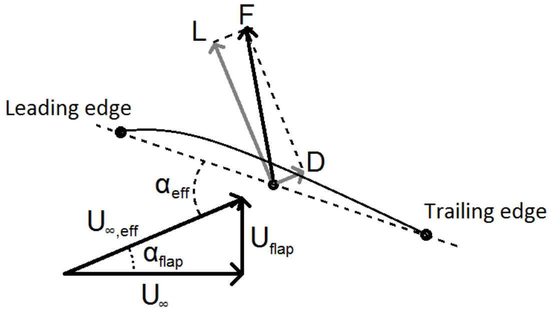

Figure 3.2 – Definition of aerodynamic forces

This set of equations gives us all the aerodynamic parameters that have to be comparable with bat flight. The three dimensional lift slope ($c_{L\alpha}$) is determined by the geometry of the wing and can be decomposed into two-dimensional geometry (camber and thickness) and three-dimensional geometry (aspect ratio), which the RoBat wing model needs to reproduce in order to simulate bat flight. The density ρ is assumed to be comparable with bat flight, because the same fluid is used (air). The surface area depends on the geometry and the velocity depends on the kinematics. This gives us the following set of parameters that have to be comparable with bat flight:

- Inflow angle (α_{flap})
- Camber
  - Leading edge flap deflection
  - Camber of the remaining chord
- Thickness
- Effective angle of attack (α_{eff})
- Aspect ratio (AR)
- Surface area (S)
- Velocity ($U_{\infty,eff}$)

The motions found in section 3.1 all have influence on these aerodynamic parameters, the effect of each motion is given in table 3.1. From this table it can be seen that the rear leg motion, active camber and LEF rotation are influenced by only a single parameter and therefore can be regarded as isolated motions. In contrast to that, the flapping, yawing, contraction and pitching motions have influence on several and overlapping aerodynamic parameters. To investigate this interaction, these motions are modeled in Matlab as described in section 3.4.

	Inflow angle	LEF angle	Camber	α_{eff}	Aspect ratio	Surf. area	Eff. velocity
Flapping motion	XX			XX			XX
Yawing motion	X			X			X
Contraction motion	X			X	XX	XX	X
Rear leg motion			X				
Pitching motion				XX			
Active Camber			XX				
LEF rotation		XX					

Table 3.1 – Connection between kinematic motions and aerodynamic parameters (X: minor influence, XX: major influence)

3.3 Mechanical requirements

In section 3.2 seven requirements were identified in the form of seven aerodynamic parameters that have to be comparable with bat flight. These requirements ensure comparable aerodynamic phenomena, but the corresponding parameters are influenced by the different motions mentioned in section 3.1 which are modeled using a Matlab program. This model doesn't incorporate deflection of the structure due to inertia and aerodynamic forces and therefore the mechanical properties have to be comparable with bats (see section 2.5) too. This gives us an extra set of requirements:

- Membrane
  - Youngs modulus: between 3 and 37 MPa (depending on direction)
  - Maximum strain: at least 1.7
  - Tensile Strength: At least 9 MPa
- Bones
  - Youngs modulus: ~22 GPa
  - Tensile Strength: High enough to withstand forces
  - Density: ~2000 $^{\text{kg}}/_{\text{m}^3}$
  - Diameter: see table 2.2

3.4 Mathematical model of bat flight

For prediction and optimization of the RoBat's motions, a Matlab routine is written that simulates the motion of the RoBat. This routing starts with an initiation where the stroke plane angle (β), frequency and geometry of the RoBat wing is defined. This geometry consist of three points, the wrist, wingtip and trailing edge of the fifth digit, initially defined in the neutral position, which will also be used to manufacture the wing. Then the wing geometry is multiplied by the rotational matrix:

$$R_{\gamma} = \begin{bmatrix} -sin\left(\beta\right) & 0 & -cos\left(\beta\right) \\ 0 & 1 & 0 \\ cos\left(\beta\right) & 0 & -sin\left(\beta\right) \end{bmatrix} \tag{3.5}$$

Resulting in a rotation of the wing around the y-axis with the stroke plane angle. This rotated geometry is now used in a loop to predict the motion of the RoBat for one wingbeat with small time increments (in this case $\frac{1}{25}$ of a wingbeat). For every time-step a rotational matrix is calculated with the use of equations 3.6, 3.7 and 3.8.

$$R\left(t\right)\left\{collum1\right\} = \begin{bmatrix} cos\left(m_2\left(t\right)\right) \cdot cos\left(-m_3\left(t\right)\right) \\ cos\left(-m_3\left(t\right)\right) \cdot cos\left(-m_1\left(t\right)\right) \cdot sin\left(m_2\left(t\right)\right) + sin\left(-m_1\left(t\right)\right) \cdot sin\left(-m_3\left(t\right)\right) \\ cos\left(-m_3\left(t\right)\right) \cdot sin\left(-m_1\left(t\right)\right) \cdot sin\left(m_2\left(t\right)\right) - cos\left(-m_1\left(t\right)\right) \cdot sin\left(-m_3\left(t\right)\right) \end{bmatrix} \tag{3.6}$$

$$R\left(t\right)\left\{collum2\right\} = \begin{bmatrix} -sin\left(m_2\left(t\right)\right) \\ cos\left(-m_1\left(t\right)\right) \cdot cos\left(m_2\left(t\right)\right) \\ sin\left(-m_1\left(t\right)\right) \cdot cos\left(m_2\left(t\right)\right) \end{bmatrix} \tag{3.7}$$

$$R\left(t\right)\left\{collum3\right\} = \begin{bmatrix} cos\left(m_2\left(t\right)\right) \cdot sin\left(-m_3\left(t\right)\right) \\ cos\left(-m_1\left(t\right)\right) \cdot sin\left(m_2\left(t\right)\right) \cdot sin\left(-m_3\left(t\right)\right) - cos\left(-m_3\left(t\right)\right) \cdot sin\left(-m_1\left(t\right)\right) \\ sin\left(-m_1\left(t\right)\right) \cdot sin\left(m_2\left(t\right)\right) \cdot sin\left(-m_3\left(t\right)\right) + cos\left(-m_3\left(t\right)\right) \cdot cos\left(-m_1\left(t\right)\right) \end{bmatrix} \tag{3.8}$$

In these equations, m_1 is the flapping motion, m_2 is the yawing motion and m_3 is the pitching motion, defined for one wingbeat. For each time-step, the coordinates of the wrist are multiplied with a factor representing the contraction motion. This is followed by a multiplication with the rotational matrix for all three points to obtain the predicted coordinates of the RoBat's wrist, wing tip and trailing edge of the fifth digit.

To accurately model the motions in Matlab, three dimensional kinematic measurements of real bats are used (Busse von, 2011) to determine the four motions. First this data is made periodic by rotating it around half the period, then a sine function was fitted to multiple periods realizing a fit with the required period. The flapping, yawing and contracting motions are derived from the kinematics of the wrist, because this point is least influenced by deflections. The pitching motion cannot be derived from the wrist alone, so for this motion, the fifth finger is used. The sine functions are defined by their amplitude, mean value, phase shift (negative is delayed) and period, where the period is equal for each motion. These values can be found in table 3.3.

	Amplitude	Mean value	phase shift
Flapping motion	32.4°	8.5°	90°
Yawing motion	19.9°	−123.6°	−3.5°
Contraction motion	0.0090m	0.052m	27.6°
Pitching motion	16.2°	−4.5°	−20.9°

Table 3.3 – Sinusoidal fit of the four modeled motions

The quality of this model can be seen in the figures 3.3, 3.4 and 3.5. In the first figure the kinematics of both the model and the measured data is shown in three different planes, from which can be concluded that the coordinates of the wrist are quite well modeled, but for the tip of the fifth digit and especially the wing tip, large discrepancies are present. This difference is probably because of the deflection (both active as passive) of the real bat wing that is not incorporated in the model. The errors might also be caused due to the fitting of the sine function because the real motions will most likely not be perfect sine functions and because of the total kinematics is simplified by four motions. The quality of the model can also be assessed on three parameters that are found to be important for the aerodynamics such as angle of attack, inflow velocity and inflow angle (section 3.2). This comparison can be found in figure 3.4 and 3.5 from which the conclusion can be made that the trends are comparable, but absolute values can differ between the model and the measurements. In section 5.2 these differences are minimized using an optimization.

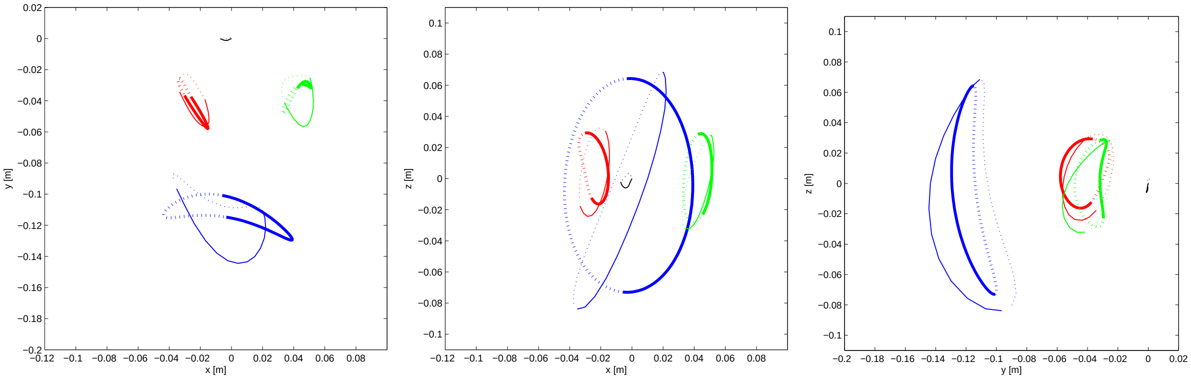

(a) Top-view **(b)** Side-view **(c)** Front-view

Figure 3.3 – Measured (thin line) and modeled (thick line) kinematics for the wingtip (blue), wrist (red), tip fifth digit (green) and body (black). Dotted lines are the upstroke and solid lines the downstroke.

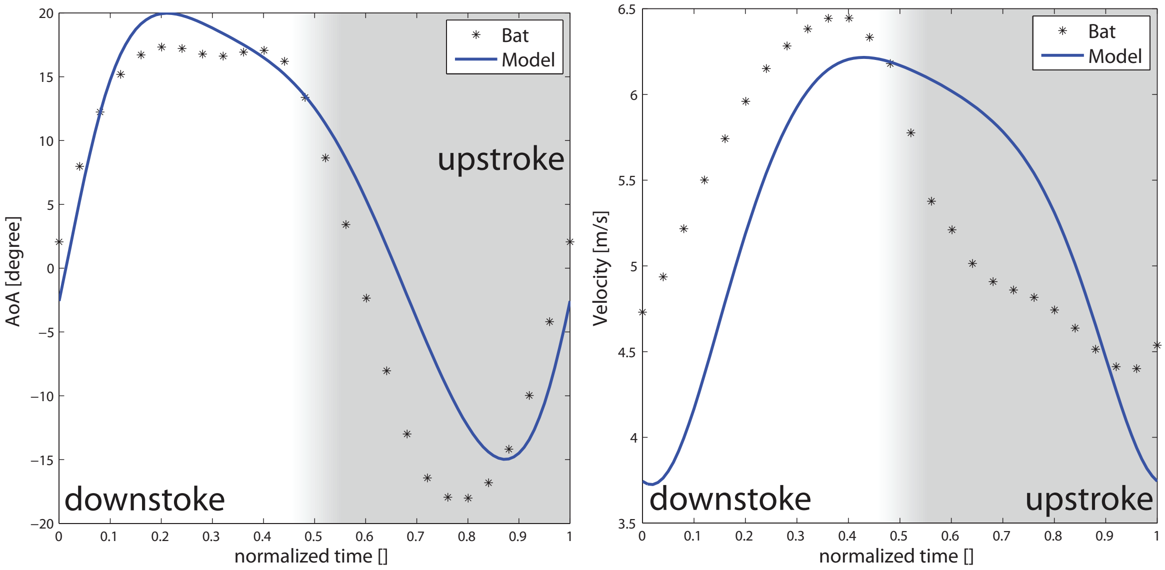

(a) (b)

Figure 3.4 – Comparison between bats and the model for the angle of attack (a) and effective velocity (b) at the midpoint of triangle "wingtip-wrist-fifth digit tip". The model consist of four different motions: flapping, pitching, yawing and contraction

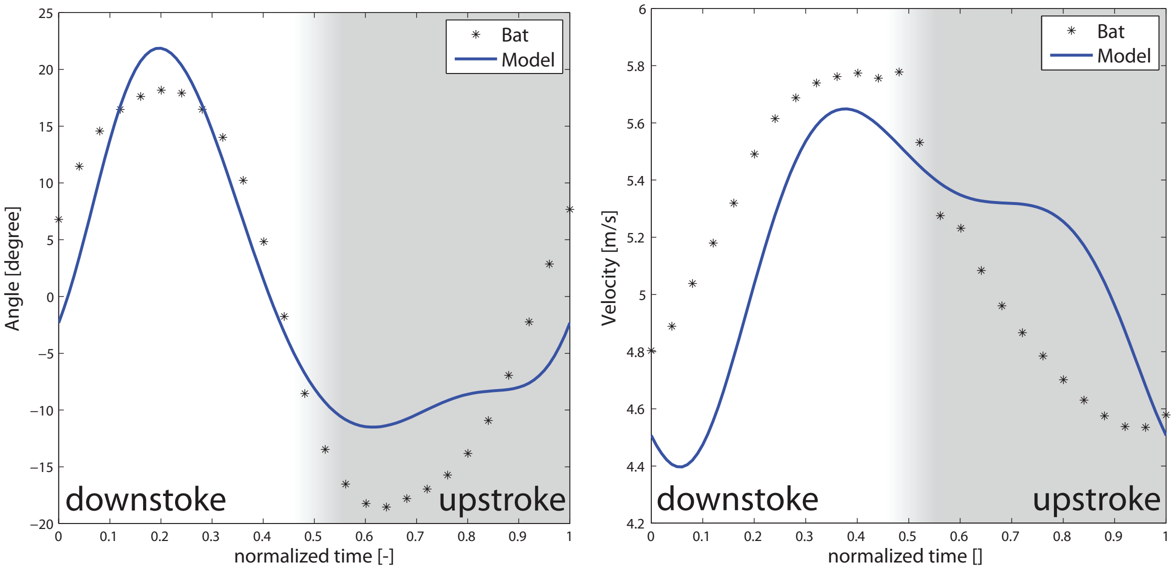

(a) (b)

Figure 3.5 – Comparison between the bats and the model for the angle (a) and magnitude (b) of the effective velocity at the wrist. The model consist of four different motions: flapping, pitching, yawing and contraction

CHAPTER 4

Conceptional design of the RoBat

4.1 Selection of degrees of freedom

From the kinematics in section 3.1 seven main motions are identified in section 3.1. Given the limitations of the present study, seven motions are too many to model because of structural complications, therefore the three most important motions are selected. Although the rear leg motion could be active and of influence for the aerodynamics, this motion is neglected because it is beyond the scope of this study. Secondly the importance of the LEF and camber motion are treated separately because these are isolated motions (as can be concluded from table 3.1). The four remaining motions (flapping, yawing, contracting and pitching) have influence on several and overlapping aerodynamic requirements (table 3.1) and thereby need to be analyzed together.

The leading edge flap motion

In aviation, the leading edge flap is used for two purposes, as high lift mechanism and for control of the aircraft. Both might also be the case for bat flight. Muijres et al. (2008) suggest that the actively changed shape of the wing (partly by the LEF angle) could contribute to the stability of the leading edge vortices and measurements done by Busse von (2011) suggest a correlation between the overall aerodynamics and the LEF angle. Much is still unknown about this and therefore this motion must be modeled in the RoBat to allow a further investigation of it's possible function. A sine function is fitted to the measured values (Busse von, 2011) which will be used for the RoBat model as variation of the LEF angle over the flapping cycle. Both the measured and modeled values are shown in figure 4.1a.

The camber motion

The camber of a bat's wing changes during the stroke, this is very likely to be active. At 5 m/s flight speed, the camber fluctuates between 7.1% and 8.2 % see figure 4.1b(Busse von, 2011). Using the thin airfoil theory for parabolic cambered airfoils (App, 2012), the two-dimensional lift coefficient can be calculated using equation 4.1.

$$c_l = 2\pi\left(\alpha_{eff} + 2h\right) \tag{4.1}$$

Where h is the camber and α_{eff} the effective angle of attack. For this case, the maximum difference between using the mean camber or the variable camber is equal to:

$$\Delta c_{l_{max}} = 4\pi\left(h_{max} - h_{mean}\right) = 4\pi\left(0.082 - 0.076\right) = 0.075 \tag{4.2}$$

The most valid concepts of implementing active camber make use of piezo-electric material or shape memory alloys, which are unproven for this application. Therefore and because of the increased complexity, the impact of active camber is decided to be too small to support the use of it in the RoBat model. Instead the mean value equal to 7.6% is used. For lower speeds, the active camber will be more important and might have to be incorporated in a model for lower speeds (Busse von, 2011).

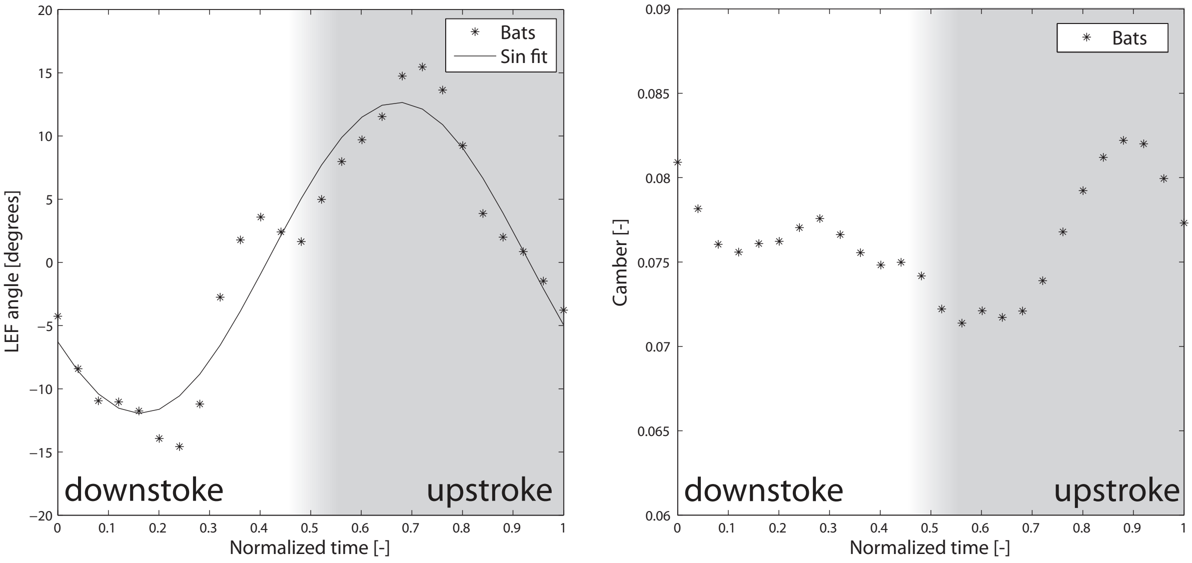

(a) (b)

Figure 4.1 – Deflection angles of the leading edge flap (a) and camber variation (b) during one period

Flapping, yawing, pitching and contracting motion

The four remaining motions are modeled in Matlab as described in section 3.4. Because of the use of the flapping motion, which is the main motion and the LEF angle motion, only one more motion can be used in this project. To be able to select this last motion, the 3 different combinations are modeled and their influence on the angle of attack, effective velocity and inflow angle are shown in figure 4.2 and 4.3. In these figures, the results of four different models are shown. The blue line is the result of the model with four motions (flapping, pitching, yawing and contraction). The green, red and yellow line are the result of models with two motions, respectively flapping/pitching, flapping/yawing and flapping/contraction. All results are compared with the data from bats represented with black asterisks.

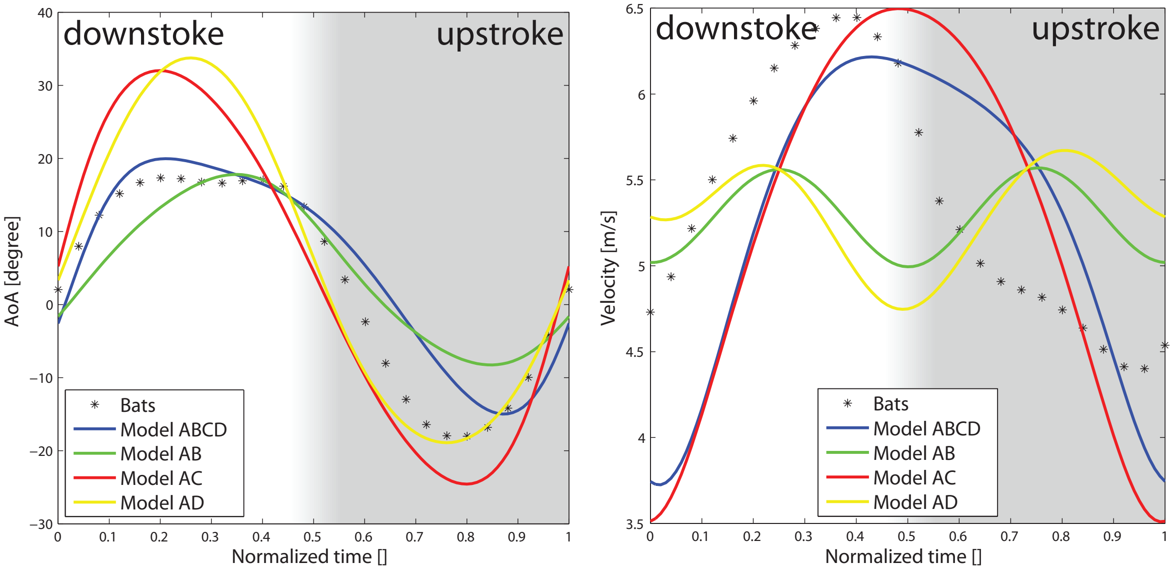

(a) (b)

Figure 4.2 – Angle of attack (a) and effective velocity (b) at the midpoint of the triangle, spanned by the wrist, wing tip and tip of the fifth digit, for four different combinations of flapping (A), pitching (B), yawing (C) and contraction (D)

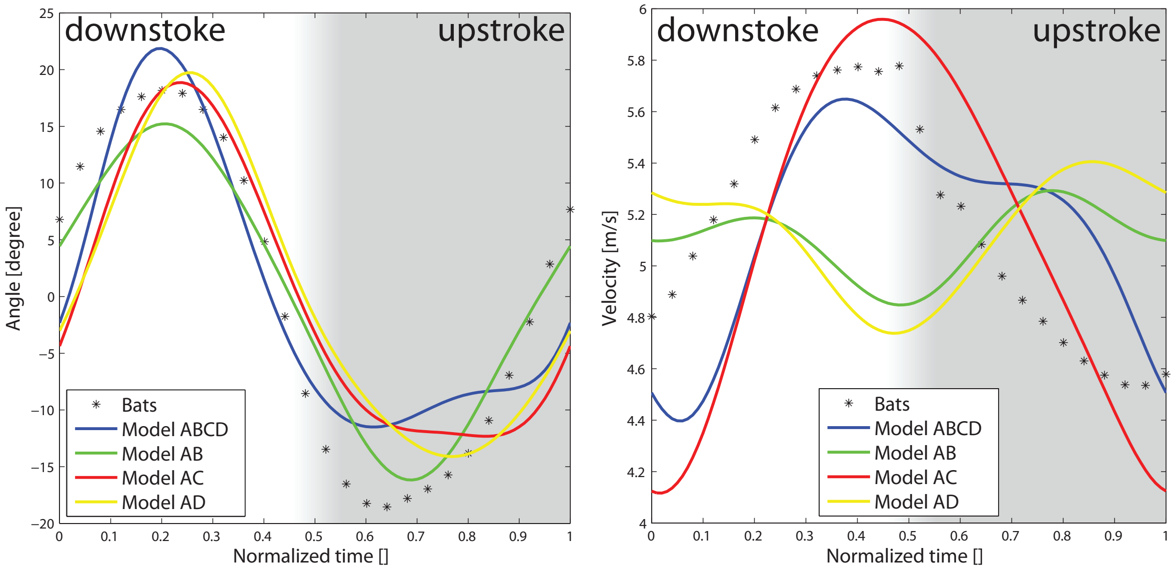

(a) **(b)**

Figure 4.3 – Angle (a) and magnitude (b) of effective velocity at the wrist for four different combinations of flapping (A), pitching (B), yawing (C) and contraction (D)

In figure 4.2a it is very clear what the influence of the pitching motion is. Both combinations without this pitching motion have a large overshoot in angle of attack during the downstroke. This overshoot will result in completely different aerodynamic phenomena such as large separated areas. The inflow angle in figure 4.3a shows small errors for all combinations, but doesn't give any preference. The magnitude of the effective velocity in figure 4.2b and 4.3b shows errors for the combinations with pitching (model AB) and contraction (model AD) motions. This will have influence on the magnitude of the lift production. The combination with yawing gives a slightly better result. The conclusion must be made that pitching is the most important motion, because the errors in angle of attack of the other options are unacceptable, the pitching motion also gives the opportunity to fine-tune the angle of attack. Besides that, the effective velocity can be improved by introducing a stroke plane angle as can be seen later.

4.2 Concept generation

The RoBat is installed on a sidewall of the windtunnel as can be seen in figure 4.4. The flapping axis is parallel to the free stream velocity and as close as possible to the windtunnel wall. The pitch and LEF angle motion axes should be the same or very close to each other and perpendicular to the windtunnel sidewall. The geometry of these axes will limit the way servos can transmit the motion to the wing because of limited space.

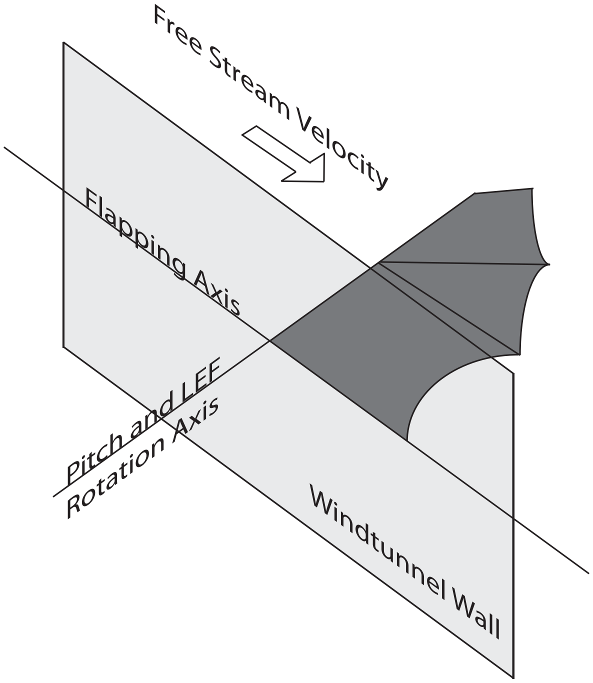

Figure 4.4 – Position sketch of the RoBat on a sidewall of the test section of the windtunnel.

Design concepts are generated for a mechanism that is capable of realizing the three selected motions (flapping pitching and LEF rotation). This is done for two separated parts, firstly the flapping motion followed by the remaining two motions. Pitching and LEF rotation cannot be treated separately because they are aligned with each other and thus have major influence on each other. For all motions, servos will be used that may transmit the motion in three different ways:

1. Direct connection: The servo axis is directly coupled to the part. This results in a rigid coupling, but has the disadvantages that the servo placement is restricted and no gear ratio is possible.
2. Geared connection: The motion is transferred using two cogwheels. This gives a little freedom in the placement of the servo, but requires precise alignment and extra parts.
3. Steering rod connection: The motion is transferred using one or more rods. This gives a lot of freedom in the placement of the servo but requires more parts.

Concepts for the first motion: flapping

The flapping motion is the main motion of this design and will be the first motion to be considered. The main problem with this motion is that the rotational axis is located on the boundary of the wind tunnel. As illustrated in figure A.1, due to limited space, this will lead to only one option, the rod connection (concept A1). To generate more design options, the option of shifting the rotational axis outside the windtunnel is also considered, giving two extra concepts (concept A2: direct connection and concept A3: geared connection). These three concepts are illustrated in figure B.1. It is important to note that this will have influence on the kinematics of the flapping motion.

Concepts for the second and third motion: pitching and LEF rotation

The pitching and LEF rotation motions are both rotations about the same axis and will be driven from outside the windtunnel. To be able to transfer these rotational motions, the first section of the wing must be straight, which will influence the geometry of the wing. The LEF rotation must be coupled to the pitching motion because pitching the wing must not change the relative LEF angle. This coupling can be achieved either mechanically or electrically. The first option implies a physical connection between the rotating part of the first servo and the housing of the second servo. The second one requires a fixed connection between the two servo housings and a coupling in the control of the servos. A second design decision is about the location of the two rotational axes. They can coincide with each other (inner and outer shaft) or be separated by a small distance (front/rear or top/bottom). For the second option, the two shafts need to be very close to each other which results in difficulties.

In figure A.2, the different design options are shown. The red hatched options are not possible because it is not possible to transfer a rotation from one axis to another axis without translation (concept B4, B5 and B6), or it is only possible with a hollow shaft servo (concept B7) or there is no place for a servo or gears (concept B10 and B11). The remaining six options (concept B1,B2,B3,B8,B9 and B12) are sketched in figure C.1 and will be discussed in the next section.

4.3 Concept selection

After the design options are generated, the best one is selected. This is done for both parts (motion 1 and motion 2/3) separately using the criteria:

- Motion 1: Flapping
  - Mechanical complexity
  - Mechanical rigidity
  - Rotational axis on the wind tunnel boundary
- Motion 2/3: Pitching and LEF rotation
  - Inertia moment around the flapping axis
  - Mechanical complexity
  - Mechanical rigidity
  - Flexible gear ratio to be able to adjust ratio between moment and angular velocity
  - Rotating servo (can introduce vibrations)

With these requirements, a trade-off is made using table 4.1 and 4.2. The best option resulting from this trade-off is concept 2 (direct connection) for the flapping motion and concept 8 (electrically coupled, same axis, geared connection) for the other two motions.

	Mechanical Complexity	Mechanical rigidity	Rot. axis on the boundary	Total score
Concept A1	–	–	++	-
Concept A2	++	+	o	+
Concept A3	o	+	o	o

Table 4.1 – Selection of the first motion, flapping. Sketches of these three concepts can be found in figure B.1. Grading from very bad (–) to very good (++).

	Inertia moment	Mechanical complexity	Mechanical rigidity	Flexible ratio	Rotating servo	Total score
Concept B1	-	+	++	-	-	o
Concept B2	-	-	o	+	–	-
Concept B3	-	–	-	+	–	–
Concept B8	+	+	+	+	+	+
Concept B9	+	o	-	+	+	o
Concept B12	+	o	-	+	+	o

Table 4.2 – Selection of the second and third motions, pitching and LEF rotation. Sketches of these six concepts can be found in figure C.1. Grading from very bad (–) to very good (++).

4.4 Scaling of the mechanical model

An important parameter that can be derived from the aerodynamic requirements is the frequency of the flapping motion , which in this case is around 10 Hz (Busse von, 2011). When using a sinusoidal flapping motion according to equation 4.3, the needed angular velocity according to equation 4.5 is equal to $1.9 \cdot 10^3 \mathrm{deg/s}$ (or 0.032 $\mathrm{s/60deg}$), which is about twice as fast as the fastest RC servo available.

$$\theta = A \cdot sin\left(\frac{2\pi}{p}t\right) \tag{4.3}$$

$$\dot{\theta} = \frac{d\theta}{dt} = \frac{2\pi}{p}A \cdot cos\left(\frac{2\pi}{p}t\right) \tag{4.4}$$

$$\dot{\theta}_{max} = \frac{2\pi}{p}A = 2\pi f A = 2\pi \cdot 10 \cdot 30 = 1.9 \cdot 10^3 \mathrm{deg/s} \tag{4.5}$$

To be able to still use RC servos the model will be scaled up in size, which will reduce the desired flapping frequency, as explained below. Other advantages of scaling are

- Reduction of unwanted vibrations
- Increase of the time resolution because of the lower flapping frequency.
- Increased dimensions will make the production of the wing easier.

Scaling the model will have influence on the free stream velocity, flapping frequency and mechanical properties if all relevant similarity parameters are to be maintained and will also effect the required power and moment. These scaling laws for a flapping wing will be derived in the next section, followed by the selection of the scale.

Scaling laws

When scaling the model, both aerodynamic and mechanical properties need to be scaled appropriate. For the aerodynamic part, the scaling laws from the lecture notes of Experimental Aerodynamics (Scarano, 2007) are used, keeping the Reynolds, and Strouhal number constant. For the mechanical part, the ratio between aerodynamic, inertia and elastic forces need to be constant to maintain comparable deformations.

Aerodynamics

Let us first focus on the aerodynamic part. Here the Reynolds number describes the ratio between inertia and viscous forces, at low Reynolds numbers, the viscous forces dominate the flow. The Strouhal number represents the unsteadiness in the flow, steady flow has a Strouhal number equal to zero. Scaling the model implies scaling a representative length l. Keeping the Reynolds number constant, results in a decreasing effective velocity with an increasing length (equation 4.6).

$$Re = \frac{U_{\infty,eff} \cdot l}{\nu} \Rightarrow U_{\infty,eff} \propto l^{-1} \tag{4.6}$$

Where ν is the kinematic viscosity. And $U_{\infty,eff}$ the effective velocity on the wing. The Strouhal number can be used to find the scale of f according to equation 4.7.

$$St = \frac{fl}{U_{\infty,eff}} \Rightarrow f \propto \frac{U_{\infty,eff}}{l} \propto l^{-2} \tag{4.7}$$

The effective velocity can be decomposed into U_{∞}, $U_{flap,x}$ and $U_{flap,z}$ according to equation 4.8 (using the definitions from figure 3.2), so all these velocities should also scale with the inverse of l.

$$U_{\infty,eff} = \sqrt{\left(U_{\infty} + U_{flap,x}\right)^2 + U_{flap,z}^2} \tag{4.8}$$

With the constant Reynolds and Strouhal number it can be shown that the lift force remains constant (equation 4.9) and the aerodynamic moment scales according to equation 4.10.

$$L = \frac{1}{2} c_L \rho S U_{\infty,eff} \propto l^2 \left(l^{-1}\right)^2 = constant \tag{4.9}$$

$$M_{aero} \propto L \cdot l \propto l \tag{4.10}$$

Forces Now we know that the lift force is constant, the other two forces, inertia and elastic forces also need to be constant. Assuming both lift and inertia forces act on the tip of the wing, neglecting the mass and stiffness of the membrane, the inertia force can be expressed as equation 4.11 using the geometry as in figure 4.5a. The elastic force is assumed to be proportional to the deflection angle which is expressed as equation 4.12 using the geometry as in figure 4.5b.

$$F_{inertia} = m \cdot a = m \cdot \ddot{\theta} l \propto \rho d^2 l \ddot{\theta} l = constant \tag{4.11}$$

$$F_{elastic} \propto \theta_{el} = \frac{Fl^2}{2EI_2} = constant \tag{4.12}$$

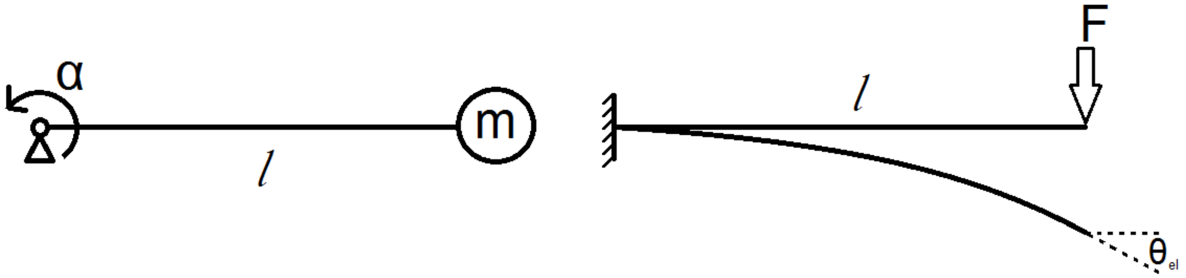

(a) Rotating point mass m, on a length l. **(b)** Clamped beam with force F, on length l.

Figure 4.5

Where m is the mass of the wing, $\ddot{\theta}$ is the angular acceleration, ρ the density of the bones, d the diameter of the bones, θ_{el} is the elastic deformation angle, F is the total force acting on the wing (inertia and aerodynamic), E is the Young's modulus and I_2 is the area moment of inertia. Lets first focus on the inertia force. For this inertia forces, the rotational velocities and accelerations need to be known.

Motions To find the influence of scaling on the angular velocity and acceleration, the flapping angle is modeled by a sine function with amplitude A and flapping frequency f:

$$\theta = A \cdot sin\left(2\pi f t\right) \tag{4.13}$$

The amplitude (A) will not be affected by scaling and f will scale according to equation 4.7. This results in an unaffected θ_{max} by scaling. Taking the derivative of θ results in the angular velocity ($\dot{\theta}$) :

$$\dot{\theta} = \frac{d\theta}{dt} = 2\pi f \cdot A \cdot cos\left(2\pi f \cdot t\right) \tag{4.14}$$

and the maximum $\dot{\theta}$ is influenced by f and thus scales according to equation 4.15.

$$\dot{\theta}_{max} = 2\pi f A \propto \frac{1}{l^2} \tag{4.15}$$

Similarly the angular acceleration ($\ddot{\theta}$) scales according to equation 4.16.

$$\ddot{\theta}_{max} = \left(2\pi f\right)^2 A \propto \frac{1}{l^4} \tag{4.16}$$

Bone density and stiffness Using equation 4.11 and 4.16, the inertial scaling can be found for the combination ρd^2:

$$\rho d^2 \propto \frac{1}{l\ddot{\theta}l} \propto \frac{1}{ll^{-4}l} = l^2 \tag{4.17}$$

Using equation 4.12 and 4.9 with the assumptions that I_2 can be scaled with d^4 and the lift force equals the total force F results in:

$$\frac{l^2}{Ed^4} = constant \tag{4.18}$$

$$Ed^4 \propto l^2 \tag{4.19}$$

Both the scaling of ρd^2 and Ed^4 can now be used to select a material and the dimensions for the RoBat wing. Equation 4.17 and 4.19 can only be fulfilled together when the density, Young's modulus or both are changed. In practice both are hard to change because these are material properties, so a trade-off has to be made between ρ, E, and d.

Moment and power scaling To calculate the effect of scaling on the needed moment and power, both aerodynamic and inertia forces need to be taken into account, which are both constant. This results in a scaling of the needed moment according to equation 4.20.

$$M = \left(F_{earo} + F_{inertia}\right) \cdot l \propto l \tag{4.20}$$

This moment can now be used to calculate the scaling of the needed power:

$$P = \dot{\theta}M \propto l^{-2}l = l^{-1} \tag{4.21}$$

Membrane stiffness To be able to calculate the influence of the scaling on the properties of the membrane, it is assumed that the membrane is stretched due to the pressure difference which is equal over the total wing. This results in a constant elongation which can be compared to a force F distributed over two sides of the membrane. The definition of the Youngs modulus can be found in equation 4.22 followed by the tension in this case (equation 4.23). Assuming that F is constant gives the scaling of Et in equation 4.24 and 4.25 which can be used in the design of the wing membrane.

$$E = \frac{\sigma}{\varepsilon} \tag{4.22}$$

$$\sigma = \frac{F}{A} = \frac{F}{l \cdot t} \tag{4.23}$$

$$E = \frac{F}{\varepsilon l t} \propto \frac{1}{lt} \tag{4.24}$$

$$Et \propto \frac{1}{l} \tag{4.25}$$

Scale selection

Using the scaling laws from the previous section, the optimum scale of the model within the restrictions of the servos can be selected. The two requirements for this selection are the flapping moment and the angular velocity. The required angular velocity which is given by equation 4.26 is shown in figure 4.6a.

$$\dot{\theta}_{max} = \frac{2\pi}{p_0} A_0 \cdot \frac{1}{scale^2} \tag{4.26}$$

Where p_0 and A_0 are the original period and amplitude.

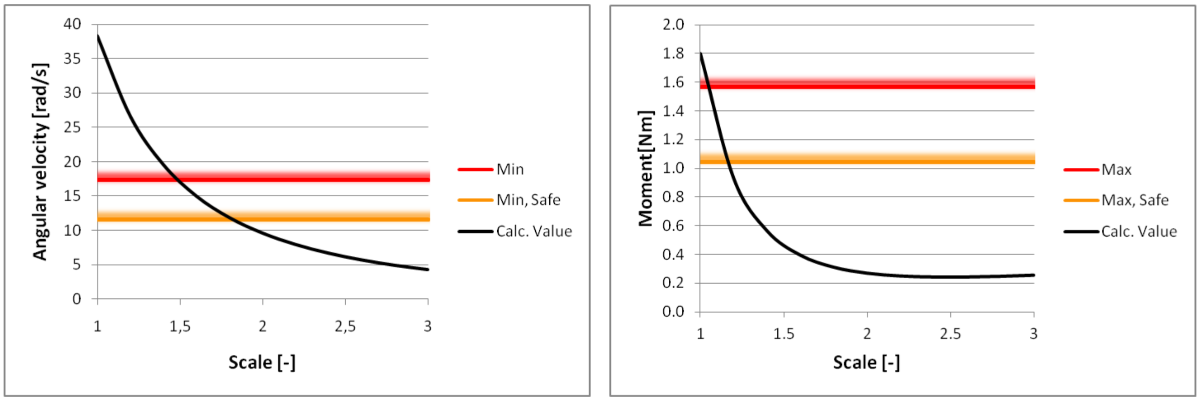

(a) (b)

Figure 4.6 – Effect of scaling on the required angular velocity (a) and flapping moment (b), with the boundaries derived from the servo characteristics and a safety factor equal to 1.5.

The flapping moment consists of an aerodynamic part and an inertia part. The aerodynamic part was estimated using equation 4.27

$$M_{aero} = F_{earo} \cdot l = L \cdot b = \frac{W_{bat}}{2} b = \frac{m_{bat} \cdot g}{2} b \tag{4.27}$$

The inertia moment can be calculated using equation 4.28

$$M_{inertia} = I_{tot} \cdot \ddot{\theta}_{max} \tag{4.28}$$

Where the angular velocity is calculated using equation 4.29 and the moment of inertia consists out of a wing, servo and construction part. The construction part is gathered from a 3D digital design with the appropriate densities. The servo inertia is calculated using equation 4.30, where Δy is the offset from the mass center of the servo to the rotational axis of the flapping motion.

$$\ddot{\theta}_{max} = \left(\frac{2\pi}{p}\right)^2 A \tag{4.29}$$

$$I_{servo} = m_{servo} \cdot \Delta y^2 \tag{4.30}$$

The inertia moment of the wing can be constructed using the inertia moment of the membrane and the bones, calculated using the equations:

$$I_{membrane} = \frac{mb^2}{3} = \frac{\frac{S}{Yield} \cdot b^2}{3} \tag{4.31}$$

$$I_{bones} = \frac{mb^2}{3} = \frac{\rho \pi d^2 b b^2}{3} \tag{4.32}$$

Using the appropriate values, the calculated flapping moment is shown in figure 4.6b. When scaling up, the required moment first decreases because of the reduced angular acceleration. When using a scale of 2 and higher, the inertia moment of the wing becomes more important, with the consequence that the required moment increases. Combining the trend of the required moment and angular velocity, results in an optimal scale equal to 2. As a consequence U_∞ is twice as small for the RoBat model compared to bat flight. For comparison purpose, the equivalent freestream velocity (U_{eq}) will often be quoted which is twice the measured U_∞ and thus corresponds to the free stream velocity of the equivalent bat flight.

CHAPTER 5

Detailed design of the RoBat

5.1 Wing design

The wing consists out of three parts: the bones, the membrane and its geometry, which all have to be comparable with real bats. In this section, the detailed design will be described starting with the geometry.

Geometry

For the conceptual design, the mean values of the kinematic data are used to construct the geometry of the mathematical model wing. Because of the contraction of the arm, there is a difference between the up and downstroke geometry which isn't incorporated in the RoBat. When using the mean kinematic geometry both the up- and the downstroke will be erroneous. An alternative, that is used in this case, is the use of the mean downstroke geometry. In this case the errors for the downstroke will be decreased while the errors for the upstroke will be increased. This is considered to be an improvement compared to the mean of the total stroke, because the downstroke is more important for the lift production and thereby the main focus of this project. This mean downstroke geometry is shown in figure 5.1 as three dotted straight red lines, with a node at the wrist. For the RoBat, the wrist has to be aligned with the y-axis to be able to transfer the LEF-motion. Taking that and a constant span and wing area into account, this simplification combined with the addition of the fourth finger and LEF results in the geometry showed by solid lines in figure 5.1. This simplification will have influence on the kinematics, but the optimization carried out in section 5.2 will improve this.

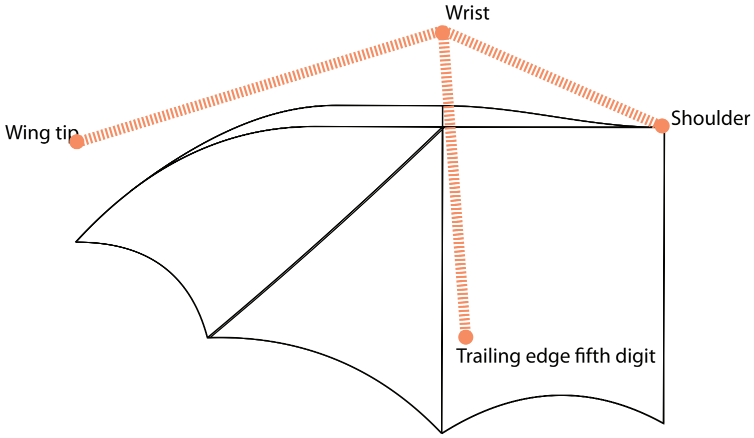

Figure 5.1 – Wing geometry of the RoBat (solid line) compared to the mean downstroke geometry of a bat wing (red dashed lines connecting the shoulder, wrist, end of fifth digit and wing tip)

Bones

With the mechanical bone properties from section 3.3 and the scaling laws in section 4.4 the dimensions of the model can be determined. A trade-off has to be made between scaling according to the inertia forces $\left(\rho d^2 \propto l^2\right)$ and elastic forces $\left(Ed^4 \propto l^2\right)$ because the choice of density and stiffness is limited by material choice. In this case only carbon tubes are found to be reasonable candidates because of the high quality requirements and the demand of several different sizes. This restricts the degrees of freedom to one, the diameter. In table 5.1 the characteristics of a 3 and 2 mm carbon bone can be found compared with the arm of the bat wing (average of the Humerus and Radius). The 3 mm carbon bone scales very well for the inertia forces (ρd^2 =0.014 instead of 0.016) but not so well for elastic forces (Ed^4 =11 instead of 0.35). The 2 mm carbon bone gives a better scaling for the elastic forces (Ed^4 =2.2 instead of 0.35) at an expense of the inertia forces (ρd^2 =0.0064 instead of 0.016). Keeping in mind that there are a lot of uncertainties for the stiffness of bat bones and the fact that the muscles in a bat wing will probably add stiffness to the total structure, the 3 mm carbon bone is used for the RoBat. The diameter of the fingers are dimensioned accordingly.

	Bat bone	Carbon bone 1	Carbon bone 2	Desired RoBat bone
diameter [mm]	1.4	3.0	2.0	
density $[\mathrm{kg}/\mathrm{m}^3]$	2000	1590*	1590*	
Young's Modulus [GPa]	23	140**	140**	
Ed^4 $\left[\mathrm{Nm}^2\right]$	0.088	11	2.2	0.35
ρd^2 $\left[\mathrm{kg} \cdot \mathrm{m}^{-1}\right]$	0.0048	0.014	0.0064	0.016

Table 5.1 – Comparison between bat bones, RoBat bones and desired RoBat bones.(*(Mat, 2012),**(dpp pultrusion, 2011))

The wing membrane

From section 2.5.1 it has become clear that a bat wing membrane is an anisotropic material with a Young's modulus that depends on the amount of strain. For low strains (<10% for the stiffest direction) the material is very elastic, but for larger strains, the Young's modulus increases. This in combination with the active muscles present in the wing membrane makes it impossible to find an off-the-shelf material that is comparable with the bat wing membrane. A simplification is necessary which results in an isotropic material that is not capable of actively change it's properties. Because the material used for the skin of the model will be isotropic, a choice had to be made between the stiff direction (aligned with the finger bones) and the elastic direction (perpendicular to the finger bones) of the bat wing membrane. For this model, the elastic direction is chosen because this direction is most important for the deflection of the membrane and thus the change in camber. Using the scaling law found in section 4.4 and the stiffness and thickness found in section 2.5.1, the resulting Et for the RoBat is equal to:

$$E_{model}t_{model} = \frac{E_{bat}t_{bat}}{scale} = \frac{3.1 \cdot 0.28}{2} = 0.43MPa \cdot mm \tag{5.1}$$

Natural rubber is found to have a good quality for very thin sheets and a completely elastic behavior for large strains. The Young's modulus is found to have an average value equal to 1.5 MPa over the first 50% strain and a decreasing Young's modulus with increasing strain (see measurements in figure 5.2). It is important to note that natural rubber has a hysteresis effect (only the loading measurements are taking into account in this case) as can be seen in figure 5.2 and that the decreasing Young's modulus with increasing strain is not comparable with the real bat wing membrane. With a 1.5 MPa Young's modulus, the desired thickness can be calculated according equation 5.2. The nearest available thickness that is used for the RoBat is equal to 0.25mm.

$$t_{model} = \frac{E_{model}t_{model}}{E_{model}} = \frac{0.43}{1.5} = 0.29mm \tag{5.2}$$

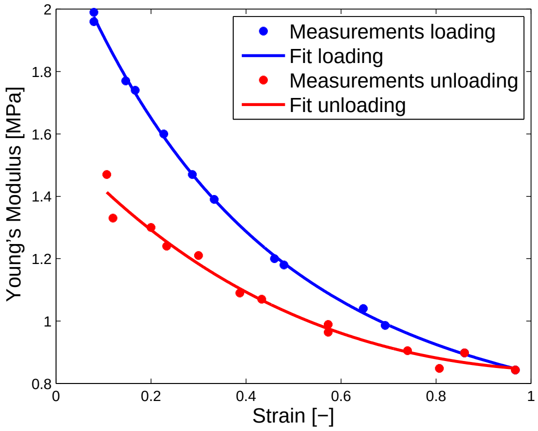

Figure 5.2 – Young's modulus of natural latex sheet, for different strains.

5.2 Optimization of the kinematics

In section 4.1 three motions were selected: flapping, pitching and LEF-rotation. This was done with a wing geometry based on the kinematics of the total period and without a stroke plane angle. The geometry of the RoBat is based on the downstroke kinematics, with some simplifications (see section 5.1) and a stroke plane angle of 17 degrees is introduced in the model. All these adjustments have influence on the kinematics of the RoBat which makes some adjustments in the flapping and pitching motion necessary in order to obtain the right aerodynamic parameters, such as the angle of attack (α_{eff}) and the inflow angle (α_{flap}). The new flapping and pitching motions are found by an optimization scheme which uses the pitching motion to optimize the α_{eff} according to equation 5.3 and the flapping motion to optimize the α_{flap} according to equation 5.4. For both cases the scheme is written such that motions remain periodic and the mean values are comparable with real bat flight.

$$\theta_{pitch_{new}}(t) = \theta_{pitch_{old}}(t) + k_{pitch} \cdot (\alpha_{eff_{model}}(t) - \alpha_{eff_{bat}}(t)) \tag{5.3}$$

$$\theta_{flap_{new}}(t) = \theta_{flap_{old}}(t) + k_{flap} \cdot \int_0^t (\alpha_{flap_{model}}(\tau) - \alpha_{flap_{bat}}(\tau))\, d\tau \tag{5.4}$$

Using values equal to 0.2 and 3 for respectively k_{flap} and k_{pitch}, the error in both angle of attack and inflow angle decreases to less than 1 degree after 17 iterations followed by an increasing error due to instabilities in the optimization scheme. The optimized flapping and pitching motions together with their original sine motions are shown in figure 5.3 to show the difference. For the motor control sine functions are most convenient, so the optimized motions are fitted with a combination of 3 sine functions. The resulting effective velocity, inflow angle and angle of attack of the sine fitted motion together with its original optimized motion are presented in figure 5.4. You can see that the sine fit introduces a small error, but remains acceptable.

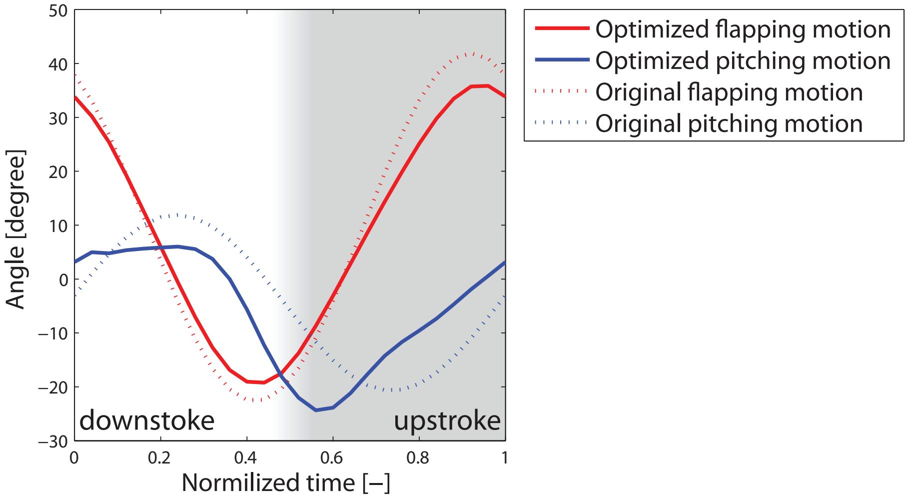

Figure 5.3 – Optimized flapping and pitching motions together with their original sine shaped motion.

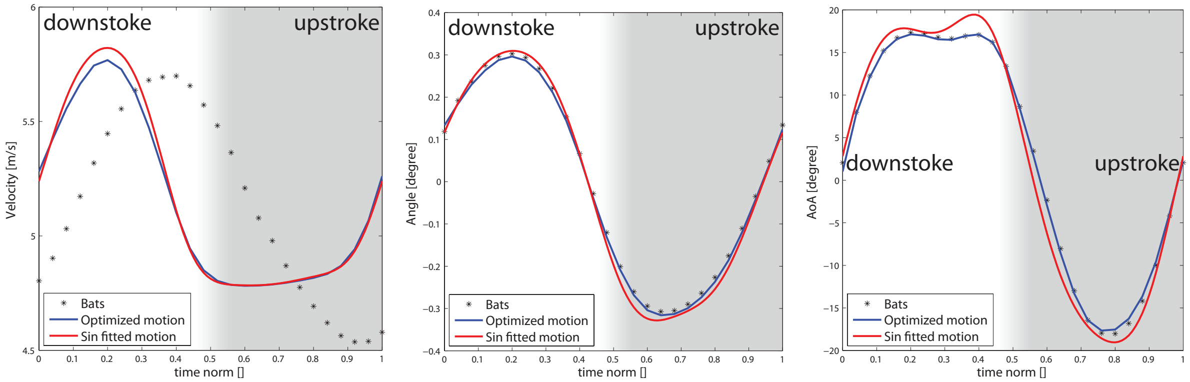

(a) Effective velocity **(b)** Inflow angle **(c)** Angle of attack

Figure 5.4 – Results of the optimized motions and the sine fit compared with the real measurements.

5.3 Drive design

In this section the concept chosen in section 4.3 will be designed in more detail. The main requirements will be:

- Low moment of inertia around the flapping axis
- Small offset of the flapping axis with respect to the wind tunnel wall
- Easy production with the use of off-the-shelf parts
- Structural stiffness and alignment to prevent unwanted vibrations and motions

Taking these requirements into account, the RoBat is designed according to figure 5.5 and 5.6. A bracket is milled from high strength aluminum as basis structure. The pitching axis of the wing is connected to this bracket by two bearings and the bracket is fixed to the "flapping motion" servo on one side and a bearing on the other side to ensure mechanical stiffness (figure 5.5). The whole part as shown in figure 5.6 is fixed to a rotating disc in the windtunnel wall to be able to adjust the stroke plane angle of the model.

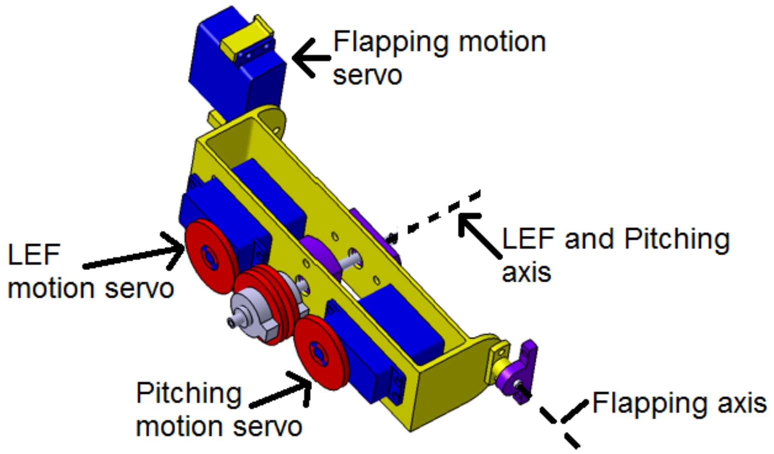

Figure 5.5 – Computer drawing of the drive system, with annotations of the servos and rotational axis. Red: gear, Blue: servo, Yellow: structure, Purple: bearing, Gray: axis.

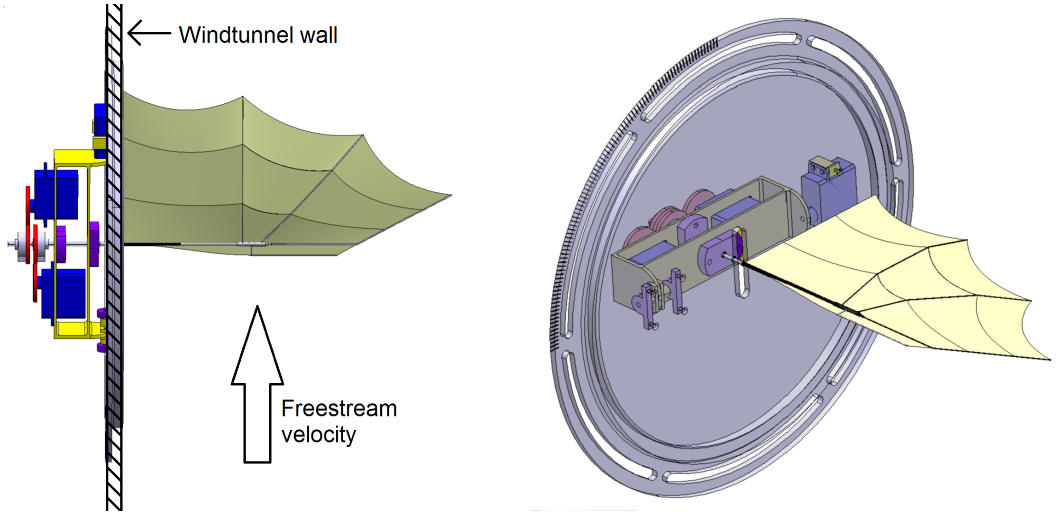

(a) Top view RoBat **(b)** 3D view RoBat

Figure 5.6 – Computer drawings of the total system. Red: gear, Blue: servo, Yellow: structure, Purple: bearing, Gray: axis.

5.4 Electronic design

The servos in this model have three wires to connect, two for the power and one for the signal. This signal must be a pulse, where the length of the pulse determines the angle of the servo (900ms for -60 degrees and 2400ms for +60 degrees). This pulse will be generated by an Arduino, an easy to program microchip. The Arduino will be powered by the USB connection to a computer which is used to update the Arduino software and to give commands during operation. The ground of the power source has to be connected to the ground of the Arduino. This results in the electrical scheme showed in figure 5.7.

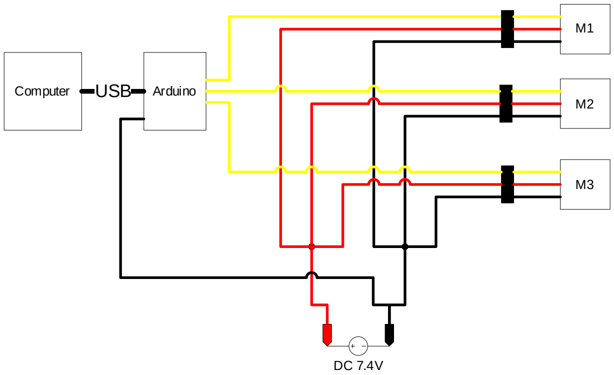

Figure 5.7 – Electrical scheme of the RoBat with the three servo motors (M1-M3) and power source (DC 7.4V) connected by the ground wire (black), the positive power wire (red) and the signal wire (yellow).

5.5 Software design

The software used to program the Arduino microcontroller is based on C++ and has three phases, the initialization and setup which will only be executed once and a loop which will be repeated continuously during the measurement. You will recognize those phases in figure 5.8. For this design, it is possible to stop and start the servos with commands from the computer. When started, the servos move from neutral to their start position from where the motion will be started. This is done to prevent large unwanted accelerations at the start of the motion. When the command stop is given, the servos continue their motion until the neutral position is reached, this again to have a smooth start-up for the next time.

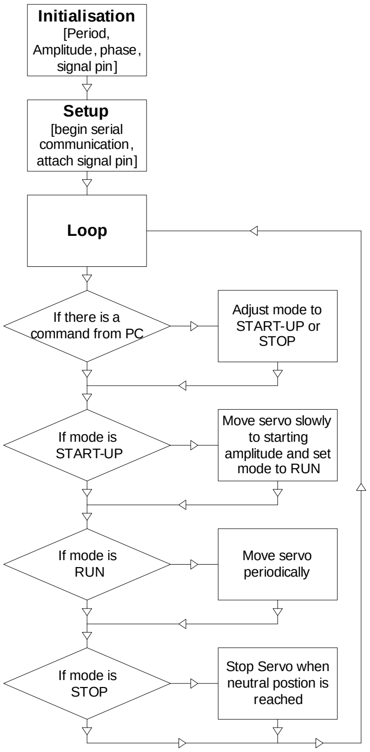

Figure 5.8 – Software design

CHAPTER 6

Test set-up

For this study measurements are done in the Lund University windtunnel. The wing kinematics are determined using two high speed cameras, while the aerodynamic analysis is performed with a PIV system with two cameras for the wake measurements and one camera for the onwing measurements. For the wake measurements, the second camera is used to increase the measurement domain.

6.1 Windtunnel

The Lund University windtunnel is a closed loop, low turbulence and low speed wind tunnel with a maximum velocity of 38m/s (Pennycuick et al., 1997). This wind tunnel is specially designed for animal flight. For this reason, there is an open section with a length of 0.5m after the test section to facilitate easy access for animal handling, as can be seen in figure 6.1. It is also possible to tilt the total wind tunnel to be able to test gliding flight. For this study the windtunnel is always used in the horizontal position.

The test section has an octagonal shape with a height of 1.08m, a width of 1.20 and length equal to 1.20m. The overall turbulence level in the test section is below 0.04% at 10m/s, but it is important to note that the boundary layers on the walls of the wind tunnel will have influence on the velocity up to 3 cm and on the turbulence up to 10 cm from the walls (Pennycuick et al., 1997). This is respectively 10% and 34% of the semi-span of the model.

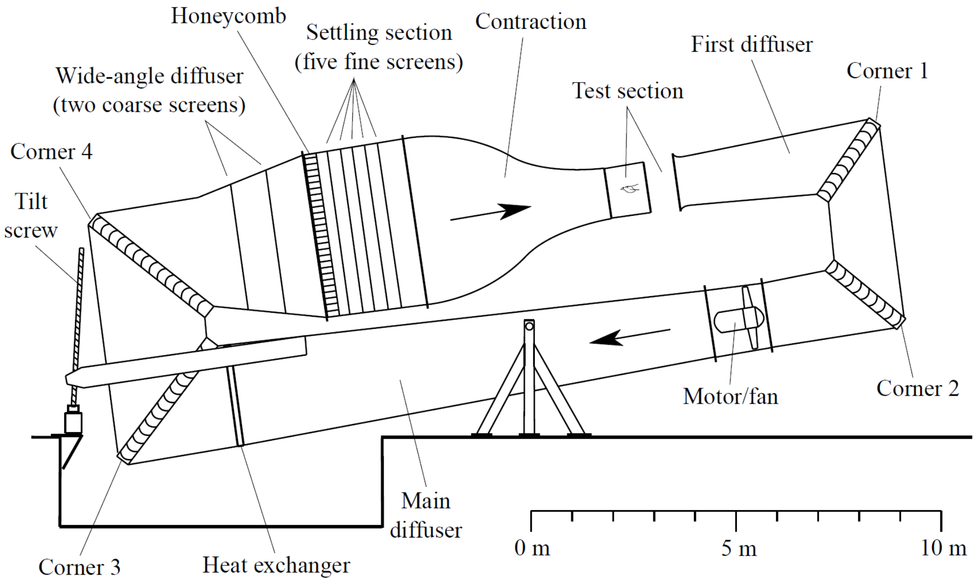

Figure 6.1 – Layout of the Lund University wind tunnel. The direction of air movement is shown by the arrows.(Pennycuick et al., 1997)

6.2 PIV system

The PIV system consisted of a 200 Hz 50 mJ Laser (Litron LPY732 series, Nd:YAG, 532mm) for illumination of fog particles (1 µm diameter), a CMOS-camera (High-SpeedStar3; 1024 x 1024 pixels) and a frame grabber PCI board in a host computer. From this computer, the total system is controlled using LaVision software from DaVis (LaVision, DaVis 7.2.2.110). This software package is also used to calibrate the two cameras using an inbuilt calibration routine and a calibration plate with fixed and known pitched markers.

With the PIV system producing 200 images per second, each flapping period of the RoBat (2.5Hz) results in 80 images. The PIV system is not synchronized with the flapping motion of the RoBat, but because of the high number of images per period and the repetitive motion of the RoBat, it is accurate enough to determine the starting image for each period manually and use this starting point for the period averaging of the PIV data.

6.3 Kinematics cameras

With two high speed camera's (Redlake MotionScope PCI 500, frame rate 250Hz, shutter speed 1/1250s) the flapping motion is recorded from two different angles. To minimize the interference with the PIV system, infrared light is used to illuminate the markers on the wing.

Using the recordings from both angles, 8 markers on the wing are digitized into three dimensional coordinates using direct linear transformation software (Hedrick, 2008). For this purpose, a calibration is performed for every test setup. This is done with a custom made calibration cube with markers having known coordinates. Alignment of the calibration cube with the flow and wind tunnel walls is assured with the use of a digital spirit level.

6.4 Test set-up

Two different test configurations are used, one for the wake measurements (figure 6.2a) and one for the onwing measurements (figure 6.2b). In both cases, one kinematic camera is placed upstream from the top and one downstream from the top, to be able to capture the 8 markers during the complete stroke. For the wake measurements the PIV cameras are placed downstream of the test section looking upstream (figure 6.2a). The two cameras are placed on top of each other, so that the two measurement areas are just overlapping resulting in a larger measurement area. The laser is positioned diagonally from above, using a mirror on the side of the windtunnel to obtain an illumination of the fog particles in the YZ plane measurement domain. For the onwing measurements, the laser sheet is aligned with the flow in the ZX-direction and the PIV camera was positioned outside the test section at the opposite side of the RoBat (figure 6.2b). The placement of the PIV camera is chosen to minimize shadows and reflections . The two locations of the light-sheet during the measurements were at 14.7 and 18.4 cm from the wind tunnel wall (respectively blue and red lines in figure 6.2b).

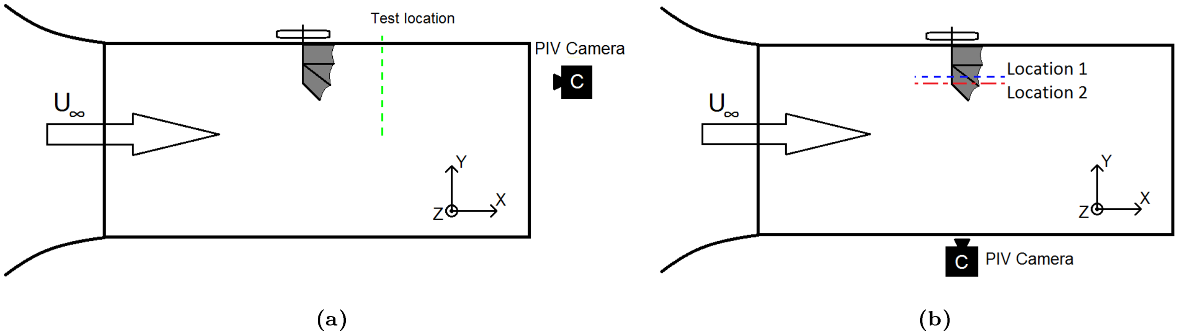

(a) (b)

Figure 6.2 – Test section of the windtunnel seen from above with the test set-up for the wake measurements (a) and the onwing measurements (b) with the corresponding windtunnel fixed reference system.

6.5 The measurement sequences

The measurements are divided into the wake measurements and onwing measurements. Both measurements are performed with different measurement configurations (changing stroke plane angle, free stream velocity and LEF motion). All measurement configurations are performed five times resulting in five independent measurement sequences of nine periods. These nine periods are used to determine the period average of each sequence, resulting in five period averaged periods for each configuration.

Wake measurements

With the wake measurements, the influence of the LEF is analyzed. This is done by comparing a measurement configuration where the LEF is performing a sine motion with a configuration where the angle LEF is fixed. Both measurement configurations consist of five independent measurement sequences which are used to calculated a mean value and its corresponding standard deviation. To be able to draw more general conclusions from these measurements, the measurement domain is expanded in the free stream velocity domain (U_{eq}=4.4, 5.0 and 5.6 m/s) and in the stroke plane angle domain ($\beta = 68°$, 73° and 78°). This results in the ten measurement configurations which are summarized in table 6.1.

Measurement set	LEF	Aimed U_{eq}	Stroke plane angle (β)
[-]	[-]	[m/s]	[degree]
1	motion	5	73
2	fixed	5	73
3	motion	4.4	73
4	fixed	4.4	73
5	motion	5.6	73
6	fixed	5.6	73
7	motion	5	78
8	fixed	5	78
9	motion	5	68
10	fixed	5	68

Table 6.1 – Overview of the ten measurement configurations used for the wake measurements.

Onwing measurements

In order to investigate the influence of α_{eff} and St on the performance of flapping bat wings, two sets of measurements are done, both with the wing kinematics described in section 5.2, based on *Leptonycteris yerbabuenae* at 5 m/s. Both sets of measurements are performed throughout an equivalent flight speed range from 1 m/s to 7 m/s, see table 6.2. In the first case the body angle and thereby the stroke plane angle and $\alpha_{eff,max}$ of the flapper is adjusted so that the maximum α_{eff} ($\alpha_{eff,max}$) is equal to that of *Leptonycteris yerbabuenae* throughout the flight speed range ($\alpha_{eff,max}$=55° at 1 m/s to $\alpha_{eff,max}$=15° at 7 m/s), hereafter called the variable α_{eff} case. In the second set of experiments the $\alpha_{eff,max}$ is kept constant throughout the flight speed range ($\alpha_{eff,max}$=55°, based on *Leptonycteris yerbabuenae* at 1 m/s), hereafter called the constant α_{eff} case. The stroke plane angles required to obtain the desired α_{eff} are calculated using simplified trigonometry. Note that changing the stroke plane angle to optimize α_{eff} will also result in a change in pitching angle relative to the wind tunnel frame of reference. In table 6.2 the resulting 9 configurations are shown, starting with the variable α_{eff} case followed by the constant α_{eff} case. The Reynolds number in table 6.2 is calculated using equation 4.6 and 4.8 based on the mean chord and mean flap velocity of the wing tip over the downstroke. The Strouhal number in table 6.2 is calculated using equation 4.7 and 4.8 based on the semi-span and the mean flap velocity of the wing tip over the downstroke.

Measurement set	U_{eq}	Required $\alpha_{eff,max}$	Stroke plane angle (β)	Re_{tip}	St_{tip}
[-]	[m/s]	[degree]	[degree]	[-]	[-]
Variable α_{eff} case	7	15	12	2.5E4	0.19
Variable α_{eff} case	5	20	17	1.9E4	0.25
Variable α_{eff} case	3	35	27	1.4E4	0.35
Variable α_{eff} case	2	45	42	1.2E4	0.42
Variable/Constant α_{eff} case	1	55	52	8.8E3	0.55
Constant α_{eff} case	2	55	65	1.2E4	0.39
Constant α_{eff} case	3	55	70	1.6E4	0.31
Constant α_{eff} case	5	55	73	2.2E4	0.22
Constant α_{eff} case	7	55	74	2.9E4	0.17

Table 6.2 – Overview of the ten measurement configurations used for the onwing measurements.

CHAPTER 7

Data analysis

7.1 Wake kinematic data

To generate data about the shape and location of the wing, the RoBat wing is captured using two high speed cameras. An example of the pictures that are recorded with one of those cameras can be found in appendix E. The eight markers on the wing in these pictures are automatically tracked and digitalized into three dimensional coordinates using direct linear transformation software (Hedrick, 2008). The first marker is on the shoulder, the second on the LEF, markers 3-6 are on the fifth digit and markers 7 and 8 are on the third digit with number 8 on the wing tip (see figure 7.1). With these markers, the LEF angle, camber, α_{eff}, inflow angle and inflow velocity are calculated.

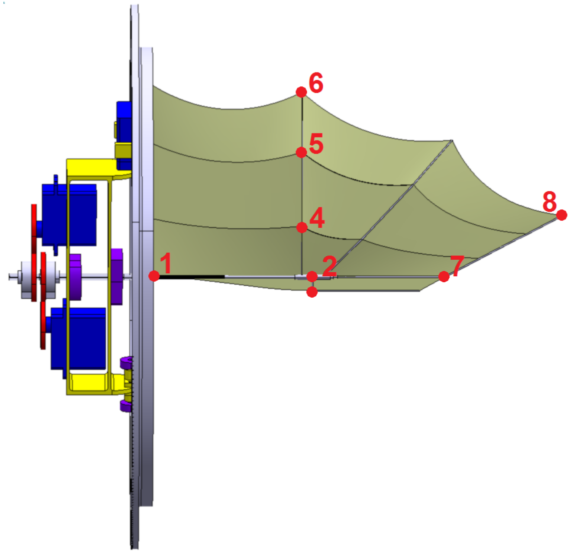

Figure 7.1 – Top view of the numbered markers on the RoBat wing

LEF angle The LEF angle is defined as the angle between the LEF triangle (spanned by the markers 2, 3 and 7) and the triangle next to it (spanned by the markers 4, 3 and 7). The surface normals of those triangles are calculated using

$$\mathbf{n_1} = [\mathbf{p3} - \mathbf{p4}] \times [\mathbf{p3} - \mathbf{p7}] \tag{7.1}$$

and

$$\mathbf{n_2} = [\mathbf{p2} - \mathbf{p3}] \times [\mathbf{p2} - \mathbf{p7}] \tag{7.2}$$

where **p1** to **p8** are the vectors representing the markers 1 to 8. The angle between $\overrightarrow{n_1}$ and $\overrightarrow{n_2}$ is equal to the LEF angle and is calculated using

$$\alpha_{LEF} = \arccos\left(\frac{\mathbf{n_1} \bullet \mathbf{n_2}}{|\mathbf{n_2}| \cdot |\mathbf{n_2}|}\right) \tag{7.3}$$

Finally a moving average smoothing with a period of 5 measurements is applied to the LEF angle to reduce noise.

Camber The camber (h) is defined as the $\triangle h$ divided by the chord, where $\triangle h$ is the largest distance between the wing cross section and the chord line, normal to the chord line. The camber is calculated using the markers 3 to 6, were it is unknown if marker 4 or 5 has the largest deviation, so $\triangle h$ is calculated for both markers where the largest one is used for the camber. For marker 4 $\triangle h$ is calculated using

$$\triangle h = \frac{|[\mathbf{p6} - \mathbf{p2}] \times [\mathbf{p4} - \mathbf{p2}]|}{|[\mathbf{p6} - \mathbf{p2}]|} \tag{7.4}$$

and the camber is calculated using

$$h = \frac{\triangle h}{|[\mathbf{p6} - \mathbf{p2}]|} \tag{7.5}$$

This is the camber of the fifth digit, including the LEF. To be able to compare the camber with real bats, the camber is also calculated for the fifth digit excluding the LEF because this method is also used by Busse von (2011). This camber is calculated in the same way, only maker 2 is replaced by marker 3 to exclude the LEF.

Angle of attack The angle of attack is different for every point on the wing because of the flapping motion. In this case, α_{eff} of the outer wing, or the triangle spanned by markers 3, 6 and 8 is used because this part of the wing is generates the largest part of the lift. More specific, the centroid of this triangle is used, calculated by

$$\mathbf{C} = \frac{\mathbf{p3} + \mathbf{p6} + \mathbf{p8}}{3} \tag{7.6}$$

The centroids velocity ($\mathbf{U_c}$) is calculated using the derivative of a piecewise polynomial fit of the centroids coordinates. A moving average smoothing (period equal to 10 measurements) is used to reduce noise. This velocity is used to calculate the total effective velocity

$$\mathbf{U_{\infty,eff}} = \mathbf{U_\infty} - \mathbf{U_c} \tag{7.7}$$

And together with the surface normal of the outer wing triangle:

$$\mathbf{n_3} = [\mathbf{p3} - \mathbf{p6}] \times [\mathbf{p3} - \mathbf{p8}] \tag{7.8}$$

the angle of attack is calculated using equation 7.9.

$$\alpha_{eff} = 90 - \arccos\left(\frac{\mathbf{U_{\infty,eff}} \bullet \mathbf{n_3}}{|\mathbf{U_{\infty,eff}}| \cdot |\mathbf{n_3}|}\right) \cdot \frac{180}{\pi} \tag{7.9}$$

Inflow angle and effective velocity magnitude With the effective velocity calculated in the previous paragraph, the inflow angle can be calculated by

$$\alpha_{flap} = \arctan\left(\frac{U_{\infty,eff_z}}{U_{\infty,eff_x}}\right) \tag{7.10}$$

Where U_{∞,eff_z} and U_{∞,eff_x} are respectively the components of $U_{\infty,eff}$ in the z and x-direction. The magnitude of this velocity is calculated by

$$U_{\infty,eff} = |\mathbf{U_{\infty,eff}}| \tag{7.11}$$

7.2 Wake PIV data

The aerodynamic data is gathered with a PIV system as described in section 6.2. Each measurement has a duration of 4 seconds with a frame-rate of 200 frames per second resulting in 800 frames per measurement and 80 frames per period. The raw data of four frames from one period can be found in appendix E as example. With these images the first post-processing step (pre-postprocessing) is done with LaVision software from Davis. The resulting vector fields are exported and further analyzed with the use of Matlab.

Pre-postprocessing using DaVis The LaVision package from DaVis (7.4.0.122) is used to analyze the PIV images with a multi-pass 2D cross-correlation. An interrogation window size of 64x64 pixels is used for the first pass, followed by two passes with an interrogation window size of 32x32 pixels. These interrogation windows have an overlap of 50 percent. After this multi-pass cross-correlation a 3x3 smoothing is applied to reduce noise. This method is applied for both camera's separately because they both have a different measurement domain. Because only one camera is used for the calculation of one velocity field a parallax effect is present in the measurements, resulting in an outward radial velocity component in the results that is not present in the real flow. This effect is caused by the fact that particles that have a velocity towards the camera appear to move outwards on the image of this camera (as is illustrated in figure 7.2) To reduce this error the velocity fields without disturbance although still with the parallax effect are subtracted from the measurements. For this purpose images are recorded without the wing in the measurement domain. Finally the vector fields are exported to be able to use them in Matlab for further analysis.

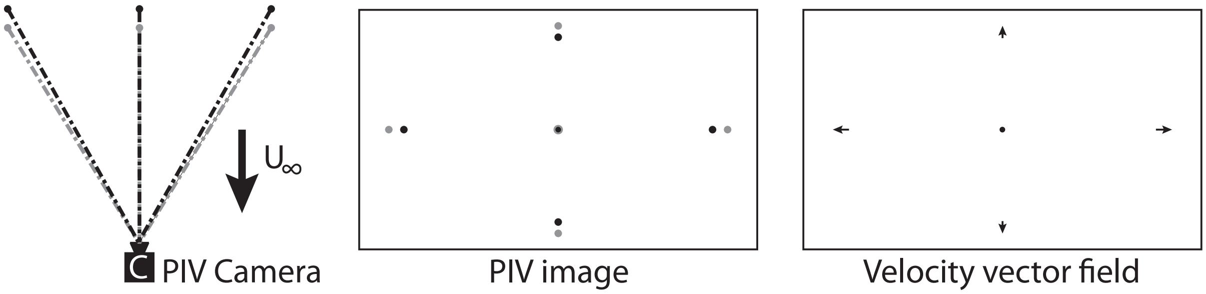

Figure 7.2 – Illustration of the parallax effect. The dots represent particles in the flow, where the grey dots are particles illuminated a small time step after the black particles. From the PIV image in the middle a velocity vector field is calculated according to the image on the righthand side.

Post-processing using Matlab Because the total measurement domain consists out of two different domains each captured by a different camera, the two resulting velocity fields had to be stitched together. This is done using a custom Matlab routine using the known distance between the two velocity fields to position them at the right location. Besides that, an inbuilt Matlab interpolation scheme is used to make the location of the vectors in the two velocity fields corresponding and using these vector fields, the vectors in the overlapping area are averaged. The result is a smooth transition between the two velocity fields (figure 7.3) although at the boundaries of the overlap two lines are slightly visible in the resulting vorticity field. The error made on these boundaries never exceeds the cut-off value of the traced vortices and is therefore assumed to be negligible.

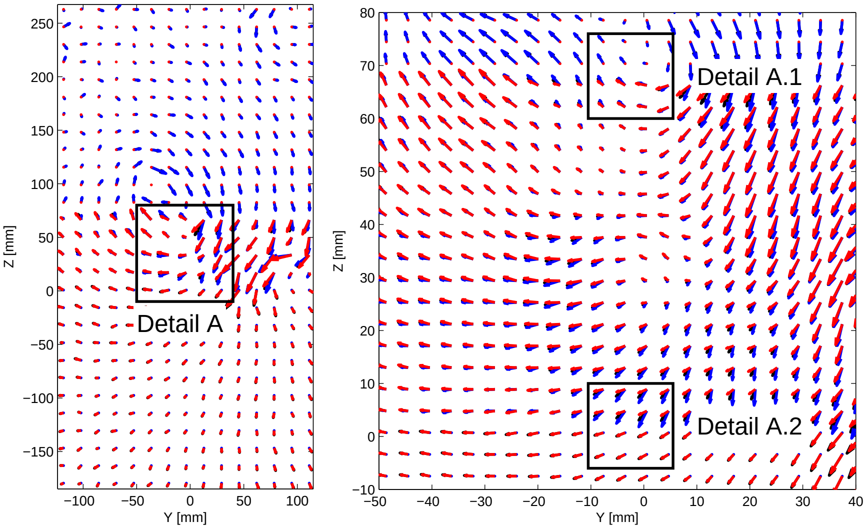

(a) Stitched wake velocity field

(b) Detail A

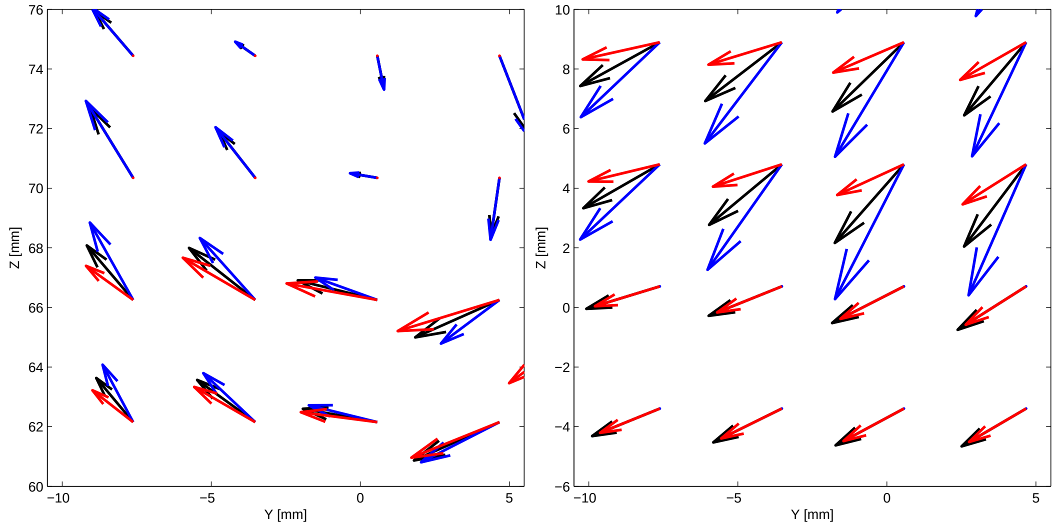

(c) Detail A.1

(d) Detail A.2

Figure 7.3 – Stitched velocity field with blue arrows indicating the velocity of the upper domain, the red arrows of the lower domain and the black arrows the result of the stitching process in the overlap of the upper and lower domain. In sub-figure 7.3a the total field is represented and in sub-figure 7.3c and 7.3d a detailed view (as defined in sub-figure 7.3b) of the upper and lower boundaries of the overlap are shown.

After stitching, the new velocity fields are used to calculate the velocity fields of an average period for each measurement. The starting point of these periods is determined with the raw PIV images and is defined as the frame were the wing was in the most upper position just at the start of the downstroke. It is important to note that there is a delay for the aerodynamic data compared to the kinematic date due to the convection time. The aerodynamic measurements were taken approximately one chordlength behind the trailing edge of the wing.

With these averaged periods three types of vortices are analyzed using a custom Matlab routine described by Muijres et al. (2011). With the use of this Matlab routine the vortices are manually identified and labeled, after which the circulation and position is calculated. The circulation is determined by integrating the vorticity over the vortex area. This area is limited by a minimum vorticity (ω_{min}) in this case $30s^{-1}$ because this is higher than the maximum vorticity ($\sim 10s^{-1}$) in the background flow and low enough to capture a large part of the vortices. Because this boundary cuts of a part of the vortex and thereby gives an underestimation of the circulation of the vortex, a correction (Spedding et al., 2003) is applied in the form of

$$\Gamma_{vort} = \frac{1 + |\omega|_{min}}{|\omega|_{max}} \Gamma'_{vort} \tag{7.12}$$

to get a more accurate value. Γ'_{vort} is the resolved circulation inside the vortex boundary and $|\omega|_{max}$ the maximum vorticity of the vortex. This correction is derived assuming the vorticity in a vortex has a Gaussion distribution. The location of the vortex is defined as the position of the maximum vorticity.

The first vortex is defined as the tip-vortex, although this does not mean it is always shed from the tip. During the downstroke, this vortex is assumed to be shed from the tip and is the most prominent vortex. Depending on the measurement the tip-vortex has disappeared at the start of the upstroke or moves inward and disappears in the first part of the upstroke. The second and third vortices are most of the time part of a dipole vortex structure and are therefore called negative and positive dipole vortex (negative circulation is a sign of positive lift production and positive circulation is a sign of negative lift production).

With the amount of circulation and position of the vortex, an estimate is made for the force corresponding with this vortex according to the method described by Muijres et al. (2011). This method ignores viscosity, resulting in conservation of vorticity in the wake. Using this assumption, each spanwise change in vorticity on the wing will result in a vortex line in the direction of the local streamline. In practice, these vortex lines interact with each other and roll up into a distinct vortex. Assuming the strength and location of this vortex would be the same as a vortex produced by a wing with spanwise constant lift production with a semi-span equal to the semi-span of the vortex, the resulting force production is equal to equation 7.13.

$$F_{vort} = \rho U_{\infty} 2 \cdot b_{vort} \Gamma_{vort} \tag{7.13}$$

were b_{vort} is the semi-span between the vortex and its imaginary counterpart, or in other words the y-directional distance between the vortex position and the body centerline.

7.3 Onwing kinematic data

The onwing kinematic data is gathered from the images recorded by the PIV camera. An example of these images can be found in appendix E. The kinematics of the leading and trailing edges of the wing at the measured cross-section are manually tracked with software described by Hedrick (2008). From these two points the local pitching angle, local chord and the velocity of the midpoint are determined.

Based on the measured wing kinematics the local Reynolds number Re_{loc}, local Strouhal number St_{loc} (Muijres et al., 2012) and the local Rossby number Ro_{loc} (Lentink, 2008) are calculated using equation 7.14, 7.15 and 7.16

$$Re_{loc} = \frac{c_{loc} \cdot U_{\infty,eff}}{\nu} \tag{7.14}$$

where c_{loc} is the local chord length.

$$St_{loc} = \frac{0.5 \cdot U_{z,wing}}{U_{\infty} + U_{x,wing}} \tag{7.15}$$

with $U_{z,wing}$ being the local z-component of the wing velocity and $U_{x,wing}$ the local x-component of the wing velocity.

$$Ro_{loc} = \frac{U_{\infty,eff}}{\dot{\theta}_{loc} \cdot c_{loc}} = \frac{U_{\infty,eff} \cdot b_{loc}}{U_{wing} \cdot c_{loc}} \tag{7.16}$$

where $\dot{\theta}_{loc}$ is the local angular velocity and b_{loc} is the local semi-span. The Rossby number is a measure for the importance of the Coriolis acceleration due to rotation in the flapping motion.

7.4 Onwing PIV data

The aerodynamic data is gathered from analyzing the PIV images using DaVis (7.4.0.122) with a multi-pass 2D cross-correlation (32x32, 16x16, 50% overlap) and a 3x3 smoothing average post-processing. From every period one frame at mid downstroke is selected and analyzed resulting in nine frames per measurement sequence with close to identical geometry and phase because of the repetitive motion of the model. These nine frames are averaged using Davis and analyzed with a custom made Matlab routine (Muijres et al., 2011) to determine the circulation. For every measurement configuration five measurement sequences were used to calculate a mean value and a standard deviation. The total procedure is displayed in figure 7.4. The circulation was determined above the wing cross-section using a semicircle defined by the line through the leading and trailing edge of the cross-section obtained from the kinematics and 70% of the local chord as radius to be able to capture all the relevant vortices. An example of this area and the corresponding vortices are shown in figure 7.5.

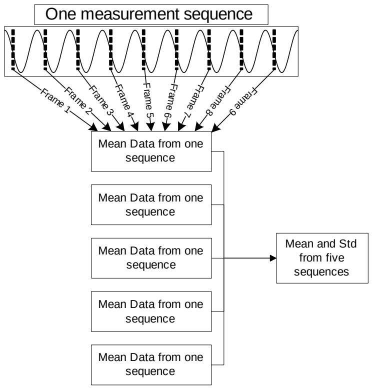

Figure 7.4 – Data acquisition of five measurements from one measurement set resulting in a mean value and its standard deviation

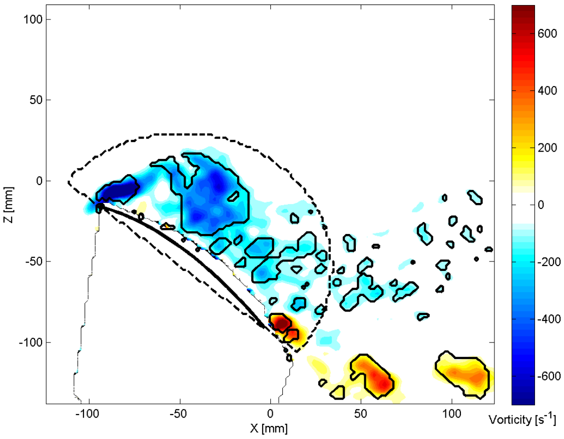

Figure 7.5 – Vorticity field ($\alpha_{eff} = 48°$ and $U_{eq} = 5.2$ m/s) with swirl strength contours (solid line) and semi circle domain (dashed line)

Because of the turbulent character of the flow fields at high angles of attack, the swirling strength (λ_{ci}) criterion is used for identifying vortices (Adrian et al., 2000). The swirling strength is determined by the imaginary part of the eigenvalues of the two dimensional gradient tensor. The gradient tensor is determined by

$$\mathbf{D} = \begin{bmatrix} \frac{\partial u_1}{\partial x_1} & \frac{\partial u_1}{\partial x_2} \\ \frac{\partial u_2}{\partial x_1} & \frac{\partial u_2}{\partial x_2} \end{bmatrix} = \begin{bmatrix} \frac{\partial v}{\partial y} & \frac{\partial v}{\partial z} \\ \frac{\partial w}{\partial y} & \frac{\partial w}{\partial z} \end{bmatrix} \tag{7.17}$$

Where v is the velocity component in y-direction and w in z-direction. In this case negative vorticity was used for the circulation (Γ_{vort}) if the swirling strength was larger than 5% of the maximum, resulting in boundaries as shown in figure 7.5. The total area within these boundaries is used as a measure of the size of the vortices (S_{vort}). The circulation was used to calculate the circulation coefficient (c_Γ) according to equation 7.18.

$$c_\Gamma = \frac{\Gamma_{vort}}{U_{\infty,eff} \cdot c_{loc}} \tag{7.18}$$

CHAPTER 8

Results

8.1 Evaluation of the RoBat wing kinematics

For evaluation of the RoBat model, the kinematic measurements (using the mean of 5 measurements) are compared with the simulated data and the measurements done with real bats (Busse von, 2011) in figure 8.2, 8.3 and 8.4. The RoBat is not capable of performing motions like contracting, yawing and active deforming, which results in an undesired difference between the RoBat and bat kinematics. Furthermore it is important to note that the kinematics of the RoBat are a simplified version of the bat wing kinematics and the optimization of the RoBat motions is not with the intention to increase the resemblance between those two kinematics but to achieve an equivalent aerodynamic situation. This results in an intended difference between the RoBat and bat wing kinematics. The combination of both differences results in the difference between the RoBat and real bats that is clearly visible in figure 8.1. There are two major differences between the RoBat and bats kinematics visible. The absence of the contracting motion is most present and clearly visible in figure 8.1b. The bats show a different upstroke, compared to the downstroke because the wing is more contracted during the upstroke and for the RoBat this difference is negligible. Secondly, the geometry of the RoBat is not the same as the one of a bat wing because of design restrictions as explained in section 5.1. This shows most obvious in the top view (figure 8.1d), where it can be seen that the RoBat has a larger sweep angle than bats. Moreover there is a small difference between the simulated coordinates and the measured coordinates from the RoBat, this difference is most likely caused by the absence of deformations in the simulation and geometrical inaccuracies of the construction of the RoBat.

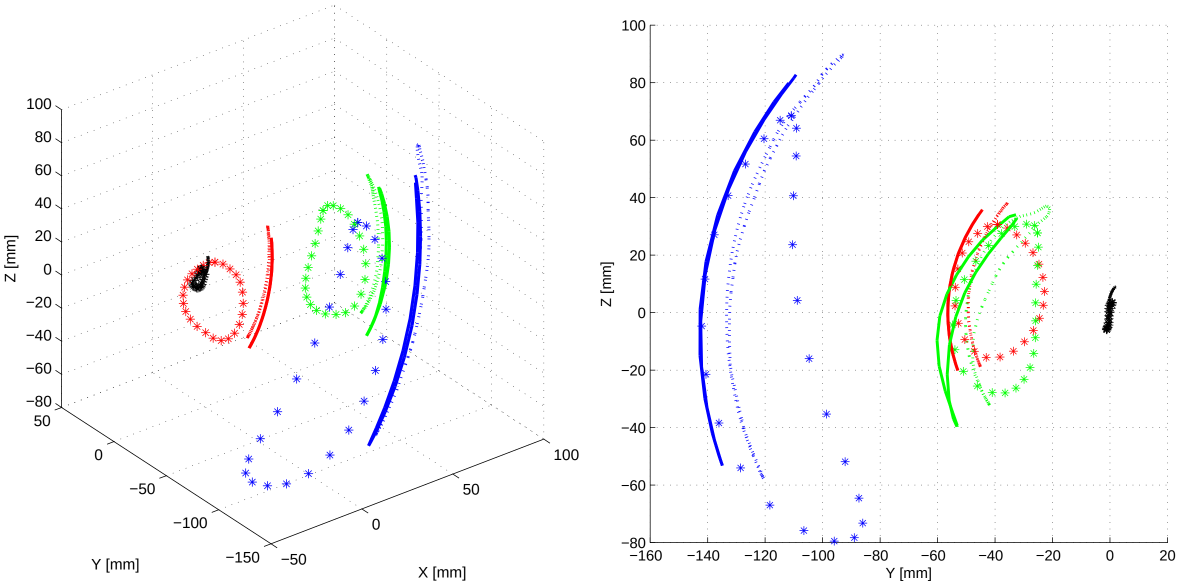

(a) Isometric view

(b) Rear view

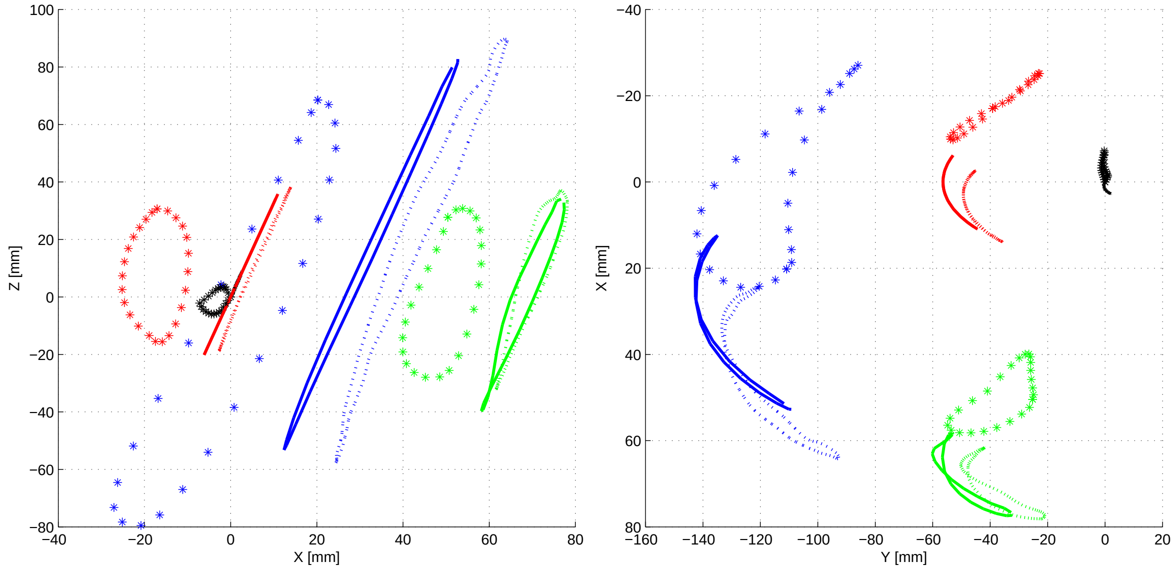

(c) Side view

(d) Top view

Figure 8.1 – Three dimensional coordinates from the RoBat wing (dashed line), the simulation (solid line) and a bat wing (asterisks). The points showed are; the shoulder (black), the wrist (red), the wing tip (blue) and the trailing edge of the fifth digit (green).

In figure 8.2 the flapping and pitching motion of the RoBat, simulation and bat is shown for comparison. As described before, there is a desired difference between the simulated motions and the bats motions, but in addition there is a difference between the simulated and actual RoBats motions. This difference is unwanted and caused by uncertainties and elastic deformations due to aerodynamic and inertia forces. The measured flapping motion is close to the desired (simulated) motion with a small overshoot and delay at the negative maximum. This can be explained by deformations caused by inertia forces, but it would be expected to happen at both the positive and negative maximum. The pitch angle in figure 8.2b shows a different behavior than simulated. There is an overshoot in the downstroke, resulting in a too large pitch down angle. As will be shown later, this will result in a lower angle of attack than desired. The pitch up angle is lower than the desired simulated motion during the upstroke, in contrast the pitching motion is more similar to the bats pitching motion during the upstroke. This will result in more pitch down angle of attack during the upstroke than desired.

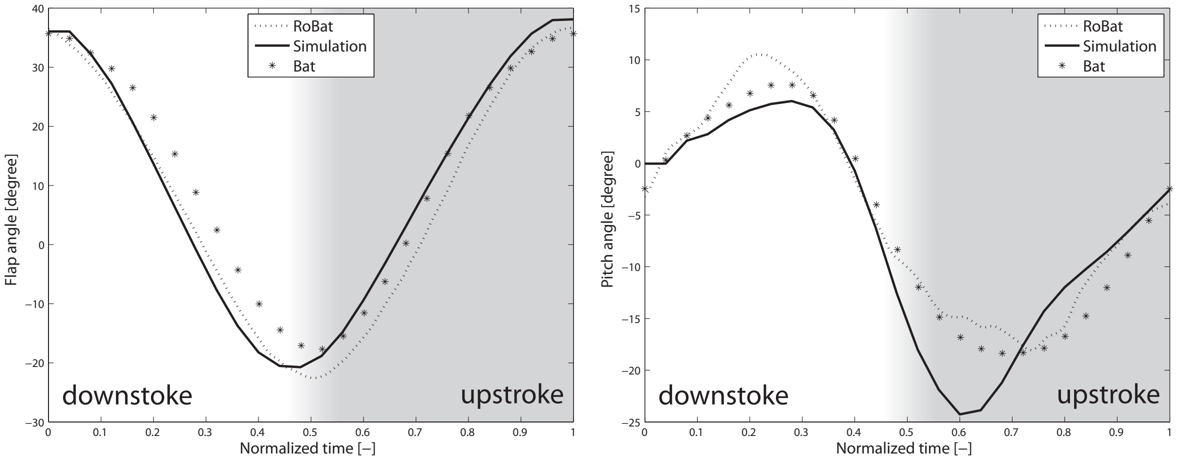

(a) **(b)**

Figure 8.2 – Comparison between RoBat measurements, simulated values and bat measurements, showing the flap (a) and pitch (b) angle for one period.

Other interesting parameters that can be determined from the kinematic data are the LEF angle and the camber. These are shown in figure 8.3. The sine shape is clearly visible in the LEF angle but, specially during the upstroke, the LEF angle is larger than desired. Again, a positive angle means downwards, which results in a more positive total camber during the upstroke than desired. The camber, excluding the LEF is not actively altered, but as can be seen in figure 8.3b there is still a variation of 1 percentage point, which must be due to passive deformation. The deformation of the camber shows some resemblance with the deformations of the bats camber. This would suggest that at least part of the change in camber is due to passive deformation.

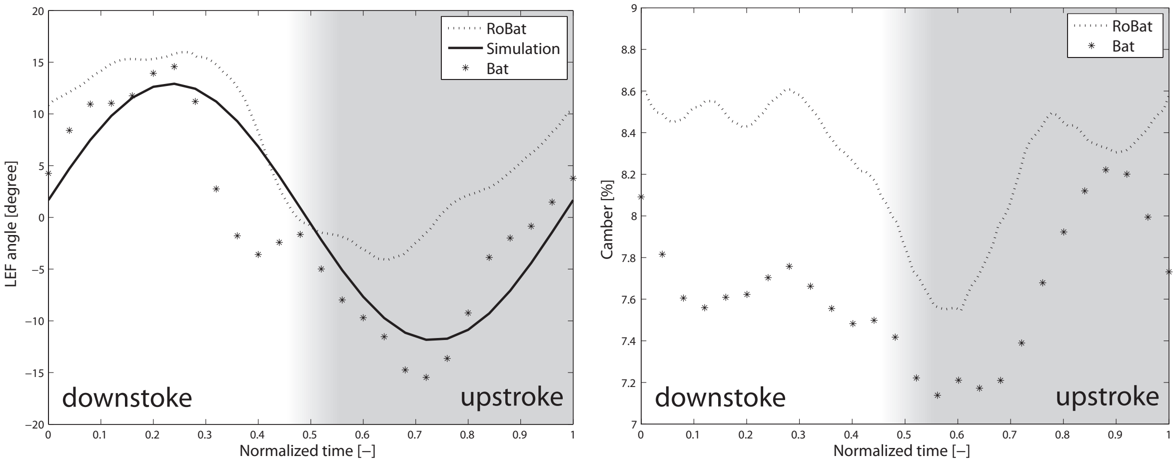

(a) (b)

Figure 8.3 – Comparison between RoBat measurements, simulated values and bat measurements, using the LEF angle (a) and camber (b) for one period.

The angle of attack, inflow velocity and inflow angle are calculated using the kinematic data and the free stream velocity. These parameters mostly coincide with the simulated values, although the simulated values for the inflow velocity are different than the one for bats because there is no yawing motion incorporated in the RoBat model. The errors with most effect are made in the angle of attack, these are too low in the first part of the downstroke, too high in the second half of the downstroke and too low again during the upstroke, resulting in high negative angles of attack in the upstroke. Most likely these differences between desired and measured angle of attack will be visible in the aerodynamic data.

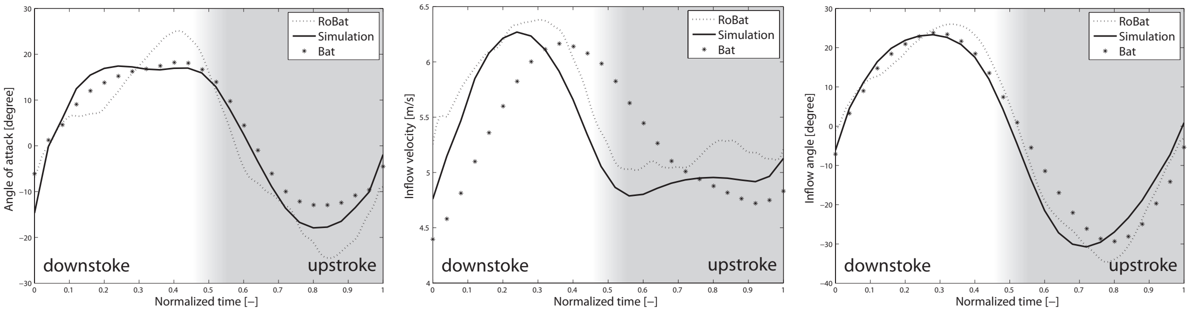

(a) (b) (c)

Figure 8.4 – Comparison between RoBat measurements, simulated values and bat measurements, using the angle of attack (a), inflow velocity (b) and inflow angle (c) for one period.

8.1.1 The influence of aerodynamic and inertia forces

Two extra measurements are performed at zero free stream velocity. One measurement at the normal frequency equal to 2.5 Hz and one at 0.5 Hz. The absence of a free stream velocity will decrease the overall aerodynamic forces and the lower frequency will decrease these aerodynamic forces even more and will reduce the inertia forces too due to lower accelerations. For both measurements, the sample number is 100 to assure an equal accuracy. The difference is clearly visible in figure 8.5 and 8.6. The flap angle shows a small delay for the lowest maximum and an overshoot in both directions for the low frequency case. These overshoots indicate that the wing is not reaching the desired amplitude due to deflections. The pitch angle shows a large difference in the downstroke between the low and high frequency case. In contrast to the low frequency case, the high frequency case has a second peak before its global maximum. It is possible that the increasing lift force during the downstroke causes a pitch down moment causing a oscillation in the pitch angle. Another possibility is that the servo motors have problems with the high frequency, introducing unwanted vibrations resulting in an oscillation in the pitching angle.

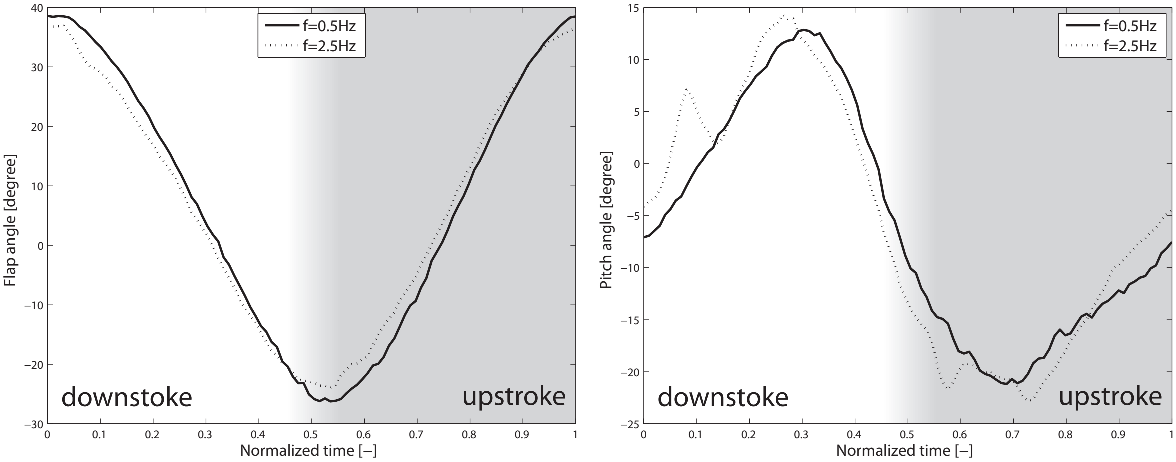

(a) (b)

Figure 8.5 – Comparison between 0.5 Hz and 2.5 Hz flapping motion using the flap (a) and pitch (b) angle for one period.

In figure 8.6 the effect of the high frequency can be distinguished for the LEF angle and camber. The difference between the high and low frequency case for the LEF angle is most likely caused by internal friction and low torsional stiffness of the carbon rod that transfers the LEF motion. As a result, the LEF is not reaching the desired value for the high frequency case. From figure 8.6b it is clearly visible that the camber is oscillating more for the high frequency case, but follows the same trend as the camber of the low frequency case.

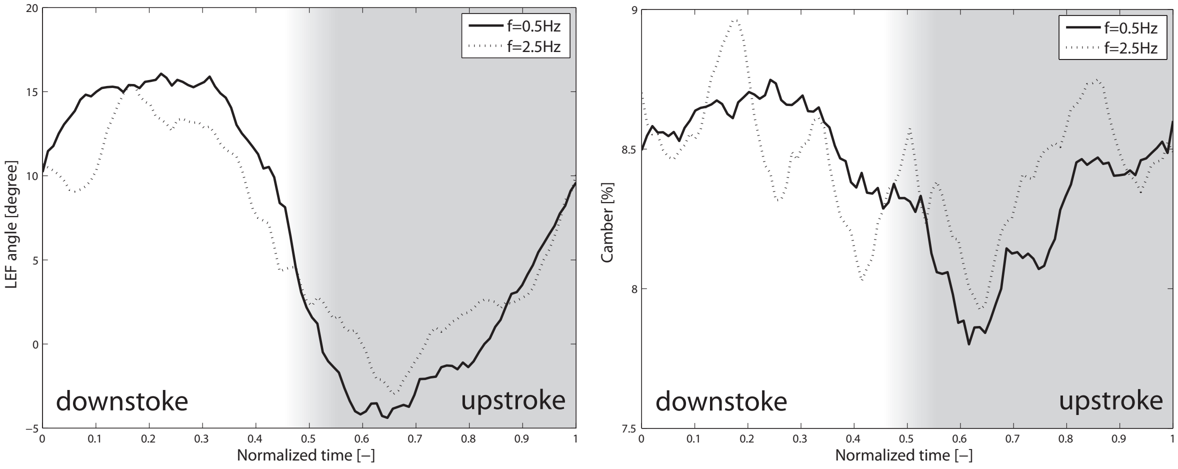

(a) **(b)**

Figure 8.6 – Comparison between 0.5 Hz and 2.5 Hz flapping motion using the LEF angle (a) and camber (b) for one period.

Overall the kinematics from the RoBat are comparable with the one from real bats, which makes it possible to compare the aerodynamic data of the RoBat with the data of real bats. Nevertheless it is important to keep in mind, that the RoBat uses simplified kinematics and materials. Also the oscillation in the pitching angle, and therefore in the angle of attack, will give a different aerodynamic behavior.

8.2 Aerodynamic analysis of the RoBat wing flow field.

From the PIV measurements, flow fields are derived from the wake in a plane perpendicular to the free stream velocity direction. In this section, these flow fields are analyzed for comparison with respect to the flow field produced by bats and to analyze the influence of the LEF motion.

8.2.1 Comparison of the RoBat wing flow field with respect to real bats.

Comparison of the 3D representation of the vorticity iso-surfaces

The time-resolved two dimensional PIV data that is gathered over one period (in the time domain) can be transformed to a three dimensional representation using the transformation based on the Taylor hypothesis:

$$\triangle x = U_\infty \triangle t \tag{8.1}$$

The iso-surface of the streamwise component of vorticity of the resulting flow field is shown in figure 8.7 and 8.8. For these figures a symmetrical wake is assumed to be able to construct the total wake from the measurements from one wing and it's mirror image. These iso-surfaces give information about the size and sign of the vortices present in the flow behind the wings. This gives the possibility to get a better understanding of the vortex structures and to compare real bats with the RoBat. The overall structure of the vortices of the RoBat is similar to that of real bats. During the downstroke, there is a strong tip vortex that moves more inwards at the end of the downstroke and disappears. At the beginning of the upstroke a dipole structure is formed, which is present during the upstroke. The most striking difference between bats and the RoBat is at the start of the downstroke, were the RoBat is not able to generate the same size of tip vortex as real bats. This is consistent with the too low α_{eff} in the first part of the downstroke. Next to that, in the second part of the upstroke the inward part of the dipole structure disappears. In the middle of the wake, no data is available. This makes it difficult to draw conclusions about the total lift production, but both differences make it very likely that the RoBat is producing less lift than real bats.

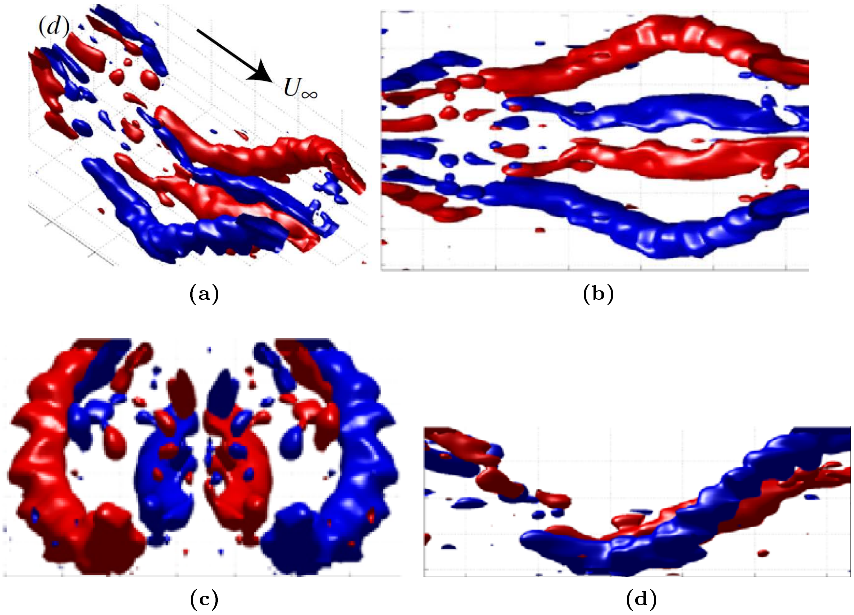

(a) (b)

(c) (d)

Figure 8.7 – Four views of the iso-surfaces (cut-off value = $60s^{-1}$) of the streamwise component of vorticity in the wake of a *Leptonycteris yerbabuenae* for one wingbeat at a flight speed of 6.3 m/s. Positive vorticity is colored red and negative blue.(Muijres et al., 2011)

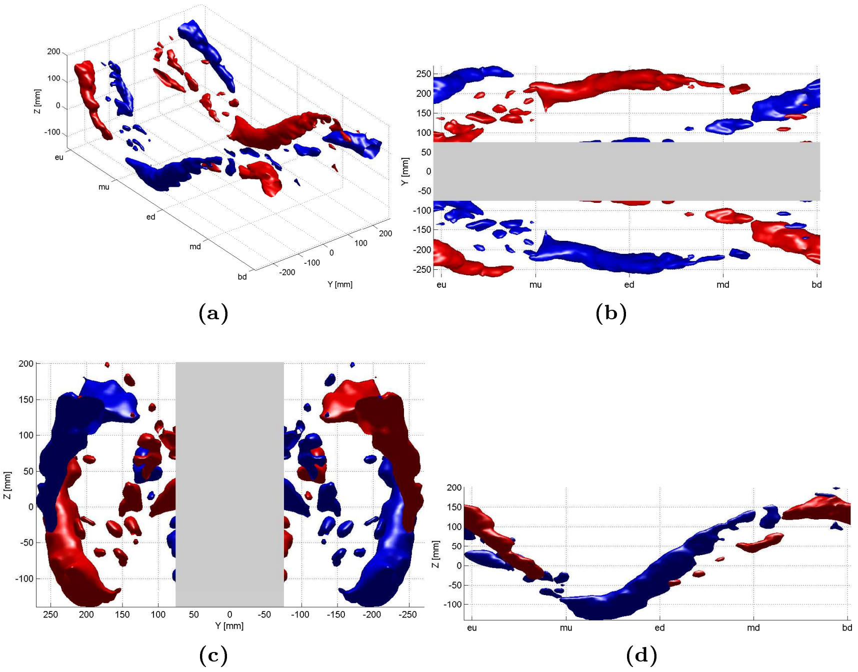

(a) (b)

(c) (d)

Figure 8.8 – Four views of the iso-surfaces (cut-off value = $30s^{-1}$) of the streamwise component of vorticity in the wake of the RoBat for one wingbeat at an equivalent flight speed of 5.1 m/s. Positive vorticity is colored red and negative blue. In the gray area no data is available.

For comparison with real bats, the vorticity iso-surfaces are chosen to visualize the vortex structures. This method has the disadvantages that it is very sensitive to the used cut-off value and that vorticity consists out of rotation and shear of the flow field. When rotation is the main focus, which is the case for vortex structures, the swirl might be a better quantity to use. The swirl is calculated as described in section 7.4 and is less sensitive for the used cut-off values because the gradients in the swirl field are much larger than these in the vorticity field. The resulting swirl iso-surfaces (cut-off value is equal to 5% of maximum swirl strength) are shown in figure 8.9 and show smaller vortices when they are strong (for example the tip vortex in the second half of the downstroke) and thicker vortices when they are weak (for example the tip vortex in the first half of the downstroke) compared to the vorticity iso-surfaces.

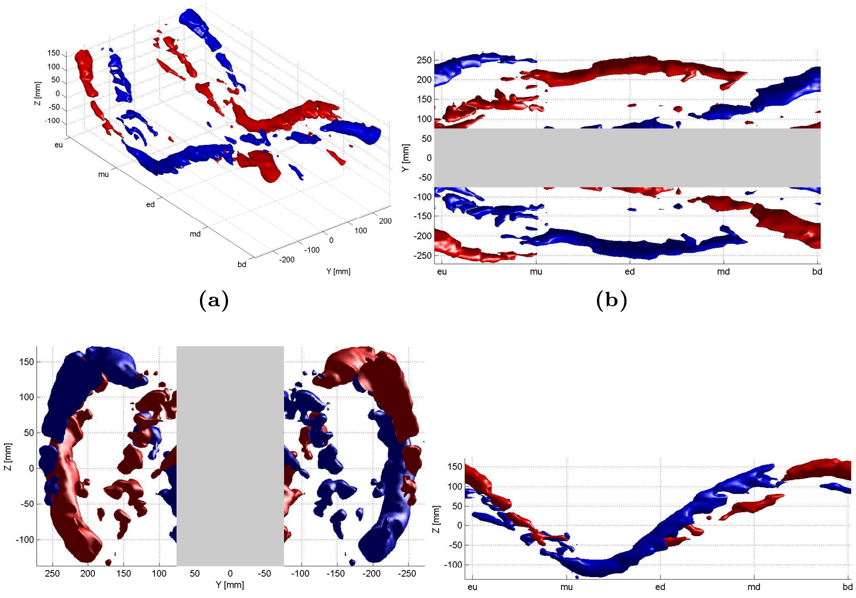

(a) (b)

(c) (d)

Figure 8.9 – Four views of the iso-surfaces (cut-off value = 5% of the overall maximum) of the swirl in the wake of the RoBat for one wingbeat at an equivalent flight speed of 5.1 m/s. Positive vorticity is colored red and negative blue. In the gray area no data is available.

Comparison of the circulation coefficients

A second comparison is made between bats and the RoBat wing by means of the circulation coefficient (c_Γ). This is done for the tip vortex and the outward vortex of the dipole structure. This last vortex is of opposite sign with respect to the tip vortex and causes a decrease in lift production. In figure 8.10a c_Γ is shown for both vortices for the configuration $U_{eq} = 5.1 {}^{m}/_{s}$ and $\beta = 73°$. For the tip vortex the maximum value of c_Γ is identical for bat and RoBat wing. On the other hand, the maximum value of the c_Γ for the outward vortex of the dipole is much higher for the RoBat wing compared to real bats. Also the values of c_Γ for the tip vortex are lower for the RoBat wing compared to real bats for the largest part of the wingbeat. This results in a too low lift production and possible different vortex structures. Partly these deviations in c_Γ can be explained by the deviations of α_{eff} found in section 8.1, because a lower α_{eff} will result in a lower value of the c_Γ.

In figure 8.10b, the same vortices are compared for a configuration with a higher body and thereby lower stroke plane angle ($U_{eq} = 5.1 {}^{m}/_{s}$ and $\beta = 68°$). This results in higher values for α_{eff} with the result that c_Γ decreases for the outward vortex of the dipole and c_Γ increases for the tip vortex. This results in a better match between the RoBat and bat wing.

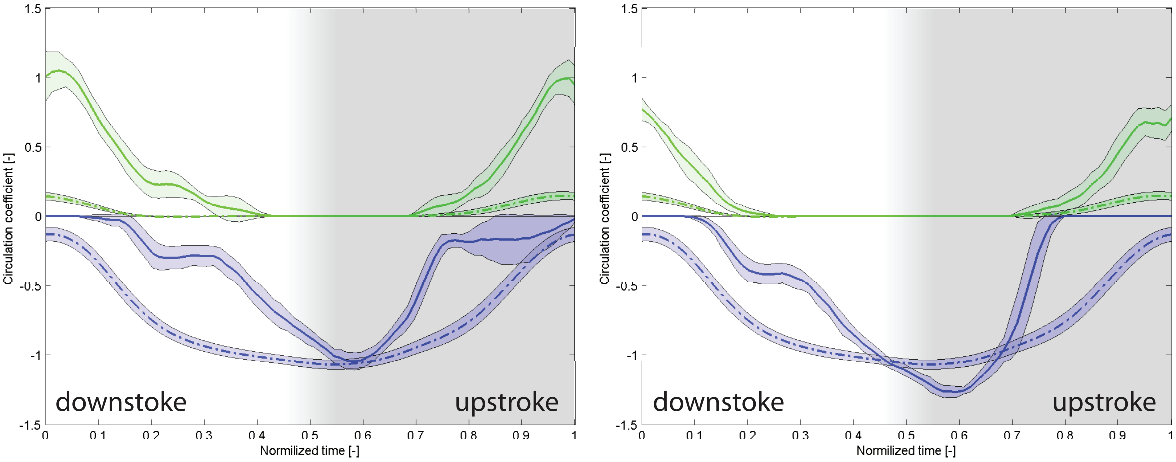

(a) Comparison of the circulation coefficient (c_Γ) of the RoBat wing (solid line) and bat wing (dashed line) with standard deviation for the configuration: $U_{eq} = 5.1 {}^{m}/_{s}$ and $\beta = 73°$. Green lines represent the outward vortex of the dipole and blue lines represent the tip vortex.

(b) Comparison of the circulation coefficient (c_Γ) of the RoBat wing (solid line) and bat wing (dashed line) with standard deviation for the configuration: $U_{eq} = 5.1 {}^{m}/_{s}$ and $\beta = 68°$. Green lines represent the outward vortex of the dipole and blue lines represent the tip vortex.

Figure 8.10

8.2.2 The influence of the leading edge flap on the aerodynamic performance

Both tests with and without LEF motion are performed to investigate the influence of the LEF. In the case with LEF motion, a sine shape motion is used and for the case without the LEF motion, the LEF is fixed at the average angle of the LEF motion. The measured LEF angles can be found in figure 8.11 where the case without LEF motion shows an almost constant LEF angle and the case with LEF motion shows a sin shaped LEF angle. Although the LEF angles are larger than desired the trend is equal to the LEF angles found at bats. The variation found in the measured LEF angle is most likely caused by uncertainties in the tracking of the two markers located at the leading and trailing edge of the LEF. These uncertainties have a large influence on the LEF angle, because of the small distance (∼13 mm) between the two markers.

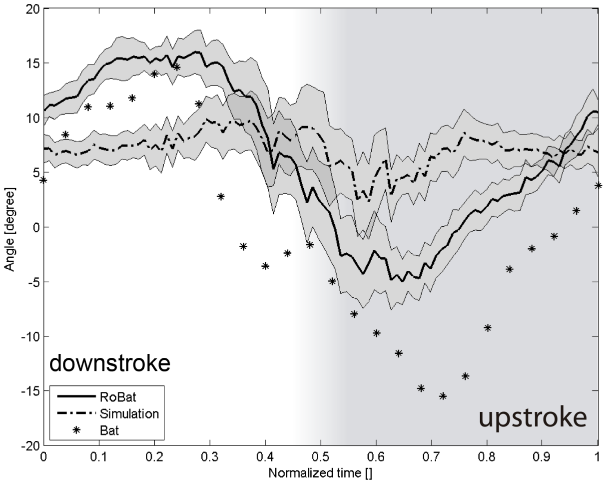

Figure 8.11 – LEF angle over one flapping period. Measurements of the RoBat with LEF motion (solid line) and without LEF motion (dashed lines) both with standard deviation boundaries compared with the LEF angle measured at a bat wing.

To find the influence of the LEF motion, the vortices in the wake are analyzed. This is done by quantifying the maximum vorticity, circulation and location of three vortices. These vortices are the tip vortex and the in- and outward part of the vortex dipole that is present during the upstroke as described in more detail in section 7.2. In figure 8.12 both the maximum vorticity and circulation are shown during one period, beginning at the start of the downstroke of the wing. From this comparison it is hard to draw conclusions because the standard deviation of both cases is large and the difference between the two cases is small. For a more detailed analysis, for all three vortices, the corresponding force is calculated according equation 7.13 and averaged over the total wingbeat. For a more general result, this is done for five configurations ($U_\infty = 2.3, \beta = 73; U_\infty = 2.6, \beta = 78; U_\infty = 2.6, \beta = 73; U_\infty = 2.6, \beta = 68; U_\infty = 2.9, \beta = 73$) with five measurements each, resulting in five results with and five results without LEF motion for each configuration. With these results, a double t-test is performed to find the significance of the LEF motion. The results of those five variations for the three vortices can be found in appendix D. In this tables the force production is shown together with the p-value of the hypotheses that the two sets (with and without LEF motion) are equal. The low p-values (<0.05) give an indication that the LEF motion has a significant influence on the force production. As can be seen in these tables, this is only the case for the overall force production in case of $U_\infty = 2.6, \beta = 73$. For this case, the positive force production of the configuration with LEF motion is ~14% lower than the configuration with a fixed LEF. The vortex that is responsible for this difference is the outward component of the dipole vortex structure, because this is the only vortex with a significant difference (also ~14% difference in force production). This vortex is active during the upstroke, so the influence of the LEF motion is also during the upstroke. The inward vortex of the dipole structure also shows a significant difference for the case $U_\infty = 2.6, \beta = 78$, but this difference is negligible for the total force production (<0.1% difference in force production). In all other cases, the difference is not significant and thus no proof is found for an increased force production due to LEF motion. It is important to note that a LEF deflection has influence on both the camber of the wing as the α_{eff}. In these experiments, the change in α_{eff} is not corrected.

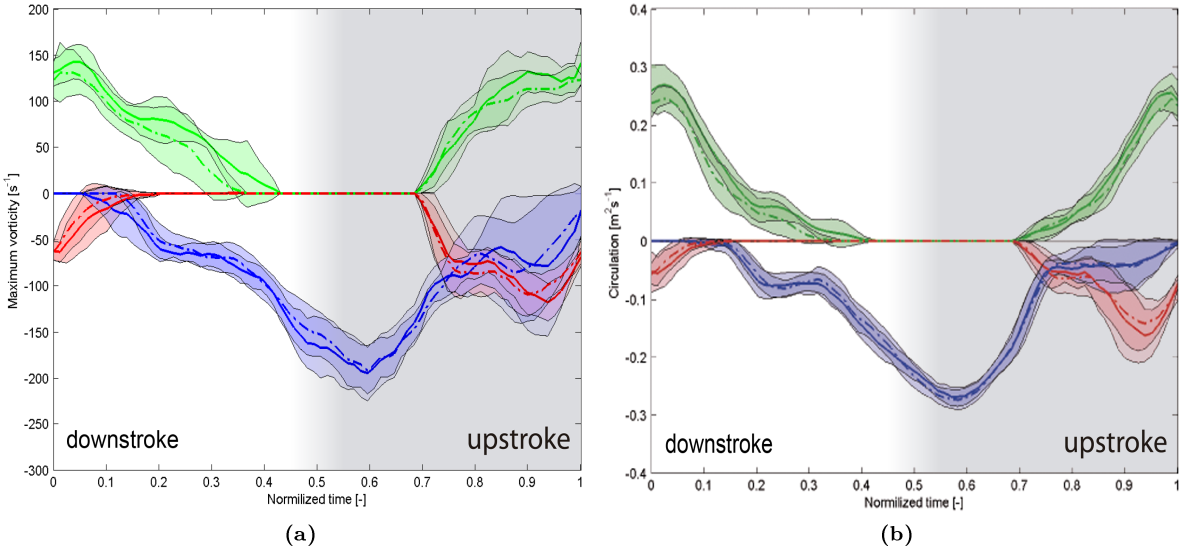

(a) (b)

Figure 8.12 – Maximum vorticity (a) and total circulation (b) for; the tip vortex (blue), inward vortex of the dipole (red) and outward vortex of the dipole (green). Solid lines are with a LEF motion, dashed lines without. Both are with U_∞ = 2.6m/s and β = 73. All are represented with standard deviation boundaries.

8.3 Onwing measurements results

For the onwing measurements two different cases (variable and constant α_{eff}) are used both consisting out of 5 configurations as described in section 6.5. Figure 8.13 shows the desired α_{eff}-U_{eq} based on the kinematics of *Leptonycteris yerbabuenae* and the measured α_{eff} at two locations on the wing. In this figure the variable α_{eff} case shown as the lower decreasing line and the constant α_{eff} case as the horizontal upper line. It is clear that the measured α_{eff} is generally lower than the required value, and this error increases both along the wingspan and with U_{eq}.

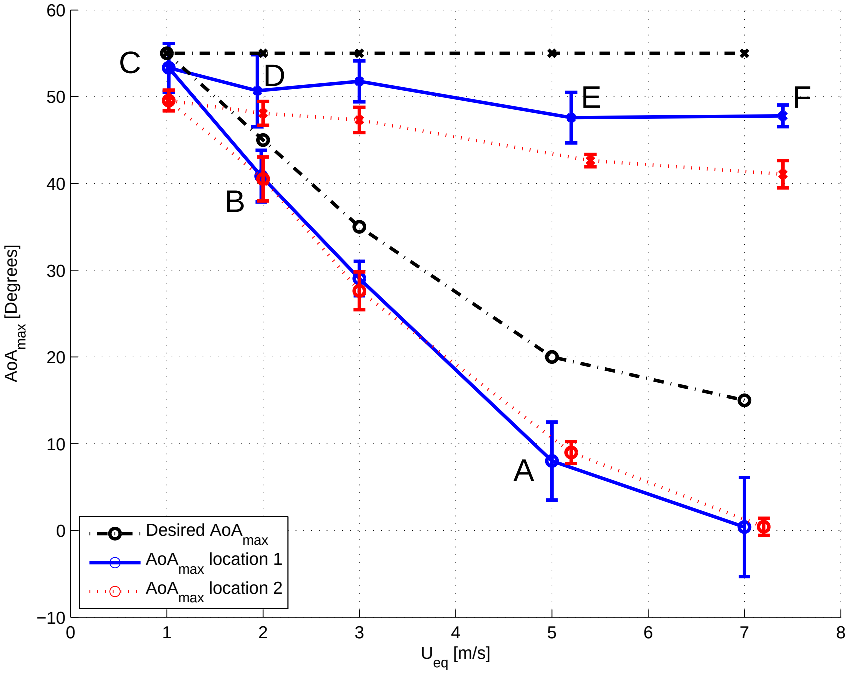

Figure 8.13 – Maximum angle of attack versus equivalent free stream velocity U_{eq} (with standard deviation error bars). Both the variable α_{eff} (lower decreasing line) and constant α_{eff} (upper horizontal line) cases are shown. The labels A-F are given for comparison with other figures.

8.3.1 Description of the flow field

To give a better understanding of the flow field around the RoBat wing, the instantaneous streamlines and vorticity values in the wing fixed reference frame for the configurations with labels A to F from figure 8.13 are shown in figure 8.14. The configurations with label A, B and C are configurations with decreasing U_{eq} and the α_{eff} found in bat flight. The configurations C, D, E and F are configurations with increasing U_{eq} and close to constant α_{eff}. The flow field in a wing fixed reference frame gives primarily information about the aerodynamic state of the flow, especially flow separation from the wing. The wing fixed reference frame flow fields are determined by subtracting the wing velocity in XZ plane from the flow fields in the wind tunnel fixed reference frame. Starting at α_{eff} = 8° and U_{eq} = 5 m/s (label A in figure 8.13 and figure 8.14a) a quasi steady state is clearly visible with very low values of vorticity. The slightly curved streamlines indicate some lift production, which corresponds with the low α_{eff}. At α_{eff} = 41° and U_{eq} = 2.0 m/s (label B in figure 8.13 and figure 8.14b) a clear separation bubble at the leading edge is visible with flow reattachment halfway along the chord. The shedding of trailing edge vortices, of opposite sense to the LEF, are an indication of an increase in lift production by the wing. The fact that the vorticity is not continuously shed, but in distinct vortices is probably due to a vibration in the trailing edge of the membrane. This vibration is also visible in the raw PIV images. At α_{eff}=53° and U_{eq}= 1.0 m/s (label C in figure 8.13 and figure 8.14c) the LEV has increased in size but reattachment still occurs upstream of the trailing edge. At α_{eff} = 51°and U_{eq} = 2.0 m/s (label D in figure 8.13 and figure 8.14d) the vorticity above the wing has suddenly greatly increased, reattachment does not occur anymore and the vortices that are generated at the leading edge of the wing are periodically shed into the wake. These characteristics are indicative of LEV bursting (Lentink and Dickinson, 2009). The burst vortex wake increases in size consistently with increasing flight speed (figure 8.14e: α_{eff} = 48°, U_∞= 2.6 m/s, and figure 8.14f: α_{eff} = 48°, U_∞= 3.7 m/s). Note that vortex bursting is a result of the change in U_{eq}, since the α_{eff} stays almost constant from figure 8.14c to figure 8.14f.

From figure 8.14a to 8.14c it can be seen that the RoBat wing produces comparable flow structures as real bats. Fully attached flow at high speeds and a LEV at low speeds. Figure 8.14c to 8.14f give extra information about how the flow field would look like if a bat would increase it's α_{eff} to an angle of attack from 48° to 53°, for example at high load turns. In this case, the LEV will burst and increase in size, but as will be shown in the next section, will still generate lift.

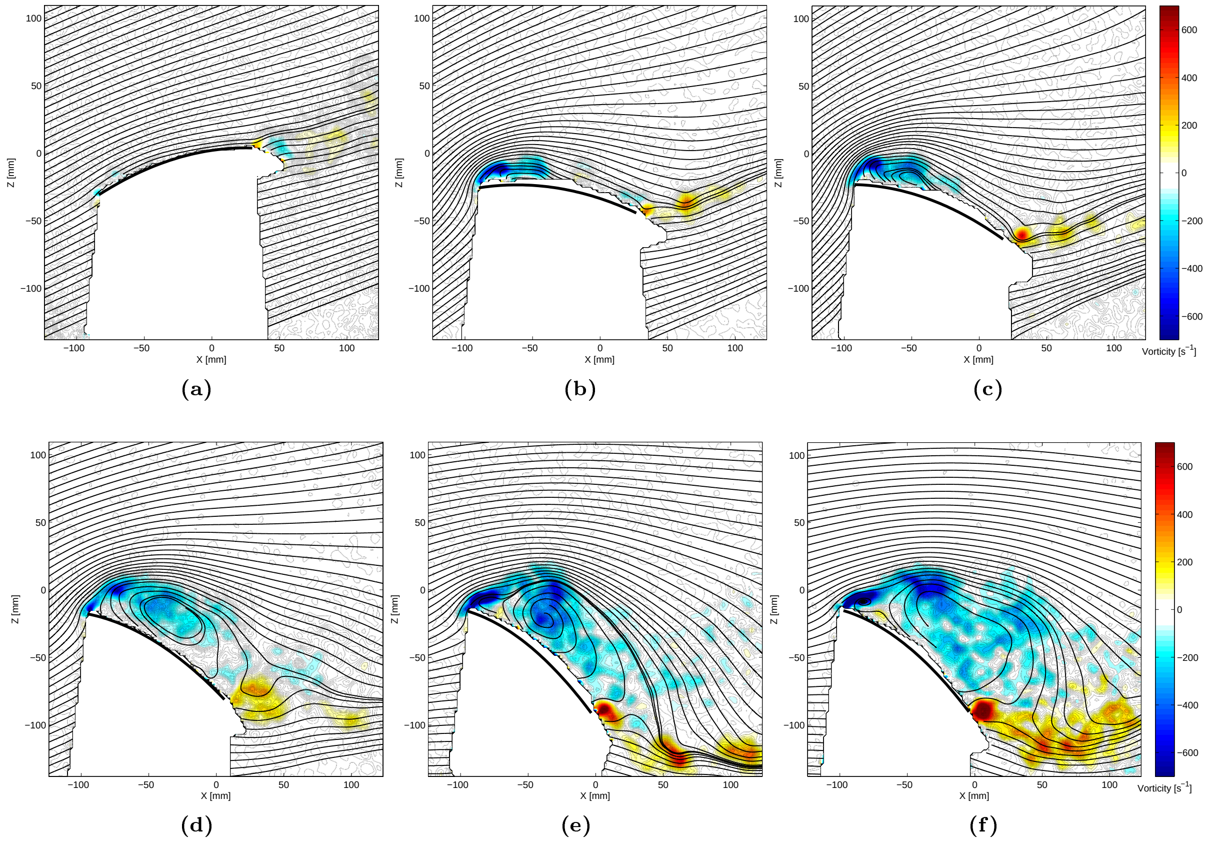

(a) (b) (c)

(d) (e) (f)

Figure 8.14 – Instantaneous streamlines and vorticity in the wing fixed reference system at location 1 for A: α_{eff} = 8°, U_{eq} = 5.0 m/s, B: α_{eff} = 41°, U_{eq} = 2.0 m/s ,C: α_{eff} = 53°, U_{eq} = 1.0 m/s, D: α_{eff} = 51°, U_{eq} = 2.0 m/s, E: α_{eff} = 48°, U_{eq} = 3.1 m/s, F: α_{eff} = 48°, U_{eq} = 7.4 m/s.

8.3.2 Vortex dynamics

The circulation coefficients (c_Γ) determined from the vortices positioned above the wing are plotted against Re_{loc}, $\alpha_{eff,loc}$, St_{loc} and Ro_{loc} in figure 8.15. The same is done for the vorticity area (S_ω) in figure 8.16. The increase in c_Γ occurs at an almost constant Re_{loc} (variable α_{eff} measurements in figure 8.15a), while c_Γ remains constant with increasing Re_{loc} (constant α_{eff} measurements in figure 8.15a). This shows that c_Γ is largely independent from Re_{loc}. The same is almost valid for S_ω although S_ω remains increasing for the constant α_{eff} measurements for an increasing Re_{loc} (figure 8.16a). Figure 8.15b shows that c_Γ is associated with α_{eff}. For the variable α_{eff} measurements, a weak LEV starts to occur at α_{eff}=30°, and its strength (c_Γ) and size (S_ω) increases almost linearly with α_{eff} up to $\alpha_{eff}>50$°(figure 8.15b).

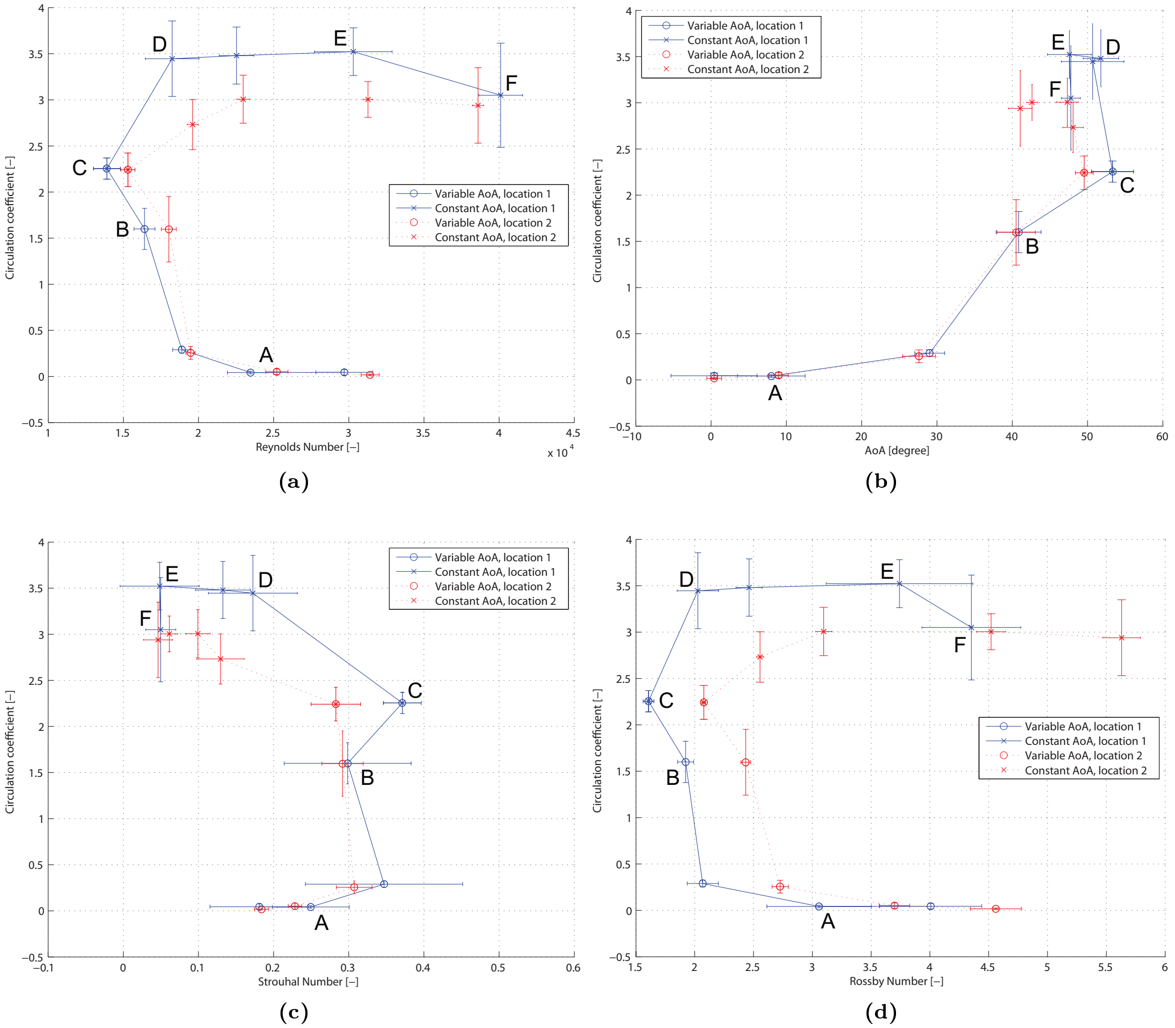

(a) **(b)**

(c) **(d)**

Figure 8.15 – Negative circulation coefficient in the semicircle above the wing with respect to Re_{loc} (a), $\alpha_{eff,loc}$ (b), St_{loc} (c) and Ro_{loc} (d) with labels A-F referring to figure 8.14. The error bars represent the standard deviation.

For the constant α_{eff} measurements, c_Γ increases initially with flight speed (figure 8.15b, label C-D), but then remains rather constant with a further increased speed (figure 8.15b, label D-F). The size (S_ω) increases a factor 3 to 4 for the constant α_{eff} measurements. The largest increase in c_Γ occurs also at a constant St_{loc} (~ 0.3, variable α_{eff} measurements in figure 8.15c), while c_Γ remains almost constant when St_{loc} decreases from 0.2 to 0.05 (constant α_{eff} measurements in figure 8.15c). Thus, c_Γ is also largely independent from St_{loc}. In contrast, S_ω seems to be St_{loc} dependent because for data points where S_ω is increasing the most, St_{loc} is decreasing almost linearly (figure 8.16c). The shape of the c_Γ-Ro_{loc} and c_Γ-Ro_{loc} curves (figure 8.15d and 8.16d) are comparable with the c_Γ -Re_{loc} and S_ω-Re_{loc} curves. This can be explained by the fact that for both quantities $U_{\infty,eff}$ is driving in this experiment.

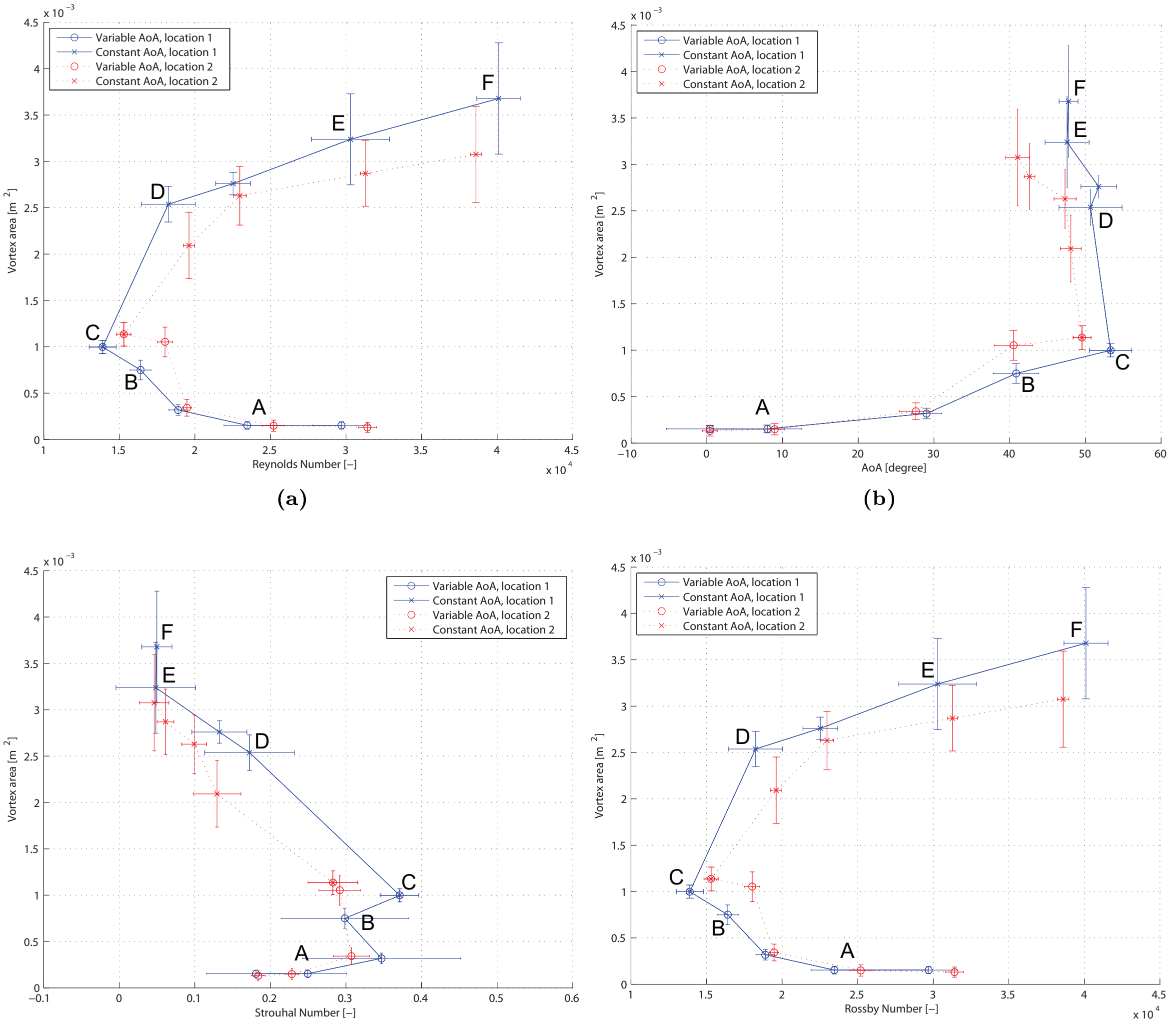

(a) **(b)**

(c) **(d)**

Figure 8.16 – Cumulative area of the vortices in the semicircle above the wing with respect to Re_{loc} (a), $\alpha_{eff,loc}$ (b), St_{loc} (c) and Ro_{loc} (d) , with labels A-F referring to figure 8.14. The error bars represent the standard deviation.

CHAPTER 9

Conclusions and recommendations

The kinematics of the RoBat show good resemblance with that of real bats in the flapping angle and LEF motion, but the absence of the yawing motion introduces an error in the inflow velocity and the deformations of the wing are causing deviations in the predicted kinematics. Both effects combined give a too low α_{eff} during the first half of the downstroke, a too high α_{eff} during the second half of the downstroke and a too negative α_{eff} during the upstroke. A possible improvement would be to optimize the pitch motion, which would result in α_{eff} closer to that of real bats . This optimization would be necessary for every configuration, because the resulting α_{eff} is dependent on deformations influenced by the specific aerodynamic and inertia forces for that configuration.

The kinematic measurements of the RoBat also show an interesting phenomenon in the camber. This camber is not actively adjusted in the RoBat and shows some resemblance with the camber measured at bats. This suggest that the camber change is partly due to passive deformation. Further research over the total flight speed range of bats could give more information about the active and passive part of the camber deformation.

For the onwing measurements the α_{eff} from the RoBat is lower than that corresponding to the real bat, but the general trends; increasing α_{eff} with decreasing U_{eq} for the variable α_{eff} case and almost constant α_{eff} for the constant α_{eff} case are clear. For all measurements the α_{eff} is lower than the required value, which is most likely due to a pitch down deformation introduced by the lift production. Since flight forces can be expected to increase with U_{eq}, the reduction in α_{eff} can be expected to be a result of spanwise pitch down wing twist as a result of lift production. This pitch down deformation is larger for the more outward, second location and therefore give a lower α_{eff} compared to the first location. In further research this phenomenon could be reduced by a larger torsional stiffness of the wing and a separate optimization of α_{eff} for each flight speed.

9.1 Wake measurements

From the wake measurements, the resemblance between the RoBat and real bats is clearly visible in vorticity iso-surfaces, although the tip vortex is smaller at the start of the downstroke for the RoBat wing. When quantifying the circulation of the RoBat wing it is shown that the tip vortex reaches the same circulation coefficient as a bat wing, but is lower over the largest part of the flapping period. The circulation coefficient of the outward vortex of the dipole structure shows the same trend compared to a bat wing, but is larger. These effects can be decreased by increasing the body angle and thereby α_{eff}. Also the absence of the contracting motion is clearly visible in the wake measurements resulting in less movement in the y-direction of the vortices.

The analysis of the influence of the LEF motion shows no evidence of lift increase due to this motion. Only one case shows a significant difference, but this difference is present in the upstroke which is not the focus of this research and thereby less well modeled. Four other configurations show no significant difference. It is not possible to conclude from these results that the LEF motion has no influence on bat flight performance, but it suggests that the LEF does not increase the lift production, especially during the downstroke. It still remains possible that the LEF is used by bats to control flight and the LEV stability. Both will need a more complicated motion than used in this study. The LEF motion might even be part of a feed back system in these cases. Another possibility is that the decrease in α_{eff} due to pitch down LEF deflection nullifies the effect of increased camber. This would be an interesting subject for further research.

9.2 Onwing measurements

The onwing aerodynamics are analyzed in two different cases, one with a variable bat inspired α_{eff} and one with a constant α_{eff}. Both over a U_{eq} range from 1 to 7 m/s. In both cases, the measured α_{eff} was lower than desired, most likely to be caused by deformations in the wing due to aerodynamic forces, which are not accounted for in the simulation. Despite this lower α_{eff}, the two cases can still be used to give information about the vortex dynamics of the LEV.

Vortex dynamics The test sequence with variable α_{eff} represents a steady flight of bats and shows no LEVs at high speeds and a strong stable attached LEV at low speeds (figure 8.14b and 8.14c, respectively). This increase in strength of the LEV structure (c_Γ) is primarily due to an increase in α_{eff} with decreasing flight speed (figure 8.15B). The constant α_{eff} sequence showed that, throughout the complete flight speed range, it is possible to generate a LEV by operating at a high enough α_{eff}, and that c_Γ stays constant at constant α_{eff} throughout the complete measured flight speed range which increases the evidence of a relation between α_{eff} and c_Γ. In contrast to c_Γ, the size of the LEV (S_ω) remains increasing for increasing U_{eq} for the constant α_{eff} sequence and is thus not α_{eff} dependent. The increase in size of the LEV can be explained by a decrease in St_{loc} (figure 8.16C). No evidence was found for a relation between c_Γ or S_ω and Re_{loc} or Ro_{loc}.

Relevance for bats Based on lift coefficient estimates for flying *Leptonycteris yerbabuenae* (Muijres et al., 2011) an enhanced lift mechanism, such as a LEV, can be expected at low flight speeds ($C_{L,max}$>1.6 for U_{eq}<4 m/s), but not at high flight speeds ($C_{L,max}$<1.6 for U_{eq}>4 m/s) (Laitone, 1997). This corresponds well with the results obtained in the present study (figure 8.14c and 8.14a, respectively). Also, the LEV structure found at U_{eq}=1 m/s (figure 8.14c) is similar to that found in the smaller species *Glossophaga soricina* bats (Muijres et al., 2008).

LEVs can enhance C_L, but this comes with a penalty of increased drag. Therefore, we can assume that bats use LEVs at low flight speeds to generate enough lift for weight support. At high flight speeds the LEV is not required, and bats use the energetically more efficient attached flow at low α_{eff}. The increased sensitivity of the wing membrane near the trailing edge (Chadha et al., 2011) could be used to sense the difference between an attached LEV and a separated flow, which makes it possible for the bat to adjust the α_{eff} to an optimal position for different flight tasks.

Still bats are expected to be able to generate LEVs at high flight speeds by increasing α_{eff}, but it comes at a price, though, since the LEV tends to burst at high speeds, resulting in completely separated flow and high drag (figure 8.14d to 8.14f). Thus, LEVs could be used by bats throughout the complete natural flight speed range in high load maneuvers such as sharp turns.

Relevance for MAVs For the design of MAVs the fact that one single parameter as the body angle and thereby the stroke plane angle has so much influence on the flow field and possibly the resulting flight forces is very interesting . The almost constant circulation coefficient around 50 degrees α_{eff} at variable U_{eq} indicates that there is little influence of LEV bursting on the lift production, which makes it possible to use the high α_{eff} both at low and high speeds. Although, lift enhancement by using LEVs will be less efficient at high speeds due to the increased drag of LEV bursting.

Concluding remarks Thus, much information can be gathered with the use of a bat inspired flapper such as the RoBat, although the kinematics must be simplified. Also both bats and MAVs can greatly extend their flight envelope through controlling LEV production by changing their body and stroke plane angle, without the necessity to change any other wing flapping kinematics parameters.

Bibliography

(2012, February). Applied aerodynamics: A digital textbook. URL: http://www.desktop.aero/appliedaero/airfoils1/tatresults.html.

(2012, February). Conventional engineering materials. URL: http://ashwintooldesigner.blogspot.com/2009/03/conventional-engineering-materials.html.

Adrian, R., K. Christensen, and Z. Lui (2000). Analysis and interpretation of instantaneous turbulent velocity fields. *Experiments in Fluids 29*, 275–290.

Aldridge, H. D. J. N. (1986). Kinematics and aerodynamics of the greater horseshoe bat, rhinolophus ferrumequinum, in horizontal flight at various flight speeds. *The Journal of Experimental Biology 126*, 479–497.

Aldridge, H. D. J. N. (1987). Body accelerations during the wingbeat in six bat species: the function of the upstroke in thrust generation. *The Journal of Experimental Biology 130*, 275–293.

Anderson, J. D. (2001). *Fundamentals of Aerodynamics*. McGraw-Hill.

Berg van den, C. and C. P. Ellington (1997, mar). The three-dimensional leading-edge vortex of a 'hovering' model hawkmoth. *Philosophical Transactions of the Royal Society B: Biological Sciences 352*, 329–340.

Birch, J. M. and M. H. Dickinson (2001). Spanwise flow and the attachment of the leading-edge vortex on insects wings. *Nature 412*, 729–733.

Bunget, G. (2010). *BATMAV - A bio-inspired micro-aerial vehicle for flapping flight*. Ph. D. thesis, North Carolina Stat University.

Bunget, G. (2012, February). URL: https://sites.google.com/site/gheorghebunget/research/batmav.

Busse von, R. (2011). *The trinity of energy conversion - kinematics, aerodynamics and energetics of the lesser long-nosed bat (Leptonycteris yerbabuenae)*. Ph. D. thesis, Humboldt University Berlin.

Chadha, M., M. C. F., and S. J. Sterbing-D'Angelo (2011). Organization of the primary somatosensory cortex and wing representation in the big brown bat, eptesicus fuscu. *Journal of Comparative Physiology 197*, 89–96.

Dickinson, M. H., F.-O. Lehmann, and S. P. Sane (1999). Wing rotation and the aerodynamic basis of insect flight. *Science 284*, 1954–1960.

dpp pultrusion (2011). *Specifications standard product range, January 2011*. dpp pultrusion.

Dumont, E. R. (2010, jul). Bone density and the lightweight skeletons of birds. *Proceedings of the Royal Society B: Biological Sciences 277*(1691), 2193–2198.

Ellington, C. P., C. Berg van den, A. P. Willmott, and A. L. Thomas (1996, dec). Leading-edge vortices in insect flight. *Nature 384*, 626–630.

Hedenstrom, A., C. L. Johansson, and R. G. Spedding (2009). Bird or bat: comparing airframe design and flight performance. *Bioinspiration & Biomimetics 4*, 015001.

Hedenstrom, A., L. C. Johansson, v. B. R. Wolf, M., Y. Winter, and G. R. Spedding (2007). Bat flight generates complex aerodynamic tracks. *Science 316*, 894.

Hedenstrom, A., L. C. Johansson, v. B. R. Wolf, M., Y. Winter, and G. R. Spedding (2009). High-speed stereo dpiv measurement of wakes of two bat species flying freely in a wind tunnel. *Experiments in Fluids 46*, 923–932.

Hedrick, T. L. (2008). Software techniques for two- and three-dimensional kinematic measurements of biological and biomimetic systems. *Bioinspiration & Biomimetics 3*, 6.

Hubel, T. Y., N. I. Hristov, S. M. Swartz, and K. S. Breuer (2009). Time-resolved wake structure and kinematics of bat flight. *Experiments in Fluids 46*, 933–943.

Hubel, T. Y., D. K. Riskin, S. M. Swartz, and K. S. Breuer (2010). Wake structure and wing kinematics: the flight of the lesser dog-faced fruit bat, cynopterus brachyotis. *The Journal of Experimental Biology 213*, 3427–3440.

Hubel, T. Y. and C. Tropea (2008). Experimental investigation of a flapping wing model. *The Journal of Experimental Biology 46*, 945–961.

Hubel, T. Y. and C. Tropea (2010). The importance of leading edge vortices under simplified flapping flight conditions at the size scale of birds. *The Journal of Experimental Biology 213*, 1930–1939.

Johansson, L., W. Marta, R. Busse von, Y. Winter, G. R. Spedding, and A. Hedenstrom (2008). The near and far wake of pallas' long tongued bat (glossophaga soricina). *The Journal of Experimental Biology 211*, 2909–2918.

Koekkoek, G., F. T. Muijres, C. L. Johansson, M. Stuiver, B. W. Oudheusden van, and A. Heddenstrom (2012). Stroke plane angle controls leading edge vortex in a bat-inspired flapper. *Comptes Rendus Mecanique 340*, 95–106.

Laitone, E. V. (1997). Wind tunnel tests of wings at reynolds numbers below 70 00. *Experiments in Fluids 23*, 405–409.

Lentink, D. (2008). *Exploring the biofluiddynamics of swimming and flight.* Ph. D. thesis, Wageningen.

Lentink, D. and M. H. Dickinson (2009). Rotational accelerations stabilize leading edge vortices on revolving fly wings. *The Journal of Experimental Biology 212*, 2705–2719.

Maxworthy, T. (2007). The formation and maintenance of a leading-edge vortex during the forward motion of an animal wing. *Journal of Fluid Mechanics 587*, 471–475.

Muijres, F., M. Bowlin, C. L. Johansson, and A. Heddenstrom (2012). Vortex wake, downwash distribution, aerodynamic performance and wingbeat kinematics in slow-flying pied flycatchers. *Journal of the Royal Society Interface 9*, 292–303.

Muijres, F., L. Johansson, R. Barfield, M. Wolf, G. Spedding, and A. Heddenstrom (2008, feb). Leading-edge vortex improves lift in slow-flying bats. *Science 319*, 1250.

Muijres, F. T., L. C. Johansson, Y. Winter, and Hed (2011). Comparative aerodynamic performance of flapping flight in two bat species using time-resolved wake visualization. *Journal of the Royal Society Interface*.

Norberg, U. M. (1976a). Aerodynamics , kinematics and energetic of horizontal flapping flight in the long-eared bat plecotus auritus. *The Journal of Experimental Biology 65*, 179–212.

Norberg, U. M. (1976b). Aerodynamics of hovering flight in the long-eared bat plecotus auritus. *The Journal of Experimental Biology 65*, 459–470.

Pennycuick, C. J., T. Alerstam, and A. Heddenstrom (1997). A new low-turbulence wind tunnel for bird flight experiments at lund university, sweden. *The Journal of Experimental Biology 200*, 1441–1449.

Riskin, D. K., D. J. Willis, J. Iriarte-DÃaz, T. L. Hedrick, M. Kostandov, J. Chen, D. H. Laidlaw, K. S. Breuer, and S. M. Swartz (2008). Quantifying the complexity of bat wing kinematics. *Journal of Theoretical Biology 254*, 604–615.

Sane (2003). The aerodynamics of insect flight. *The Journal of Experimental Biology 206*, 4191–4208.

Scarano, F. (2007, apr). Experimental aerodynamics. Unpublished.

Spedding, G. R., M. Rosen, and A. Hedenstrom (2003). A family of vortex wakes generated by a thrush nightingale in free flight in a wind tunnel over its natural range of flight speeds. *The Journal of Experimental Biology 206*, 2313–2344.

Stuiver, M. (2011). Bats in gliding flight. Master's thesis, Delft University of Technology.

Swartz, S. M., H. Groves, M.S.and Kim, and W. Walsh (1996). Mechanical properties of bat wing membrane skin. *Journal of Zoology 239*, 357–378.

Swartz, S. M. and K. M. Middleton (2008). Biomechanics of the bat limb skeleton: scaling, material properties and mechanics. *Cells Tissues Organs 187*, 59–84.

Tian, X., J. Iriarte-DÃaz, K. Middleton, R. Galvao, E. Israeli, A. Roemer, A. Sullivan, A. Song, S. Swartz, and K. Breuer (2006). Direct measurements of the kinematics and dynamics of bat flight. *Bioinspiration & Biomimetics 1*, S10–S18.

Weis-Fogh, T. (1973). Quick estimates of flight fitness in hovering animals, including novel mechanisms for lift production. *The Journal of Experimental Biology 59*, 169–230.

Wolf, M., C. L. Johansson, R. Busse von, Y. Winter, and A. Hedenstrom (2009). Kinematics of flight and the relation to the vortex wake of a pallas' long tongued bat (glossophaga soricina). *The Journal of Experimental Biology 213*, 2142–2153.

APPENDIX A

Design option tree

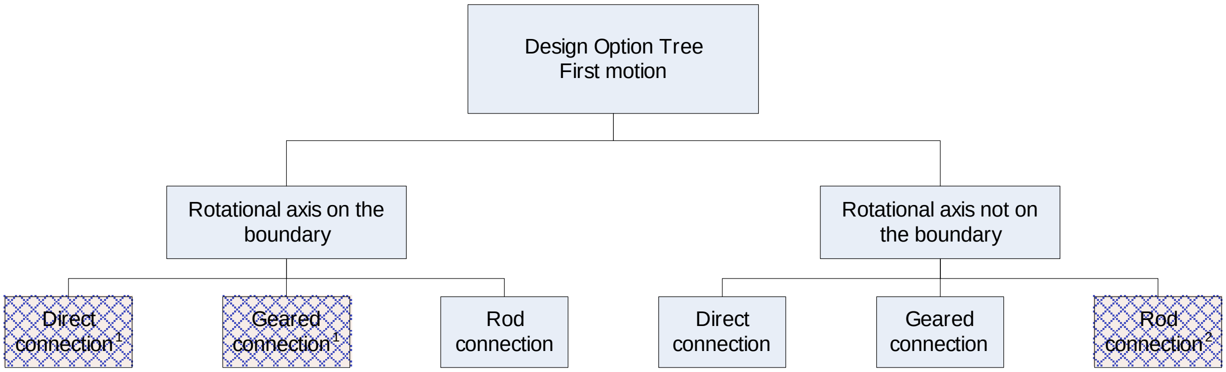

Figure A.1 – Design option tree for the flapping motion. [1]Not possible, [2]Better option when the rotational axis is located on the wind tunnel boundary.

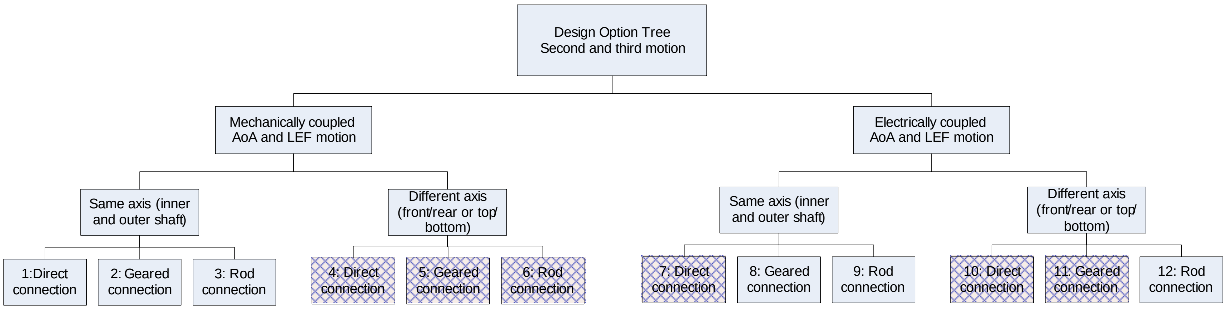

Figure A.2 – Design option tree for the pitching and LEF rotation motions

APPENDIX B

Design options part A: flapping motion

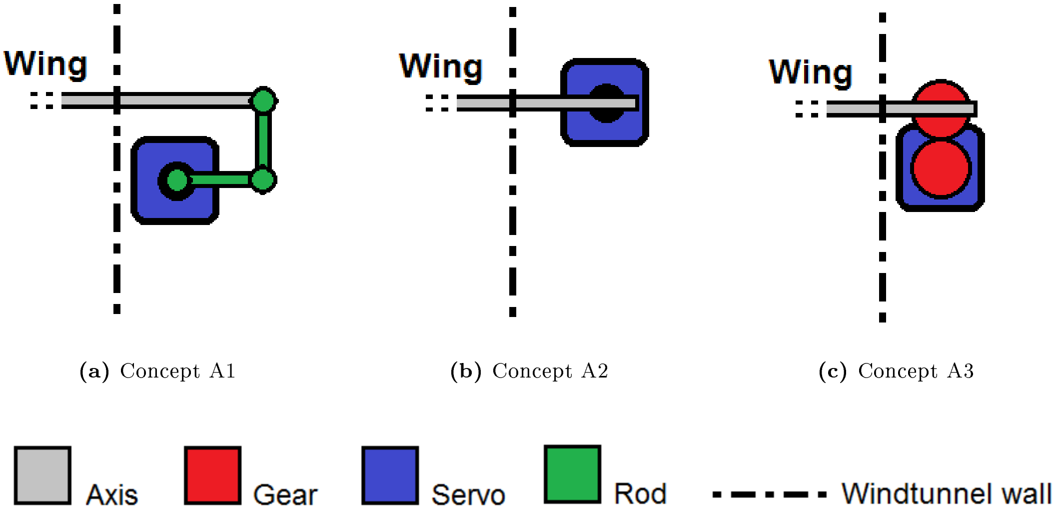

(a) Concept A1 **(b)** Concept A2 **(c)** Concept A3

Figure B.1 – Sketches of the three possible concepts for the flapping motion

APPENDIX C

Design options part B: pitching and LEF rotation

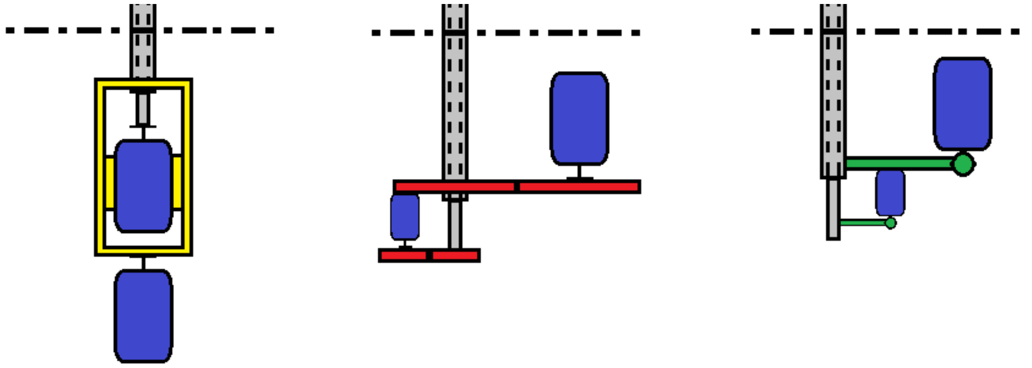

(a) Concept B1 **(b)** Concept B2 **(c)** Concept B3

⬜ Axis 🟥 Gear 🟦 Servo 🟨 Structure 🟩 Rod

- - - Windtunnel wall

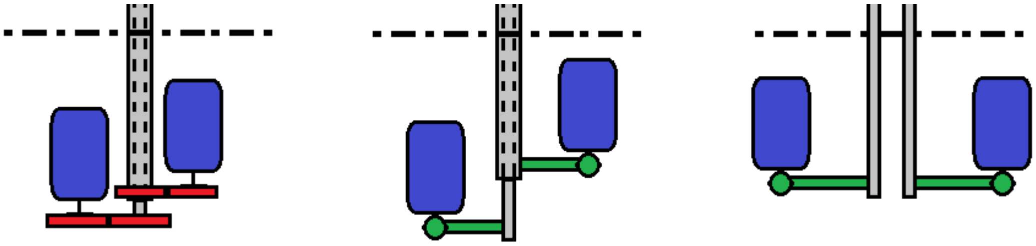

(e) Concept B8 **(f)** Concept B9 **(g)** Concept B12

Figure C.1 – Sketches of the six possible concepts for the pitching and LEF rotation

APPENDIX D

LEF and no LEF motion compared using the force production

	Beta = 12			Beta = 17			Beta = 22		
	LEF on	LEF off	p-value	LEF on	LEF off	p-value	LEF on	LEF off	p-value
U=2.2				48.2	51.9	0.21			
U=2.6	-14.4	-14.5	0.97	**62.2**	**72.3**	**0.02**	148	148	0.92
U=2.9				71.7	83.4	0.10			

Table D.1 – Force production [mN] for all three vortices together

	Beta = 12			Beta = 17			Beta = 22		
	LEF on	LEF off	p-value	LEF on	LEF off	p-value	LEF on	LEF off	p-value
U=2.2				0114	117	0.33			
U=2.6	92.2	90.3	0.39	132	131	0.73	170	169	0.82
U=2.9				**132**	**139**	**0.04**			

Table D.2 – Force production [mN] for the tip vortex

	Beta = 12			Beta = 17			Beta = 22		
	LEF on	LEF off	p-value	LEF on	LEF off	p-value	LEF on	LEF off	p-value
U=2.2				18.2	17.9	0.88			
U=2.6	**21.6**	**25.5**	**0.02**	25.8	25.4	0.81	35.3	32.4	0.15
U=2.9				35.1	38.3	0.11			

Table D.3 – Force production [mN] for the inward vortex of the dipole vortex structure

	Beta = 12			Beta = 17			Beta = 22		
	LEF on	LEF off	p-value	LEF on	LEF off	p-value	LEF on	LEF off	p-value
U=2.2				-84.4	-83.0	0.33			
U=2.6	-128	-130	0.52	**-95.7**	**-83.8**	**0.0006**	-57.1	-53.6	0.05
U=2.9				-95.0	-94.0	0.75			

Table D.4 – Force production [mN] for the outward vortex of the dipole vortex structure

APPENDIX E

Raw Data Examples

Kinematic camera images

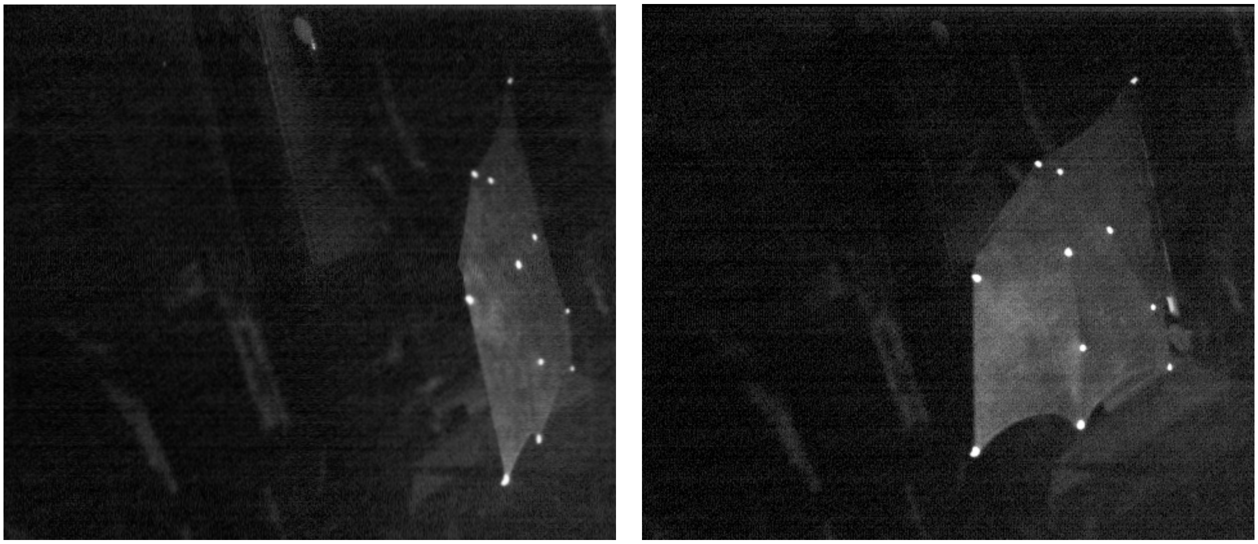

(a) Frame 0 **(b)** Frame 17

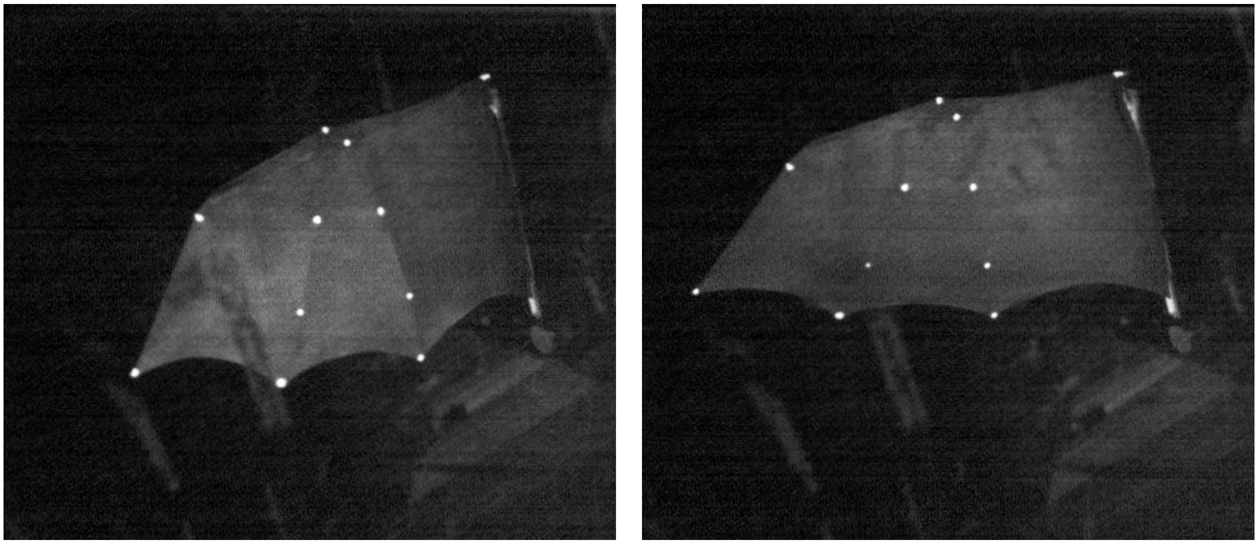

(c) Frame 33 **(d)** Frame 50

Figure E.1 – Four frames of one kinematic camera at frame number 0, 17, 33, 50 from total range of 0 to 100 starting at the upper most point at frame 0 ($U_\infty = 2.5\,\mathrm{m/s}$, $\beta = 83°$).

Wake PIV camera images

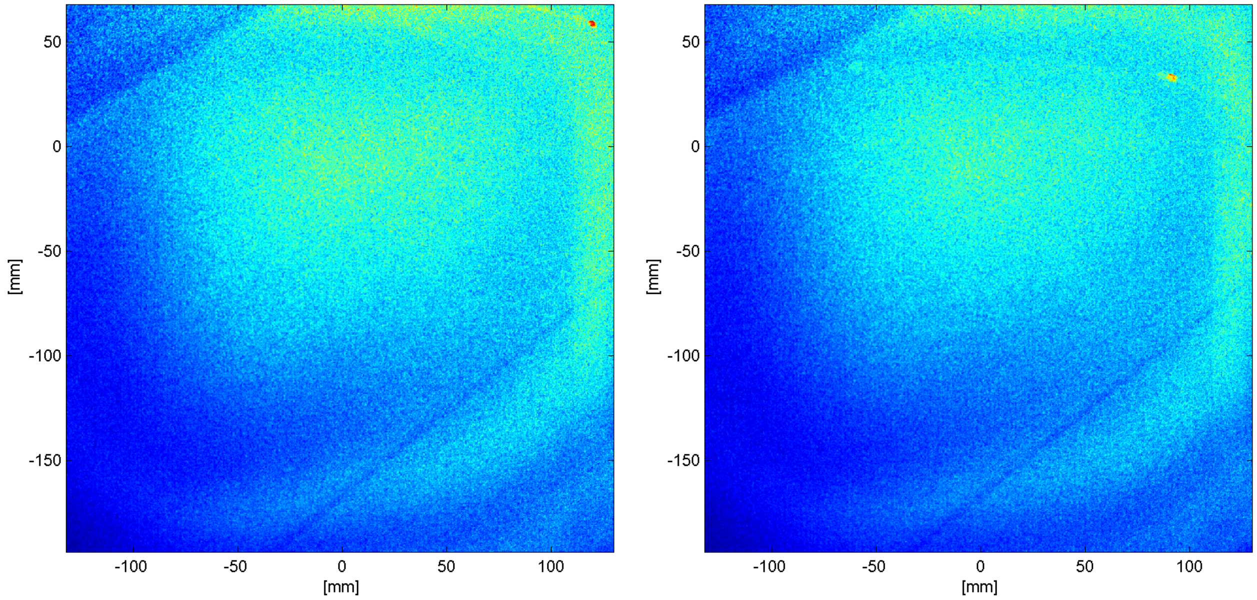

(a) Frame 10

(b) Frame 20

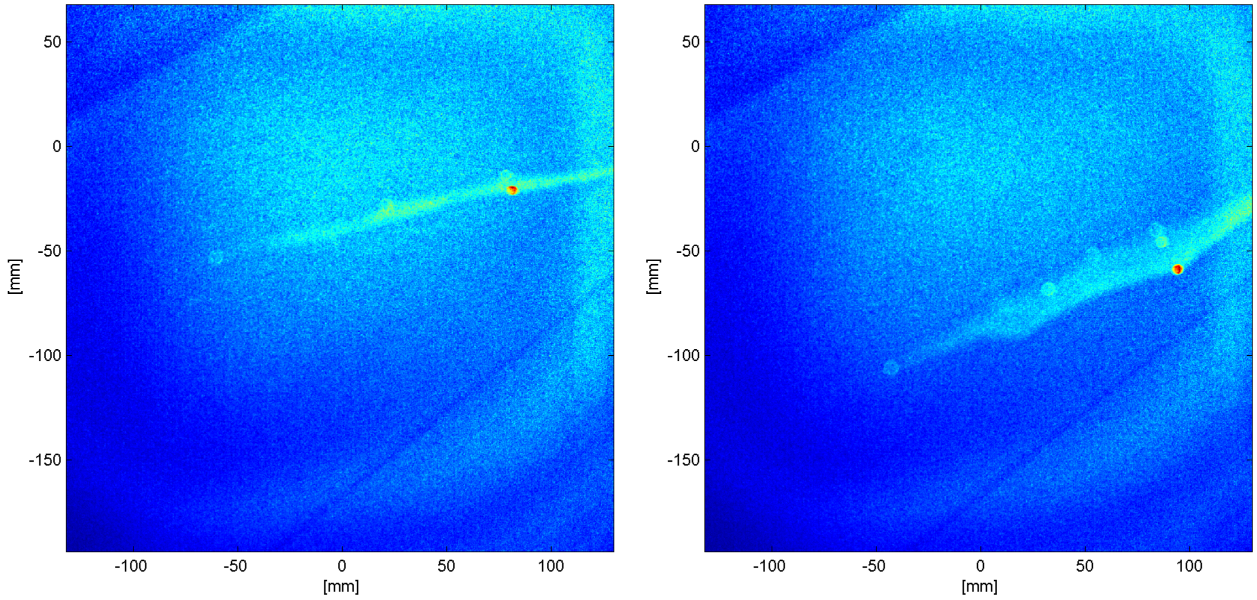

(c) Frame 30

(d) Frame 40

Figure E.2 – Four frames of the lower PIV camera at frame number 10, 20, 30 and 40 from total range of 0 to 80 starting at the upper most point at frame 0 ($U_\infty = 2.5\,\mathrm{m/s}$, $\beta = 83^\circ$).

Onwing PIV camera images

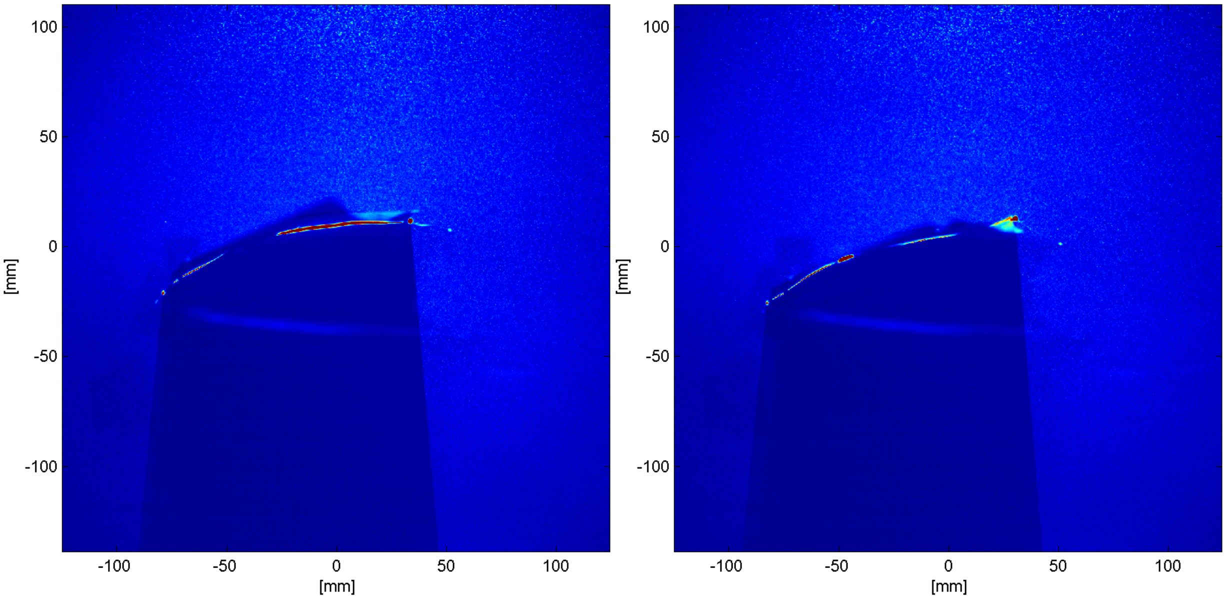

(a) frame 24 **(b)** frame 25

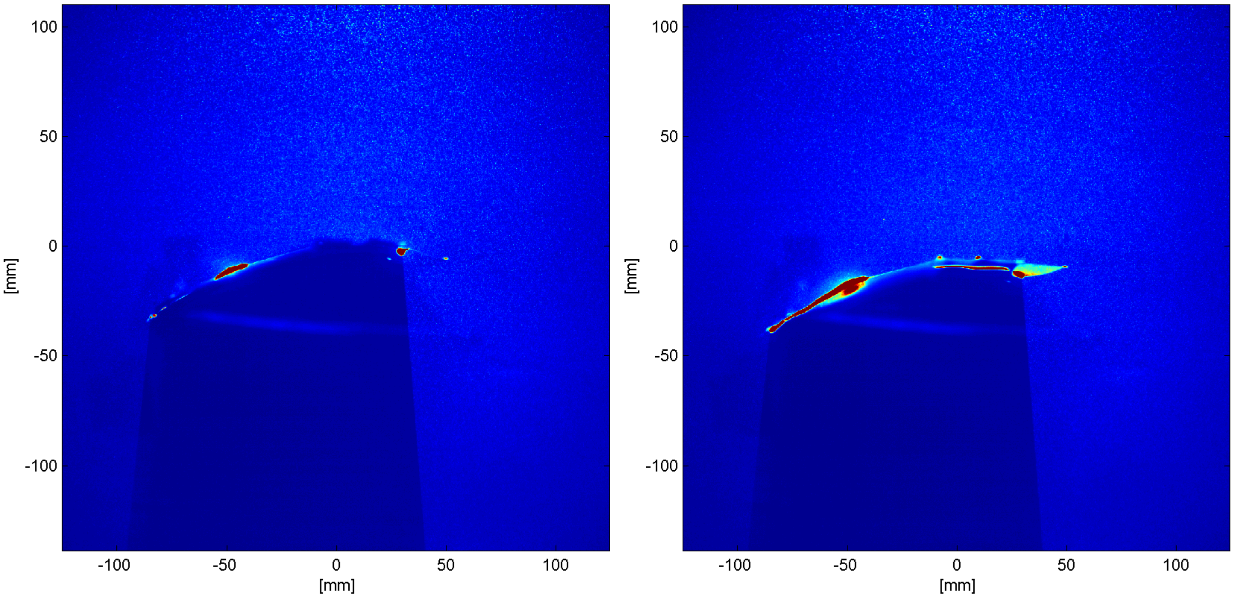

(c) frame 26 **(d)** frame 27

Figure E.3 – Four frames of one PIV camera at frame number 24 to 27 from total range of 0 to 80 starting at the upper most point at frame 0 ($U_\infty = 2.5^{\mathrm{m}}/_{\mathrm{s}}$, $\beta = 83°$). Used frame for onwing postprocessing is frame 26.

APPENDIX F

Stroke plane angle controls leading edge vortex in a bat-inspired flapper

Published in *Comptes Rendus Mecanique* 340, 95-106

C. R. Mecanique 340 (2012) 95–106

Contents lists available at SciVerse ScienceDirect

Comptes Rendus Mecanique

www.sciencedirect.com

Biomimetic flow control

Stroke plane angle controls leading edge vortex in a bat-inspired flapper

Gide Koekkoek [a,b], Florian T. Muijres [a], L. Christoffer Johansson [a], Melanie Stuiver [a,b], Bas W. van Oudheusden [b], Anders Hedenström [a,*]

[a] *Lund University, Department of Biology, Ecology Building, SE-223 62 Lund, Sweden*
[b] *Delft University of Technology, Department of Aerospace Engineering, P.O. Box 5058, 2600 GB Delft, The Netherlands*

ARTICLE INFO

Keywords:
Aerodynamics
Bat flight
Bio-inspired robot
Leading edge vortex
Micro air vehicle

ABSTRACT

The present interest in micro air vehicles has given the research on bat flight a new impulse. With the use of high speed cameras and improved PIV techniques, the kinematics and aerodynamics of bats have been studied in great detail. A robotic flapper makes it possible to do measurements by systematically changing only one parameter at a time and investigate the parameter space outside the natural flight envelope of bats without risking animal safety. For this study, a robotic flapper (RoBat), inspired by *Leptonycteris yerbabuenae* was developed and tested over the speed range 1–7 m/s, with variable maximum angles of attacks ($\text{AoA}_{\max} = 55°$ and $15°$, respectively) and constant $\text{AoA}_{\max} = 55°$. These measurements show the presence of a leading edge vortex (LEV) for low speeds and a fully attached flow for high speeds at low $\text{AoA}_{\max}$, which is in line with natural bat flight. A LEV occurs for $\text{AoA}_{\max} = 55°$ throughout the complete flight speed range, and throughout which the LEV circulation coefficient remains rather constant. This implies that bats and micro air vehicles could use LEVs for high load maneuvers also at relatively high flight speeds. However, at high flight speeds the LEV bursts, which causes increased drag, most likely due to a decrease in Strouhal number.

1. Introduction

The present interest in flapping micro air vehicles (MAV) has resulted in a renewed interest in animal flight (e.g. Lentink and Biewener [1]). The maneuverability and hover capability of animals is still unrivalled by MAVs, suggesting that animal flight can still act as a source of inspiration for future MAV designs. Bats are of particular interest because of their impressive maneuverability and similarity to MAVs regarding size and often also airframe design, consisting of flexible wing membranes spanned between stiffeners (e.g. www.delfly.nl).

Recent studies of kinematics and aerodynamics of bat flight have considerable increased our understanding of bat flight (Hedenström et al. [2,3], von Busse [4], Tian et al. [5], Johansson et al. [6], Muijres et al. [7], Hubel et al. [8,9], Wolf et al. [10], Muijres et al. [11], Lindhe-Norberg and Winter [12], Muijres et al. [13]). With the use of high speed cameras the kinematics of bats flying in a wind tunnel are analyzed and show that the motion of the wings contain next to a flapping, also a yawing, contracting and pitching component (Wolf et al. [10], von Busse [4]). In addition, the camber, angle of attack (AoA) and orientation of the leading edge flap (LEF, part of the wing membrane controlled by the thumb and index finger, Propatagium and Dactylopatagium brevis) all show a substantial variation indicating an active control of the flow (von Busse [4]).

---

[*] Corresponding author.
E-mail address: anders.hedenstrom@biol.lu.se (A. Hedenström).

1631-0721/$ – see front matter
doi:10.1016/j.crme.2011.11.013

The airflow structure close to the top surface of the wing of *G. soricina* bats has been measured using Particle Image Velocimetry (PIV) in imaging planes parallel to the flight direction (Muijres et al. [7]), which revealed the presence of an attached leading edge vortex (LEV) that produced about 40% of the lift during slow flight (1 m/s). The LEV is present at mid downstroke over the complete wing span, with the highest strength near the wingtip. The LEV is stably attached at least up to mid downstroke, although in steady conditions the high angle of attack (around 51 degrees) should cause full separation (Laitone [14]).

It is still largely unknown how bats control the attached LEV, such as the relation between the kinematics and LEV stability, and whether the control mechanism is due to passive deformation or active control of the wing shape. It has recently been shown that bats have sensory hairs on the top surface of the wing that are specialized in sensing reversed airflow (Chadha et al. [15], Sterbing-Dangelo et al. [16]). Thus, bats should have the ability to sense LEV separation, which indicates that LEV control in bats could potentially at least be partly active.

The difficulty with doing measurements with live animals is that a parametric study is very hard or even impossible to achieve and animal safety gives restrictions. For these reasons computational approaches are ways around these problems (e.g. Soueid et al. [17], Sudhakar and Vengadesan [18]). Another solution could be to use a robotic flapper that will not have these limitations and thereby could give new information about bat flight and provides the possibility to explore aerodynamic regions outside the natural flight envelope of bats. Robotic models inspired by a fruit fly (e.g. Dickinson et al. [19]) and a goose (Hubel and Tropea [20,21]) have already proven to be interesting study objects, while to the best of our knowledge so far no aerodynamic data have been published derived from a bat-inspired flapping model. One very promising bat-inspired model is the BATMAV (Bunget [22]), but no aerodynamic data have yet been published.

In this article a robotic bat-inspired flapper (RoBat) is used to mimic flight kinematics of *Leptonycteris yerbabuenae* (*L. yerbabuenae*) at 5 m/s flight speed as closely as possible. The aim was to determine how the LEV can be controlled using simple adjustments in the stroke plane angle and give information concerning the AoA and Strouhal number dependencies of separation and LEV in bat-inspired wings. We use two test cases, one where the stroke plane angle is changed with flight speed resulting in similar AoAs as measured in real bat flight, and a second case where the AoA at mid downstroke (AoA_{max}) is kept constant. Both cases were studied across a flight speed range of 1 to 7 m/s. In order to evaluate the utility of a mechanical flapper we focused on one important aerodynamic feature of bat flight, i.e. the LEV (Muijres et al. [7]). A more complete study of the aerodynamics of this bat flapper is left for a future project.

2. RoBat wing design

The RoBat design is based on the geometry and kinematics of the *L. yerbabuenae* bat (von Busse [4]). *L. yerbabuenae* is a medium sized (20–25 g) tropical nectar feeding bat. It is well adapted to hovering flight, which it does when feeding from flowers. Since *L. yerbabuenae* is a migratory species and travels up to 100 km every night from roost to feeding patches, it can be assumed well adapted to efficient cruising flight (Horner et al. [23]). Thus, *L. yerbabuenae* can operate efficiently throughout a wide velocity range from hovering (0 m/s flight) up to a flight speed of at least 8 m/s (Sahley et al. [24], Horner et al. [23]).

Along this velocity range, the wingbeat frequency of *L. yerbabuenae* ranges from about 13 Hz (hovering) to about 9 Hz (fast forward flight). To be able to reach these kinds of frequencies with a mechanical flapper, powerful and very precise actuators are required. Also vibrations, especially around the eigenfrequencies can be expected to cause problems. To reduce the flapping frequency of the mechanical flapper, the model was designed as an isometric scale of 1:2 of an *L. yerbabuenae* wing. Using this scaling will decrease the frequency with a factor of 4 (see below). Two other advantages of scaling up the model are that a larger model is easier to produce and that more measurements per wingbeat will increase the time resolution. When scaling a wing geometrically, also the aerodynamic and mechanical parameters need to be scaled appropriately.

2.1. Scaling of the RoBat wing

For aerodynamic similarity between the bat wing and the scaled model both the Reynolds number (Re) and Strouhal number (St) should be kept constant. Re is a measure of the relative inertial and viscous forces produced by a wing with characteristic length scale l, defined as

$$Re = \frac{U_{\infty,eff}\, l}{\upsilon} \tag{1}$$

where $U_{\infty,eff}$ is the effective velocity at which the wing operates (Fig. 1), defined by

$$U_{\infty,eff} = \sqrt{(U_\infty + U_{flap,x})^2 + U_{flap,z}^2} \tag{2}$$

υ is the kinematic viscosity of air, $U_{flap,x}$ the horizontal and $U_{flap,z}$ the vertical component of U_{flap}, i.e. the wing flapping velocity in the wind tunnel frame of reference. See Fig. 4 for the definition of the coordinate system. If Re is kept constant during scaling, then

$$U_{\infty,eff} \propto l^{-1} \tag{3}$$

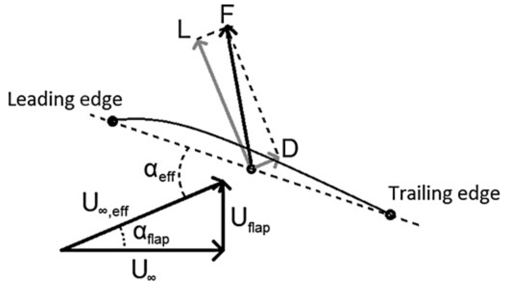

Fig. 1. Cross section of the flapping RoBat wing. Definition of forces: aerodynamic force F, with lift L and drag D components. Definition of velocities: free stream velocity U_∞, effective velocity $U_{\infty,eff}$ and flap velocity U_{flap}. Definition of angles: inflow angle (α_{flap}) and angle of attack (α).

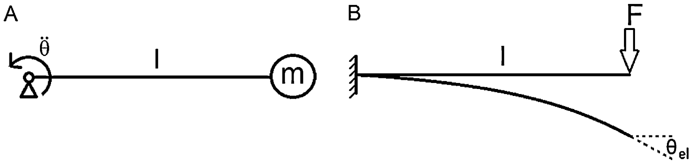

Fig. 2. (A) point mass with mass m at distance l from the rotation point with angular acceleration ($\ddot{\theta}$). (B) Clamped beam with force F on length l and elastic deflection angle θ_{el}.

Since, for similarity the angle of incidence, α_{flap}, should be kept constant (Fig. 1), the free stream velocity U_∞ scales linearly with $U_{\infty,eff}$. Thus,

$$U_\infty = \cos(\alpha_{flap}) \cdot U_{\infty,eff} \quad \Rightarrow \quad U_\infty \propto l^{-1} \tag{4}$$

For our model this means $U_{\infty,model} = U_{\infty,bat}/2$. From now on, when referring to velocities we will use the equivalent air speed

$$U_{eq} = U_{bat} = 2U_{model} \tag{5}$$

Keeping *Re* constant has the consequence that the forces are not affected by the scaling of the model

$$L = \frac{1}{2} C_L \rho_{air} S U_{\infty,eff}^2 \propto l^2 \left(l^{-1}\right)^2 = \text{constant} \tag{6}$$

where C_L is the lift coefficient, ρ_{air} is the density of air and S is the surface of the wing.

St is a measure of the relative importance of unsteady aerodynamic effects for flapping wings, and defined here as

$$St = \frac{fl}{U_{\infty,eff}} \tag{7}$$

where f is the flapping frequency. To keep *St* constant during scaling, f should scale with l^{-2}

$$f \propto \frac{U_{\infty,eff}}{l} \propto l^{-2} \tag{8}$$

Thus, for our model $f_{model} = f_{bat}/4$. To be able to model wing deformations correctly, the ratio between fluid dynamic forces and mechanical forces of the wing (inertia and elastic forces) should be kept constant. L is unaffected by the scaling (Eq. (6)), thus the mechanical forces should be kept constant too. Assuming, for scaling purposes, a simplified mechanical model, with a concentrated mass m representing the wing and a total force F, both located at a distance l from the hinge ('shoulder') point (Fig. 2). The mechanical forces can be modeled as

$$F_{elastic} \propto \theta_{el} = \frac{Fl^2}{2EI} = \text{constant}, \quad \text{and} \tag{9}$$

$$F_{inertia} = ma = m\ddot{\theta}l \propto \rho_{wing} d^2 l \ddot{\theta} l = \text{constant} \tag{10}$$

where $F_{elastic}$ is the elastic force, $F_{inertia}$ is the inertial force, $\ddot{\theta}$ is the angular acceleration, ρ_{wing} is the density of the wing skeletal bones, d is the diameter of the wing bones, θ_{el} is the elastic deformation angle, E is Young's modulus and I is the area moment of inertia. Note that, for simplicity, the mass of the membrane is neglected.

When scaling a periodic flapping motion with the angular amplitude kept constant, the angular acceleration scales with f^2, which gives

$$\ddot{\theta} \propto f^2 \propto l^{-4} \tag{11}$$

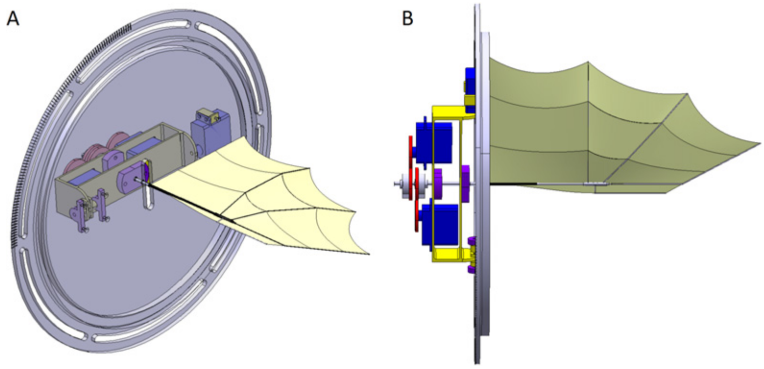

Fig. 3. The RoBat wing, drive system and mounting plate. The drive system components are cogwheels (red), servos (blue), support structure (yellow), bearings (purple) and axes (grey). (For interpretation of the references to color in this figure legend, the reader is referred to the web version of this article.)

By substituting Eq. (11) into Eq. (10) the scaling of $\rho_{wing}d^2$ can be determined as

$$\rho_{wing}d^2 \propto \frac{1}{l\ddot{\theta}l} \propto \frac{1}{ll^{-4}l} \propto l^2 \tag{12}$$

Using a circular cross section gives the scaling of the second moment of inertia as

$$I = \frac{\pi d^4}{64} \propto d^4 \tag{13}$$

Combined with Eq. (9) this gives the scaling for Ed^4 as

$$Ed^4 \propto Fl^2 \propto l^2 \tag{14}$$

Both Eqs. (12) and (14) must now be used to select the material and dimensions of the model wing. They can only be fulfilled when the density, Young's modulus or both are changed with respect to the values for a real bat. In practice ρ_{wing} and E cannot be changed independently due to the limited range of available materials. Therefore, we made a trade-off between ρ_{wing}, E, and d for our model wing as discussed below.

2.2. The RoBat wing geometry and materials

A bat wing consists of compliant skin membranes spanned between stiffeners consisting of elongated hand digits (Swartz et al. [25]). The membrane is anisotropic and varies in thickness and stiffness over the wing. There are also muscles running through the membrane that make active control of the membrane stiffness possible (Swartz et al. [26]).

The bat wing membranes are modeled by a 0.25 mm thick latex sheet, and the stiffeners are constructed using carbon reinforced epoxy (63% fiber volume) rods. These rods give an average value of Ed^4 that is a factor 30 higher than the average value in bats and ρd^2 that is 10% lower than in bats (Table 2, Swartz and Middleton [27]). This means that the wing is designed relatively stiff with respect to the real bat, while the mass of the RoBat bones is comparable with that of real bats. The difference in stiffness is a result of the limited choice in useful building materials. Since bone stiffness varies much throughout a bat wing (Swartz and Middleton [27]) an exact match in stiffness is almost impossible, and therefore we assumed it was safer to design the RoBat wing too stiff rather than too compliant.

The dimensions of the model wing were based on the wing geometry *L. yerbabuenae* at mid downstroke, estimated from kinematics measurements of *L. yerbabuenae* flying at 5 m/s in a wind tunnel (von Busse [4]). The first and second bat wing digits were combined into the LEF (Fig. 3).

2.3. The RoBat wing kinematics

Based on the wing kinematics of *L. yerbabuenae* (von Busse [4]), we decided to model three motions; a wing flapping motion, a wing pitching motion, and an LEF deflection motion. The flapping motion is the main motion for inducing U_{flap}. It is supplemented by the pitching motion to be able to regulate the AoA. The LEF rotation is added, since it is regarded as important for the control of profile shape in bat wings (von Busse [4]).

For each motion, a dedicated servo motor (Hitec HS-7940TH, 7.2 V) was used. The flapping motion is transferred from servo to wing through a direct connection, while for both the pitching motion and LEF deflection a cogwheel system was used (Fig. 3). The whole structure was connected to a circular aluminum plate placed in the wind tunnel sidewall, which can be rotated manually to adjust the stroke plane angle of the model (Fig. 3).

Table 1
Kinematic parameters used for the experimental measurements.

U_{eq} [m/s]	Required AoA_{max} [degree]	Stroke plane angle [degree]	Reynolds number Re_{tip} [–]	Strouhal number St_{tip} [–]
7	15	12	2.5E4	0.19
5	20	17	1.9E4	0.25
3	35	27	1.4E4	0.35
2	45	42	1.2E4	0.42
1	55	52	8.8E3	0.55
2	55	65	1.2E4	0.39
3	55	70	1.6E4	0.31
5	55	73	2.2E4	0.22
7	55	74	2.9E4	0.17

Table 2
Morphological data of *Leptonycteris yerbabuenae* and of the RoBat.

Measure	Unit	*L. yerbabuenae*	RoBat
Semispan	[m]	0.16	0.29
Wing area	[m^2]	0.016	0.058
Mean chord	[m]	0.047	0.10
Aspect ratio	[–]	7.0	5.6
Density bones	[kg/m^3]	2000*	1590
Young's modulus bones	[GPa]	20–23**	140
Radius bones	[mm]	1.4**	3
Young's modulus membrane	[MPa]	3–37***	1.5
Thickness membrane	[mm]	0.22–0.28***	0.25

* Dumont [33];
** Swartz and Middleton [27];
*** Swartz et al. [26].

The three motions described previously are optimized based on the kinematics data from *L. yerbabuenae* flying at 5 m/s (von Busse [4]). The kinematics of the LEF could be directly fitted with a sinusoidal motion (Fig. S1, see section Supplementary material), but because the flapping and pitching motions in real bat flight are not generated by two purely rotational motions, but instead by multiple hinges as well as wing deformations (Swartz et al. [25]), the flapping and pitching motions were optimized using the optimization scheme presented in Fig. S2.

Two aerodynamic parameters were used in the optimization, being AoA and inflow angle α_{flap} (Fig. 1). These variables were chosen because AoA primarily characterizes the aerodynamic structure and force production generated by a wing and inflow angle primarily characterizes the direction of the force vector F.

The computer model calculated the aerodynamic parameters (AoA and α_{flap}) using the given motions and geometry of the wing. Using the desired AoA (AoA_{ref}) as parameter for the pitching motion and $\alpha_{flap,ref}$ for the flapping motion the wing kinematics was thereby optimized. The resulting flapping and pitching motions for the model were then fitted with the sum of three sinusoidal motions, which could be generated by the servo motors (Fig. S3).

2.4. The measurement sequences

To be able to investigate the influence of AoA and *St* on the performance of flapping bat wings, two sets of measurements were done, both with the above described wing kinematics based on *L. yerbabuenae* at 5 m/s. Both sets of measurements were done throughout an equivalent flight speed range from 1 m/s to 7 m/s (increments of 1 m/s), see Table 1. In the first case the stroke plane of the flapper was adjusted so the maximum AoA within the wingbeat (AoA_{max}) was equal to that of *L. yerbabuenae* throughout the flight speed range ($\text{AoA}_{\text{max}} = 55°$ at 1 m/s to $\text{AoA}_{\text{max}} = 15°$ at 7 m/s), hereafter called the variable AoA_{max} case. In the second set of experiments the AoA_{max} was kept constant throughout the flight speed range ($\text{AoA}_{\text{max}} = 55°$, based on *L. yerbabuenae* at 1 m/s), hereafter called the constant AoA_{max} case. The stroke plane angles required to obtain the desired AoA_{max} were calculated using simplified trigonometry. Note that changing the stroke plane angle to optimize AoA_{max} will also change the pitching angle relative to the wind tunnel frame of reference.

The Reynolds number in Table 1 is calculated using Eqs. (1) and (2) based on the mean chord and mean flap velocity of the wing tip over the downstroke. The Strouhal number in Table 1 is calculated using Eqs. (2) and (7) based on the wing tip and the mean flap velocity of the wing tip over the downstroke.

3. Test set-up

For this study measurements were made in the Lund University closed loop, low turbulence and low speed, wind tunnel (Pennycuick et al. [28]). The model was attached to the wall of the wind tunnel test section that influences the velocity up to 3 cm and the turbulence of the airflow up to 10 cm from the wall at 10 m/s (Pennycuick et al. [28]), which is 10%

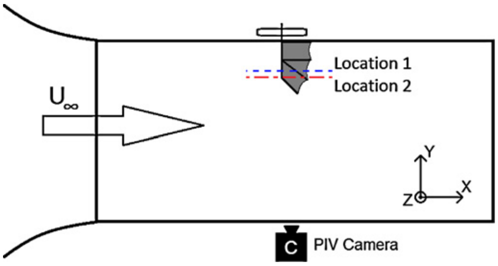

Fig. 4. Top view of the test section of the wind tunnel with the RoBat model, PIV camera, the free stream velocity vector (U_∞) and definition of the wind tunnel coordinate system.

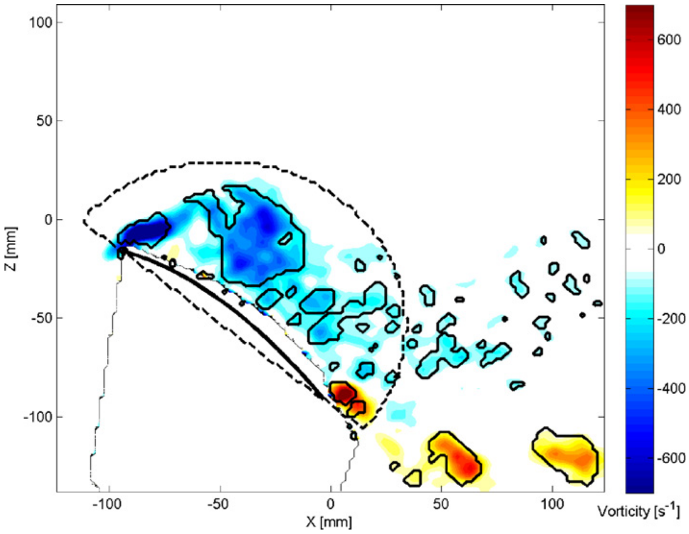

Fig. 5. Vorticity field around the flapping RoBat wing (AoA = 48° and $U_{eq} = 5.2$ m/s) with swirl strength contours (solid line) and semicircle domain (dashed line), within which the circulation is measured.

and 34% of the semi-span, respectively. The PIV system consisted of a 200 Hz 50 mJ Laser (Litron LPY732 series, Nd:YAG, 532 mm) for illumination of fog particles (1 μm diameter), a CMOS-camera (High-SpeedStar3; 1024 × 1024 pixels) and a frame grabber PCI board in a host computer. The laser sheet was aligned with the flow in the *xz*-direction and the camera was positioned outside the test section at the opposite side of the model to be able to capture the flow field above the wing with minimum shadows and reflections (Fig. 4). Measurements were performed at two spanwise wing locations, called the inner wing position (at 51% semi-span) and the outer wing position (63% semi-span).

4. Data analysis

Both aerodynamic and kinematic data were gathered from the images recorded by the PIV camera. The kinematics of the leading and trailing edges of the wing at the measured cross section were manually tracked with software described in Hedrick [29]. From these two points the pitching angle and the velocity of the midpoint were determined, which is used to determine the AoA, local Reynolds, Strouhal and Rossby number. The aerodynamic data were gathered from analyzing the PIV images using DaVis (7.4.0.122) with a multi-pass 2D cross-correlation (32 × 32, 16 × 16, 50% overlap) and a 3 × 3 smoothing average post-processing. From every period one frame was selected and analyzed resulting in nine frames per measurement with close to identical geometry and phase because of the repetitive motion of the model. These nine frames were averaged using Davis and analyzed with a custom made Matlab (7.11.0.584, R2010b) routine to determine the circulation. For every set-up 5 measurements were done that were used to calculate a mean value and a standard deviation (Fig. S4). The circulation was determined above the wing cross section using a semicircle determined by the line through the two points obtained from the kinematics and 70% of the local chord as radius to be able to capture all the relevant vortices (Fig. 5). Because of the turbulent character of the flow fields at high angles of attack (Fig. 5) we chose to use the swirling strength (λ_{el}) criterion for identifying vortices (Adrian et al. [30]). The swirling strength is determined by the imaginary part of the eigenvalues of the two-dimensional gradient tensor. The gradient tensor is determined by

$$D = \begin{pmatrix} \frac{\partial u_1}{\partial x_1} & \frac{\partial u_1}{\partial x_2} \\ \frac{\partial u_2}{\partial x_1} & \frac{\partial u_2}{\partial x_2} \end{pmatrix} \tag{15}$$

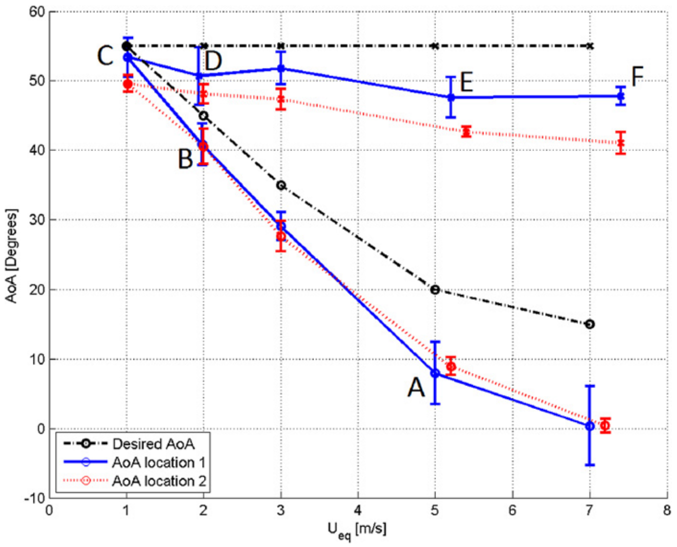

Fig. 6. Angle of attack versus equivalent free stream velocity U_{eq} (means ± standard deviation). The labels A–F refer to the panels in Fig. 7.

In this case negative vorticity was used for the circulation (Γ) if the swirling strength was larger than 5% of the maximum (Fig. 5) and the total area within these boundaries is used as a measure for the size of the vortices (S_ω). The circulation was used to calculate the circulation coefficient

$$C_\Gamma = \frac{\Gamma}{U_{\infty,eff} \cdot c_{loc}} \tag{16}$$

Based on the measured wing kinematics the local Reynolds number Re_{loc}, local Strouhal number St_{loc} and the local Rossby number Ro_{loc} (Lentink [31]) were calculated from Eqs. (17)–(19).

$$Re_{loc} = \frac{c_{loc} U_{\infty,eff}}{\upsilon} \tag{17}$$

where c_{loc} is the local chord length.

$$St_{loc} = \frac{0.5 U_{wing,z}}{U_\infty + U_{wing,x}} \tag{18}$$

with $U_{wing,z}$ being the local z component of the wing velocity and $U_{wing,x}$ the local x component of the wing velocity. The Rossby number is defined as

$$Ro_{loc} = \frac{U_{\infty,eff}}{\dot{\theta}_{loc} c_{loc}} = \frac{U_{\infty,eff} \cdot R_{loc}}{U_{wing} \cdot c_{loc}} \tag{19}$$

where $\dot{\theta}_{loc}$ is the local angular velocity, R_{loc} is the local semi-span. The Rossby number is a measure for the importance of the Coriolis acceleration due to rotation in the flapping motion.

5. Results

The resulting AoA$_{\max}$ for the two spanwise wing positions are shown in Fig. 6 together with the desired AoA$_{ref}$ based on the kinematics of *L. yerbabuenae*, throughout the measured flight speed range. It is clear that AoA$_{\max}$ is generally lower than the desired value, and this error increases both along the wingspan and with U_{eq}.

5.1. Description of the flow field

The vorticity values and instantaneous streamlines in the wing fixed reference frame for different flow fields are shown in Fig. 7. The flow field in a wing fixed reference frame gives primarily information about the aerodynamic state of the flow, and especially flow separation from the wing. The wing fixed reference frame flow fields were determined by subtracting the wing velocity in the *xz*-plane from the flow fields in the wind tunnel fixed reference frame.

Starting at AoA$_{\max} = 8°$ and $U_{eq} = 5$ m/s a quasi steady state is visible with very low values of vorticity (Fig. 7A). The slightly curved streamlines indicate some lift production, which corresponds with the low AoA$_{\max}$. At AoA$_{\max} = 41°$ and $U_{eq} = 2.0$ m/s (Fig. 7B) a clear separation bubble at the leading edge is visible with flow reattachment halfway along

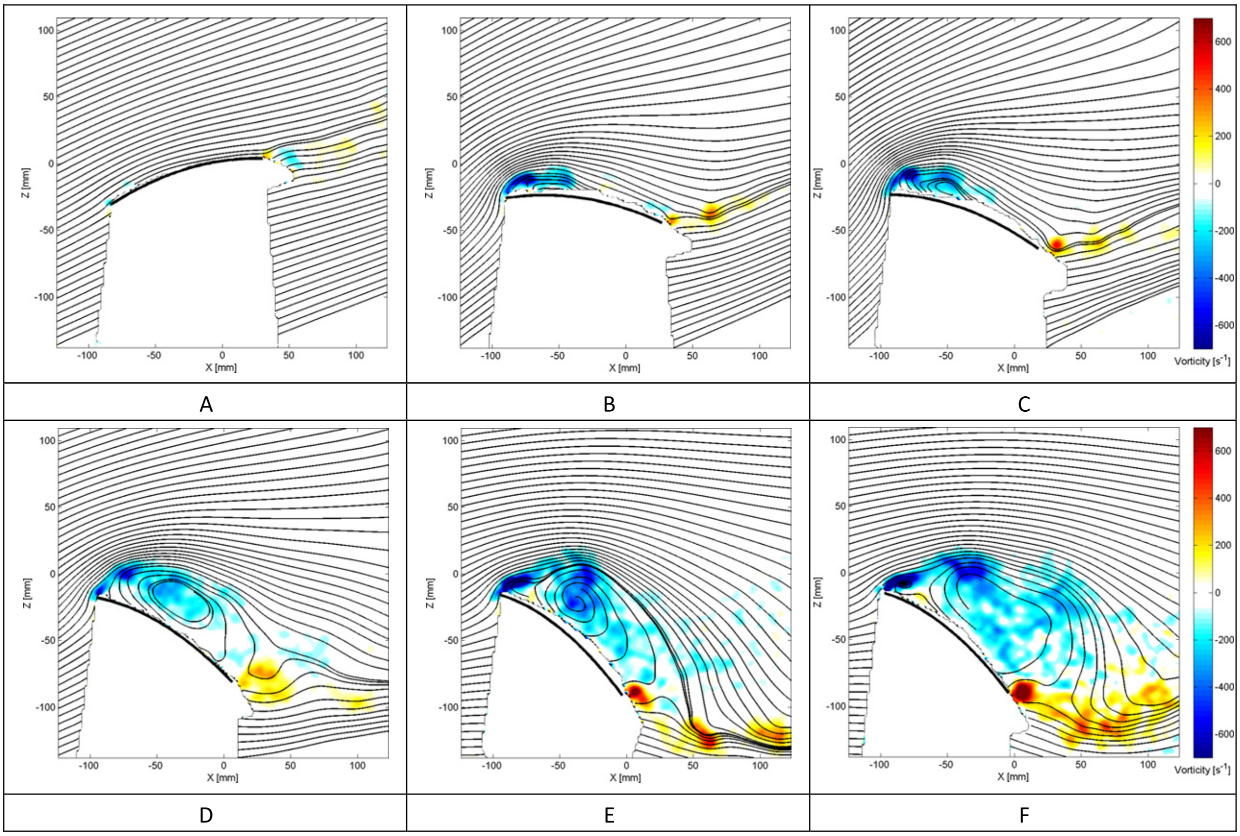

A B C

D E F

Fig. 7. Instantaneous streamlines and vorticity at the inner wing position. The values for the different panels are (A) AoA = 8°, $U_{eq} = 5.0$ m/s; (B) AoA = 41°, $U_{eq} = 2.0$ m/s; (C) AoA = 53°, $U_{eq} = 1.0$ m/s; (D) AoA = 51°, $U_{eq} = 2.0$ m/s; (E) AoA = 48°, $U_{eq} = 3.1$ m/s; (F) AoA = 48°, $U_{eq} = 7.4$ m/s.

the chord. The trailing edge vortices, of opposite sense to the LEF, that are shed indicate an increase in lift production by the wing throughout the downstroke. At $\text{AoA}_{\max} = 53°$ and $U_{eq} = 1.0$ m/s (Fig. 7C) the LEV has increased in size but reattachment still occurs upstream of the trailing edge. At $\text{AoA}_{\max} = 51°$ and $U_{eq} = 2.0$ m/s (Fig. 7D) the vorticity above the wing has suddenly greatly increased, reattachment does not occur anymore, and the vortices that are generated at the leading edge of the wing are periodically shed into the wake. These characteristics are indicative of LEV bursting (Lentink and Dickinson [32]). The burst vortex wake increases in size consistently with increasing flight speed (Fig. 7E: $\text{AoA}_{\max} = 48°$, $U_\infty = 2.6$ m/s, and Fig. 7F: $\text{AoA}_{\max} = 48°$, $U_\infty = 3.7$ m/s). Note that vortex bursting is a result of the change in U_{eq}, since the $\text{AoA}_{\max}$ stays nearly constant in the cases shown in Fig. 7C–F.

5.2. Vortex dynamics

The circulation coefficients (c_Γ) determined from the vortices positioned above the wing are plotted against Re_{loc}, AoA_{loc} and St_{loc} and Ro_{loc} in Fig. 8A–D, respectively, as well as for the vorticity area (S_ω) in Fig. 9A–D, respectively.

The increase in c_Γ occurs at an almost constant Re_{loc} (variable $\text{AoA}_{\max}$ measurements in Fig. 8A), while c_Γ remains constant with increasing Re_{loc} (constant $\text{AoA}_{\max}$ measurements in Fig. 8A). This shows that c_Γ is largely independent from Re_{loc}. The same is almost valid for S_ω although S_ω remains increasing for the constant $\text{AoA}_{\max}$ measurements with increasing Re_{loc} (Fig. 9A).

Fig. 8B shows that c_Γ is associated with $\text{AoA}_{\max}$. For the variable $\text{AoA}_{\max}$ measurements, a weak LEV starts to occur at $\text{AoA}_{\max} = 30°$, and its strength (c_Γ) and size (S_ω) increases almost linearly with $\text{AoA}_{\max}$ up to $\text{AoA}_{\max} > 50°$ (Fig. 8B). For the constant $\text{AoA}_{\max}$ measurements, c_Γ initially increases with flight speed (Fig. 8B, label C–D), but then remains rather constant with further increased speed (Fig. 8B, label D–F). The vortex size (S_ω) increases by a factor 3–4 for the constant $\text{AoA}_{\max}$ measurements.

The largest increase in c_Γ occurs also at a constant St_{loc} (~ 0.3, variable $\text{AoA}_{\max}$ measurements in Fig. 8C), while c_Γ remains almost constant when St_{loc} decreases from 0.2 to 0.05 (constant $\text{AoA}_{\max}$ measurements in Fig. 8C). Thus, c_Γ is also largely independent from St_{loc}. In contrast, S_ω seems to be St_{loc} dependent because for data points where S_ω is increasing the most St_{loc} is decreasing almost linearly (Fig. 9C).

The shape of the c_Γ–Ro_{loc} and S_ω–Ro_{loc} curves (Fig. 8D and 9D) are comparable with the c_Γ–Re_{loc} and S_ω–Re_{loc} curves.

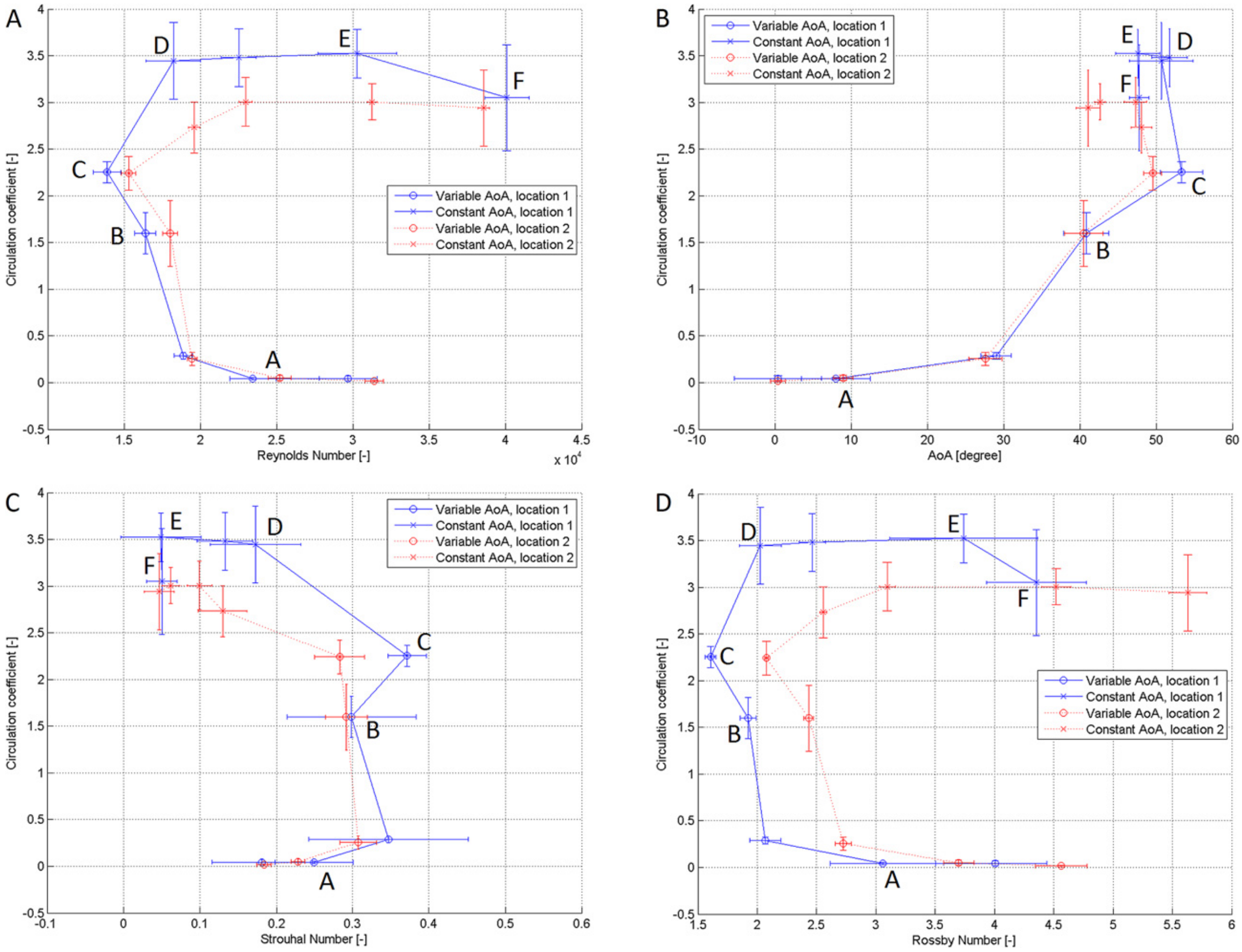

Fig. 8. Circulation coefficient (means ± standard deviation) of vortex structure above the wing with respect to Re_{loc} (A), $\text{AoA}_{\max}$ (B), St_{loc} (C) and Ro_{loc} (D). The labels A–F refer to the panels in Fig. 7.

6. Discussion

6.1. RoBat model

Although the RoBat model does not capture the full complexity of either real bat wing kinematics or wing morphology, we show that the simplified kinematics of the RoBat, based on sinusoidal flapping, pitching and leading edge flap deflection, can be used as model to study fluid dynamics mechanisms relevant for bats.

Across the complete studied flight speed range, the resulting $\text{AoA}_{\max}$ was lower in the model than that of real bats. This discrepancy was largest at high U_{eq} and at the spanwise, more distal, wing position. Therefore, we can assume that the reduction in $\text{AoA}_{\max}$ for the RoBat is due to spanwise pitch down wing twist as a result of lift production. These aeroelastic effects were not captured by our kinematics optimization scheme, resulting in the overestimation of the $\text{AoA}_{\max}$ in the RoBat.

6.2. Vortex dynamics

The test sequence with variable $\text{AoA}_{\max}$ represents a steady flight of bats and shows no LEVs at high speeds and a strong stable attached LEV at low speeds. This transition is primarily due to an increase in $\text{AoA}_{\max}$ with decreasing flight speed, which parallel the conditions when real bats exhibit a LEV (Muijres et al. [7]).

The constant $\text{AoA}_{\max}$ sequence showed that, throughout the complete flight speed range, it is possible to generate a LEV by operating at a high enough $\text{AoA}_{\max}$, and that the strength of the LEV structure (c_Γ) stays nearly constant at constant $\text{AoA}_{\max}$ throughout the complete measured flight speed range. The structure and size of the LEV vary significantly with flight speed, which can be explained by a change in St_{loc}, and independent from Re_{loc}.

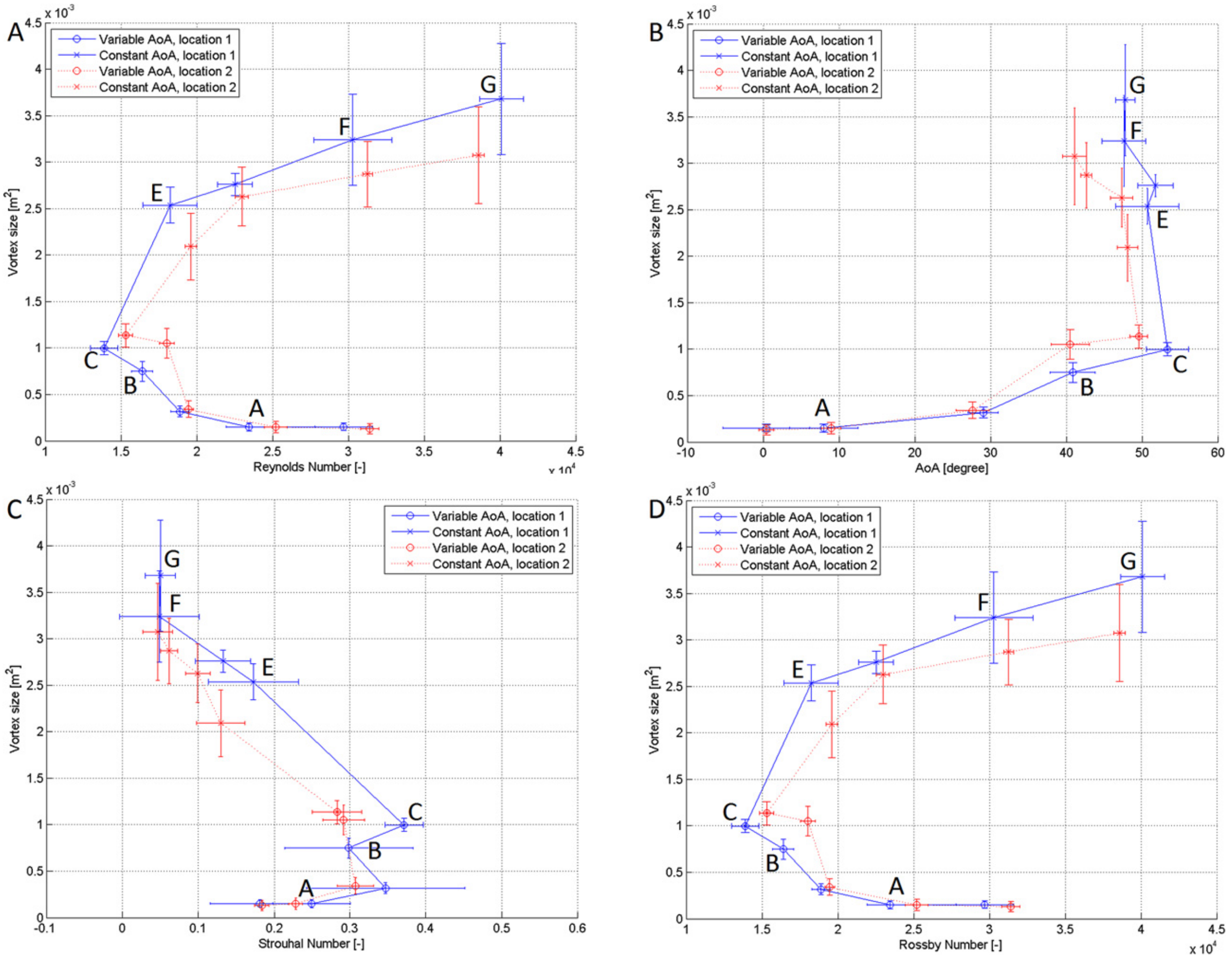

Fig. 9. Cumulative area (means ± standard deviation) of the vortex structures above the wing with respect to Re_{loc} (A), AoA$_{\max}$ (B), St_{loc} (C) and Ro_{loc} (D). The labels A–F refer to the panels in Fig. 7.

6.3. Relevance for bats

Based on lift coefficient estimates for flying *L. yerbabuenae* (Muijres et al. [11]) an enhanced lift mechanism, such as a LEV, can be expected at low flight speeds ($C_{L\max} > 1.6$ for $U_{eq} < 4$ m/s), but not at high flight speeds ($C_{L\max} < 1.6$ for $U_{eq} > 4$ m/s) (Laitone [14]). This corresponds well with the results obtained in the present study. Also, the LEV structure found at $U_{eq} = 1$ m/s was similar to that found in a smaller species of bat *G. soricina* (Muijres et al. [7]).

LEVs can enhance C_L, but this comes with a penalty of increased drag (Lentink and Dickinson [32]). Therefore, we can assume that bats use LEVs at low flight speeds to generate enough lift for weight support. At cruising flight speeds the LEV is not required, and bats use the energetically more efficient attached flow at low AoA.

Still, bats are expected to be able to generate LEVs at high flight speeds by increasing AoA as shown by the present study, but it comes at a price, though, since the LEV tends to burst at high speeds, resulting in completely separated flow and high drag. Thus, LEVs could potentially be used by bats throughout the complete natural flight speed range in high load maneuvers such as sharp turns.

The increased sensitivity of the trailing edge part of the wing membrane for detecting reversed airflow as described recently (Chadha et al. [15], Sterbing-D'Angelo et al. [16]) could be used to sense LEV bursting. This information could be used by the bat to actively adjust wing kinematics to control the flow above the wing, which could possibly prevent LEV bursting and improve flight performance.

6.4. Relevance for MAVs

For the design of MAVs the fact that a single parameter, such as the stroke plane angle has such profound influence on the flow field and possibly the resulting flight forces is very interesting, especially since the stroke plane angle in an MAV can directly be controlled by changing its body angle.

The almost constant circulation coefficient around 50 degrees AoA_{max} indicates that there is little influence of LEV bursting on the lift production, which makes it possible to use high AoA both at low and high speeds. However, lift enhancement by using LEVs will be less efficient at high speeds due to the expected increased drag from a bursted LEV.

6.5. Concluding remarks

Despite the complexity of the wing kinematics in bats we have been able to show that both bats and MAVs can extend their flight performance envelope by controlling only their body angle/stroke plane. This is accomplished by controlling the LEV lift production through changes of the AoA caused by the altered stroke plane. Further studies, incorporating higher complexity of the wing motion, will determine if this can be accomplished with higher efficiency by for example active control of the leading edge flap and camber of the wing.

We have shown that a mechanical bat model can be used to generate bat-like aerodynamic features, which in turn can be used to investigate the level of adaptation of morphology and kinematics as seen in real bats. To implement a bat-like MAV, possessing flight performance and control comparable to real bats, may require not only materials and kinematics properties similar to those in real bats, but also the implementation of wing-surface airflow sensors and the appropriate feedback to the actuating mechanism.

Acknowledgements

This study was financially supported by the Swedish Research Council in the form of a project grant (AH) and a Linnaeaus grant to support the Centre for Animal Movement Research (CAnMove), the Carl Tryggers Foundation and Lund University (CAnMove).

Supplementary material

The online version of this article contains additional supplementary material.
Please visit doi:10.1016/j.crme.2011.11.013.

References

[1] D. Lentink, A.A. Biewener, Nature-inspired flight—beyond the leap, Bioinspiration & Biomimetics (2010) 040201, 9 pp.
[2] A. Hedenström, L.C. Johansson, M. Wolf, R. von Busse, Y. Winter, G.R. Spedding, Bat flight generates complex aerodynamic tracks, Science 316 (2007) 894–897.
[3] A. Hedenström, F. Muijres, R. von Busse, L.C. Johansson, Y. Winter, G.R. Spedding, High-speed stereo DPIV measurements of bat wakes flying freely in a wind tunnel, Experiments in Fluids 46 (2009) 923–932.
[4] R. von Busse, The Trinity of Energy Conversion: Kinematics, Aerodynamics and Energetics of Lesser Long-Nosed Bat (*Leptonycteris Yerbabuenae*), Humboldt University, Berlin, 2010.
[5] X. Tian, J. Iriarte-Diaz, K. Middleton, R. Galvao, E. Israeli, A. Roemer, A. Sullivan, A. Song, S. Swartz, K. Breuer, Direct measurements of the kinematics and dynamics of bat flight, Bioinspiration & Biomimetics 1 (2006) S10–18.
[6] L.C. Johansson, M. Wolf, R. von Busse, Y. Winter, G.R. Spedding, A. Hedenström, The near and far wake of Pallas' long tongued bat (Glossophaga soricina), Journal of Experimental Biology 211 (2008) 2909–2918.
[7] F.T. Muijres, L.C. Johansson, R. Barfield, M. Wolf, G.R. Spedding, A. Hedenström, Leading edge vortex improves lift in slow-flying bats, Science 319 (2008) 1250–1253.
[8] T.Y. Hubel, N.I. Hristov, S.M. Swartz, K.S. Breuer, Time-resolved wake structure and kinematics of bat flight, Experiments in Fluids 46 (2009) 933–943.
[9] T.Y. Hubel, D.K. Riskin, S.M. Swartz, K.S. Breuer, Wake structure and wing kinematics: The flight of the lesser dog-faced fruit bat, Cynopterus brachyotis, Journal of Experimental Biology 213 (2010) 3427–3440.
[10] M. Wolf, L.C. Johansson, R. von Busse, Y. Winter, A. Hedenström, Kinematics of flight and the relationship to the vortex wake of Pallas' long-tongued bat (Glossophaga soricina), Journal of Experimental Biology 213 (2010) 2142–2153.
[11] F.T. Muijres, L.C. Johansson, Y. Winter, A. Hedenström, Comparative aerodynamic performance of flapping flight in two bat species using time-resolved wake visualization, Journal of the Royal Society Interface 8 (2011) 1418–1428.
[12] U.M. Lindhe-Norberg, Y. Winter, Wing beat kinematics of a nectar feeding bat, Glossophaga soricina, flying at different flight speeds and Strouhal numbers, Journal of Experimental Biology 209 (2006) 3887–3897.
[13] F.T. Muijres, G.R. Spedding, Y. Winter, A. Hedenström, Actuator disk model and span efficiency of flapping flight in bats based on time-resolved PIV measurements, Experiments in Fluids 51 (2011) 511–525.
[14] E.V. Laitone, Wind tunnel tests of wings at Reynolds numbers below 7000, Experiments in Fluids 23 (1997) 405–409.
[15] M. Chadha, C.F. Moss, S.J. Sterbing-D'Angelo, Organization of the primary somatosensory cortex and wing representation in the Big Brown Bat, Eptesicus fuscus, Journal of Comparative Physiology 197 (2011) 89–96.
[16] S. Sterbing-D'Angelo, M. Chada, C. Chiu, B. Falk, W. Xian, J. Barcelo, J.M. Zook, C.F. Moss, Bat wing sensors support flight control, Proceedings of the National Academy of Sciences 108 (2011) 11291–11296.
[17] H. Soueid, L. Guglielmini, C. Airiau, A. Bottaro, Optimization of the motion of a flapping airfoil using sensitivity functions, Computers & Fluids 38 (2009) 861–874.
[18] Y. Sudhakar, S. Vengadesan, Flight force production by flapping insect wings in inclined stroke plane kinematics, Computers & Fluids 39 (2010) 683–695.
[19] M.H. Dickinson, F.-O. Lehmann, S.P. Sane, Wing rotation and the aerodynamic basis of insect flight, Science 284 (1999) 1954–1960.
[20] T.Y. Hubel, C. Tropea, Experimental investigation of a flapping wing model, Journal of Experimental Biology 46 (2008) 945–961.
[21] T.Y. Hubel, C. Tropea, The importance of leading edge vortices under simplified flapping flight conditions at the size scale of birds, Journal of Experimental Biology 213 (2010) 1930–1939.
[22] G. Bunget, BATMAV – A bio-inspired micro-aerial vehicle for flapping flight, 2010.

[23] M.A. Horner, T.H. Fleming, C.T. Sahley, Foraging behaviour and energetics of a nectar-feeding bat, Leptonycteris curasoae (Chiroptera: Phyllostomidae), Journal of Zoology 244 (1998) 575–586.

[24] C.T. Sahley, M.A. Horner, T.H. Fleming, Flight speeds and mechanical power outputs of the nectar-feeding bat, Leptonycteris curasoae (Phyllostomidae: Glossophaginae), Journal of Mammalogy 74 (1993) 594–600.

[25] S.M. Swartz, J. Iriarte-Diaz, D.K. Riskin, Wing structure and the aerodynamic basis of flight in bats, American Institute of Aeronautics and Astronautics Journal (2007) 2007–2042.

[26] S.M. Swartz, M.S. Groves, H.D. Kim, W.R. Walsh, Mechanical properties of bat wing membrane skin, Journal of Zoology 239 (1996) 357–378.

[27] S.M. Swartz, K.M. Middleton, Biomechanics of the bat limb skeleton: Scaling material properties and mechanics, Cells Tissues Organs 187 (2008) 59–84.

[28] C.J. Pennycuick, T. Alerstam, A. Hedenström, A new low-turbulence wind tunnel for bird flight experiments at Lund University, Sweden, Journal of Experimental Biology 200 (1997) 1441–1449.

[29] T.L. Hedrick, Software techniques for two- and three-dimensional kinematic measurements of biological and biomimetic systems, Bioinspiration & Biomimetics 3 (2008) 034001, 6 pp.

[30] R.J. Adrian, K.T. Christensen, Z.C. Lui, Analysis and interpretation of instantaneous turbulent velocity fields, Experiments in Fluids 29 (2000) 275–290.

[31] D. Lentink, Exploring the biofluiddynamics of swimming and flight, PhD Thesis, Wageningen University, 2008.

[32] D. Lentink, M.H. Dickinson, Rotational accelerations stabilize leading edge vortices on revolving fly wings, Journal of Experimental Biology 212 (2009) 2705–2719.

[33] E.R. Dumont, Bone density and the lightweight skeletons of birds, Proceedings of the Royal Society B 277 (2010) 2193–2198.